Technische Universität München
Fakultät für Maschinenwesen

Tungsten Properties Correlated with the Orientation of its Crystals

Karsten Schlüter

Vollständiger Abdruck der von der Fakultät für Maschinenwesen der Technischen Universität München zur Erlangung des akademischen Grades eines

Doktor-Ingenieurs (Dr.-Ing.)

genehmigten Dissertation.

Vorsitzender: Prof. Dr.-Ing. habil. Christian Große

Prüfer der Dissertation: 1. Prof. Dr. Rudolf Neu
2. Prof. Dr. Carmen García-Rosales Vázquez

Die Dissertation wurde am 21.01.2021 bei der Technischen Universität München eingereicht und durch die Fakultät für Maschinenwesen am 14.06.2021 angenommen.

Abstract

Erosion, oxidation and sputtering of materials are of high interest in industry and research. In general it is known that the crystal lattice has an impact on many material properties, but the investigations are often performed on single crystals and only for a few crystal orientations. Knowledge about the impact of the crystal lattice in 'every' crystal orientation can be employed to an advantage and, furthermore, simulations could be used as a benchmark to predict the material behavior in applications like fusion. Therefore, a systematic study is highly desirable for characterizing properties such as sputtering for many different crystal orientations. This can be done with single crystals or with polycrystalline samples.

Investigating single crystals is time and effort consuming, expensive, and the extrapolation of the behavior to a textured sample can hardly be achieved. Conversely, the main advantage for using flat polycrystalline samples is that many different crystal orientations are present on one sample and all orientations undergo the same conditions in the experiment, i.e., variations between different experimental runs are excluded. For analyzing properties on polycrystalline samples, a measuring and evaluation strategy is needed to study the influence of the crystal surface orientation on the material properties of tungsten. Different analytical devices characterize polycrystalline samples with millions of data points, which should be combined. Therefore, a python tool was programmed to correlate these data sets and evaluate them. Similar experimental strategies were applied to investigate several tungsten properties. This enables to study surface effects, like oxidation, sputtering and etching.

The used polycrystalline tungsten samples had grains of around $10\,\mu\text{m}$, where each grain corresponds to one crystal orientation. With electron backscatter diffraction (EBSD), it was possible to determine the orientation of thousands of grains, which were the key data to describe crystal-dependent properties. The second main analytical device was the confocal laser scanning microscope (CLSM), which was used to measure height differences with a resolution of around $50\,\text{nm}$. The merged data sets of these two devices enabled studies on oxidation, sputtering and etching on single crystal grain surfaces. For even more detailed investigations, a python tool was continuously developed and extended to correlate additional data sets, like secondary electron emission, contrast data of the CLSM or energy dispersive X-ray spectroscopy (EDX) data maps.

In general, the measurements for different properties show that the crystal dependency is non-linear. This means without a physical understanding, it is not possible to interpolate the crystal dependency with a few crystal-dependent measurements. The crystals dependency is complex and measurements in all crystal orientations are essential to generate a detailed data set to investigate correlations and develop models.

One correlation was observed for etching. In this work, the crystal-dependent etching of tungsten was performed with Muramkami solution. The etching rates differed by several orders of magnitudes and showed a strong correlation with the Schmid factor. For a deeper understanding, future investigations are necessary to verify this correlation.

Compared to etching, oxidation is a process with different phases and to separate them is tricky. In the temperature range from $450 - 600\,°C$, tungsten grains with $\langle 100 \rangle$ surface orientation had the highest oxidation rate. In comparison to the tungsten grains with $\langle 111 \rangle$ orientation, which showed the lowest oxidation rate, the oxidation rate of tungsten grains with $\langle 100 \rangle$ orientation was twice as high. On one hand, it was shown that surface effects dominate the oxidation of each crystal orientation at the starting point of the oxidation. On the other hand, the tungsten oxide layer on different grains was different and could influence the diffusion of oxygen to tungsten in the second phase of the oxidation. This would explain the change of the oxidation rate for the $\langle 111 \rangle$ crystal orientation. For nm thick oxide layers, the $<111>$ orientation exhibited the highest oxidation rate compared to the other crystal orientations, while it had the lowest oxidation rate for a µm thick oxide layer.

Sputtering is a process which is far more understood than oxidation or etching, but still detailed research is required. Crystal-dependent sputter yields were determined by measuring the erosion depth of each grain for a $2\,keV$, $8\,keV$ and $30\,keV$ gallium (Ga) ion beam and a $2\,keV$ deuterium (D) beam on tungsten targets. Angle dependent sputter yield studies were performed with a $30\,keV$ Ga beam. In general, the low index surfaces had the lowest sputter yields, and the high index surfaces had the highest sputter yields. The differences of the sputter yields were around one order of magnitudes for a $30\,keV$ Ga ion beam and a $2\,keV$ D beam. Sophisticated sputter simulations were in very good agreement with the experimental data. In addition, the secondary electron emission and the Ga implantation were investigated in relation to the crystal orientation. The secondary electron emissions behaved similarly to the crystal orientation as the sputter yields did. The Ga implantation had a different behavior in view of the crystal orientation. The Ga concentration was high for the low index surfaces, around $20\,at\%$, and for the low index surfaces, the Ga concentration was below the detection limit of the used EDX-detector. With the collected data the impact angle of the ions was measured, and the data sets were optimized.

The developed measuring and evaluation strategy to investigate material properties dependent on the crystal surface orientation can be applied now to many materials and to other research or industrial fields, for example battery research. In general, the crystal surface orientation has a big impact on properties and therefore, could have a significant influence on applications.

Contents

1 Introduction

For manufacturing components, the choice of materials is fundamental. Already the time epochs, e.g. Stone Age, Bronze Age, are named after the materials, which were used to manufacture tools. The continuous development of the materials and therefore new tools are one key aspect of the development of the human society. An example is the plough, which changed the whole human society from the hunter-gatherer to the beginning of a settled life[1].

During the time a lot of materials were discovered, developed and had a significant influence in different epochs. As an overview, the relative importance of the material versus the time is visualized in figure 1.1 from 10.000 BC until now[2].
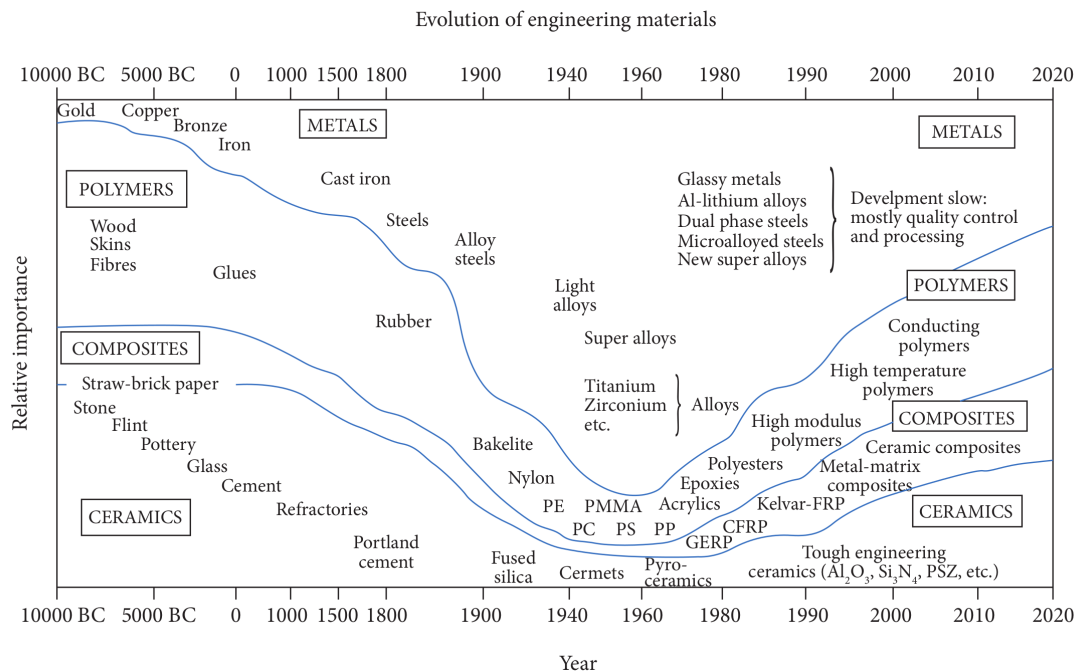
Evolution of engineering materials

Figure 1.1: "The importance of the four classes of materials (ceramics, composites, polymers, and metals) in engineering as a function of time. The timescale is nonlinear."[3]

Nowadays, there are more than 50.000 materials available[4] to engineer, design or manufacture components. Already the amount of different materials is a challenge to choose the suitable materials for the desired applications. After the selection of the suitable material, the engineer has boundary conditions to construct, e.g. a turbine.

Density, stress, strain, and temperature resistance are just a few examples of these boundaries. The optimization of the material properties is important to widen the limits and thereby, enhancing the properties of the produced component. For
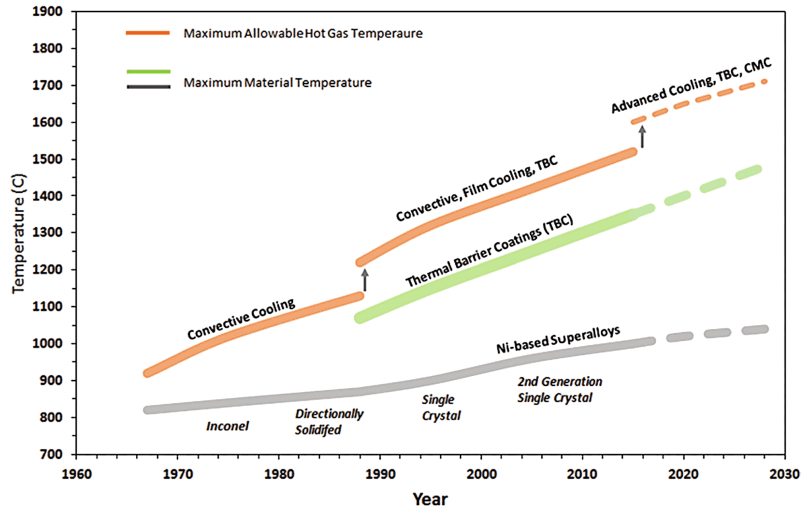
1

Figure 1.2: "Evolution of gas turbine hot gas temperatures, materials, and cooling technology." [5]

example, a gas turbine will have a higher efficiency if the operating temperature as well as the mechanical properties of the materials are enhanced. Figure 1.2 shows the operating temperature increase of a turbine over the years [5].

On the one hand, the temperature resistance of the materials increases by using single crystal Ni-based alloys, on the other hand, an engineering design increases the temperature resistance by using a thermal barrier coating. Such developments result from detailed studies of material properties and are important for high-tech research and technology development projects.

The development of a future fusion power plant is such a technology project, where the components, respectively the materials, are at their limits or even beyond their limits. Therefore, detailed investigations are necessary that the material can tolerate the impact of a fusion plasma at the first wall.

The center of a fusion plasma is over 100 million degree hot and magnetically confined inside a vacuum vessel. Nevertheless, inside a fusion reactor components must tolerate power loads of around $10\,\mathrm{MW/m^2}$ for years. Tungsten is one of the most promising materials to face this challenge. It is the metal with the highest melting point, has a low sputter rate, low hydrogen retention, and other promising properties, which are investigated and optimized [6,7]. It is already known from literature that the crystal lattice has an impact on properties such as sputtering, however, often only the low index surfaces were investigated [8,9,10,11,12,13]. Therefore, detailed analyses are required and it is just consistent to build up methods to investigate tungsten properties in relation to its crystal surface orientation.

Detailed studies are nowadays far easier to perform due to the development of data acquisition systems. One of the first data acquisition systems was the IBM 7700 in 1963. Mid-1980s, the company National Instruments Corporation established

a data acquisition solution with the software LabVIEW and an interface, first for Macintosh computers, later for Windows computers. Meanwhile, computational data acquisition has captured all scientific and engineering areas. Furthermore, the computational speed increased exponentially over the years[14,15] as well as the stored data amount, which contributes to the computational progress. In addition, analytical systems were greatly improved.

The EBSD technique is an useful and fast analytical tool in detecting crystal orientations down to sub-µm length scale. For measuring the crystal orientation, electrons are scattered at the crystal lattice and a phosphor screen visualizes the diffraction pattern. The phosphor screen is digitized by taking an image. "Photo sensor chips", so called complementary metal oxide semiconductor (CMOS)-chips, which nowadays are used in every cellphone or camera, had a significant development over the last decade. The CMOS-chips are applied in the newest generation of EBSD-detectors to speed up the measurements by several orders of magnitudes[16], allowing the detection of millions of crystal orientations within a reasonable time.

Also, other analytical systems got fast. The CLSM measures millions of height data and the EDX system can characterize the elemental composition of a sample area of around $1\,\mathrm{mm}^2$. By correlating, e.g. the height measurement to the crystal orientations, properties such as sputtering can be investigated very detailed. Therefore, systematic studies are now possible for characterizing properties in every crystal orientation. For these studies, polycrystalline samples are used, which have many single crystal grains and easily thousands of different crystal orientations on one sample.

The new technical opportunities were utilized in this work and properties were described in 'every' crystal orientation. There are still several open questions on tungsten oxidation or as E. Lassner stated: "The crystal chemistry of tungsten oxides can be regarded as one of the most complex and richest fields in the structural chemistry of the elements."[17] A fast evaluation tool can analyze the oxidation behavior of tungsten for all crystal orientations, which can be interesting for applications like solar cells, where oxidation should be avoided.

Sputtering is another property where the crystal orientation has an impact. Sputtering is already well described and its surface grain orientation dependence is often mentioned. Many experiments were performed on single crystals, but often the high index surfaces are missing. Describing sputtering for thousands of crystal orientations can benchmark simulations to experimental data. Also a detailed crystal-dependent knowledge about sputtering can predict the sputter behavior of a textured material, e.g., in a fusion reactor. In addition, predicting the roughness of polycrystalline samples due to ion polishing will be possible. There are many fields where a detailed knowledge can help to predict and describe the behavior of the material or enhance applications to the crystal orientation.

In general, metals are often polycrystalline and the effect of the crystal orientation

is not negligible for applications. The turbine blades are such examples which use already now single crystals, see figure 1.2. In addition, there are different kinds of known textures to optimize properties for applications, e.g. the Goss texture which optimizes the magnetic properties of iron. Describing properties in every crystal orientation will give input for such optimizations and is highly desirable.

2 Background

This chapter introduces a basic knowledge on tungsten (W), its crystal structure as well as on projections for illustrating crystallographic data. Meanwhile, the crystal-orientation dependent properties of W, including oxidation, sputtering and etching, will be briefly described as well. An in-depth description of the concepts and methods described here can be found in Refs.[17,18,19,20,21].

2.1 Tungsten

W is a transition metal, has the highest melting point of all metals, which is $3694\,\mathrm{K}$ and a density of $19.3\,\mathrm{g/cm^3}$[17]. The W amorphous phase as well as β and γ crystalline phases are metastable. Only the crystalline α-W phase is stable.

W has a body-centered cubic (bcc) lattice, as shown in figure 2.1 (b). In comparison to the simple cubic lattice, there is an additional atom in the center of the unit cell. A unit cell is the smallest group of atoms in the material with a repeating pattern, which means a group of eight $\frac{1}{8}$ atoms for a simple cubic and two for a bcc. The side lengths (a) are equal of these unit cells and the angles between the side lengths are perpendicular.[18].
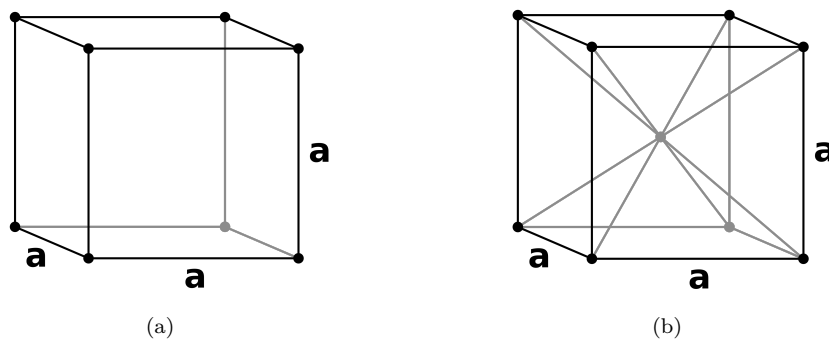

(a)   (b)

Figure 2.1: Unit cell of simple cubic (a) and bcc (b) crystals.

Typically, the crystal orientation is described by Miller indices {hkl} for planes and ⟨uvw⟩ for directions. The different brackets have a specific meaning. The brackets {} and ⟨⟩ includes all symmetric equivalent crystal orientations. This means, the symmetric equivalent directions are [100], [010], [001], [$\bar{1}$00], [0$\bar{1}$0], [00$\bar{1}$] for the ⟨100⟩ crystal direction and the symmetric equivalent planes are (100), (010), (001), ($\bar{1}$00), (0$\bar{1}$0), (00$\bar{1}$) for the {100} crystal orientation. The interplanar spacing (d) is the distance between two crystal planes and for a bcc, d can be expressed as

$$\frac{1}{d^2} = \frac{h^2 + k^2 + l^2}{a^2},\tag{2.1}$$

where a is the lattice constant. For W the lattice constant (a) is 3.16 Å at room temperature[18]. Based on the arrangement of unit cells, shown in figure 2.2, materials can be single crystalline, polycrystalline and amorphous.
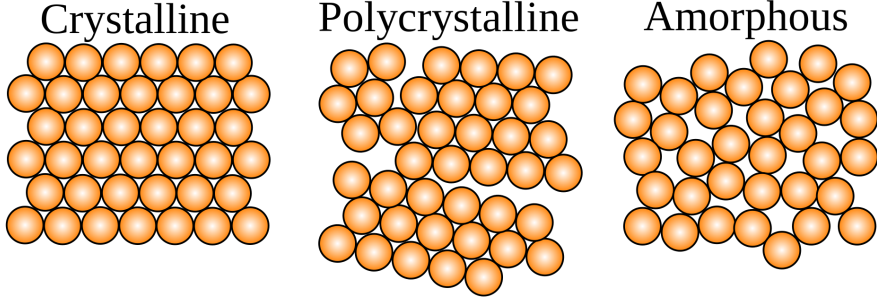

Figure 2.2: Illustration of the arrangement of atoms. Three different examples are shown: (a) single-crystals, (b) polycrystals, (c) amorphous solids[22].

In this work, W with a polycrystalline structure was used for studying the crystal orientation dependent properties, as it contains many "small scale" single crystals with various orientations. A perfect arrangement of atoms can be disturbed by so-called defects, such as point-, line-, planar- or volume-defects. To minimize the amount of defects, the as-received polycrystalline W samples were recrystallized at elevated temperatures.

2.2   Representation of crystallographic data

Crystal orientation data are often defined in three Euler angles, φ_1, ϕ, φ_2, which describe the rotation of crystal axis[20,21]. The rotations follow a specific sequence:

- First, φ_1 represents a rotation around the Z axis and transforms X into X′ and Y into Y′

- Second, ϕ represents a rotation around the X′ axis and transforms Y′ into Y″ and Z into Z′

- Third, φ_2 represents a rotation around the Z′ axis and transforms Y″ into Y‴ and X′ into X″

The rotations are illustrated in figure 2.3. The three rotations can be separately expressed in three matrices or all together as shown in the rotation matrix R.
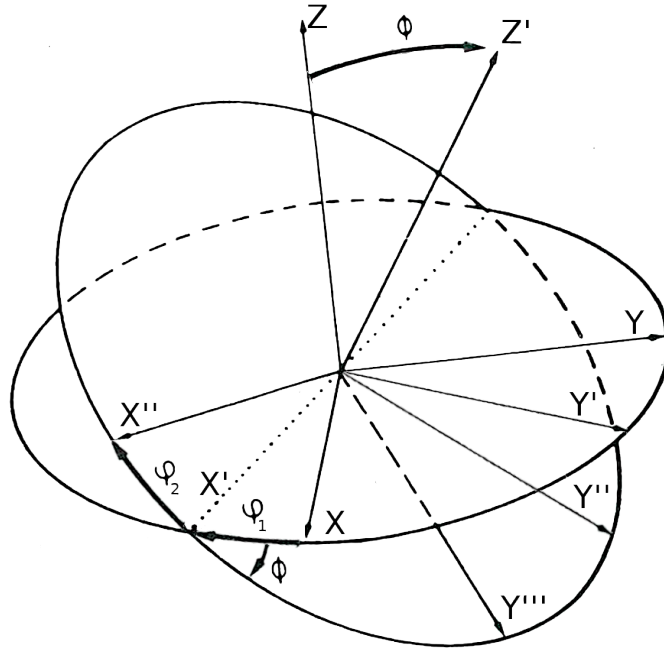
Figure 2.3: Schematic illustration showing the geometrical definition of Euler angles.

$$R = \begin{Bmatrix} r_{11} & r_{12} & r_{13} \\ r_{21} & r_{22} & r_{23} \\ r_{31} & r_{32} & r_{33} \end{Bmatrix} \tag{2.2}$$

The elements of the rotation matrix R are:

$$
\begin{aligned}
r_{11} &= \cos(\varphi_1)\cos(\varphi_2) - \sin(\varphi_1)\sin(\varphi_2)\cos(\phi) \\
r_{12} &= \sin(\varphi_1)\cos(\varphi_2) + \cos(\varphi_1)\sin(\varphi_2)\cos(\phi) \\
r_{13} &= \sin(\varphi_2)\sin(\phi) \\
r_{21} &= -\cos(\varphi_1)\sin(\varphi_2) - \sin(\varphi_1)\cos(\varphi_2)\cos(\phi) \\
r_{22} &= \sin(\varphi_1)\sin(\varphi_2) + \cos(\varphi_1)\cos(\varphi_2)\cos(\phi) \\
r_{23} &= \cos(\varphi_2)\sin(\phi) \\
r_{31} &= \cos(\varphi_2)\cos(\phi) \\
r_{32} &= -\cos(\varphi_1)\sin(\phi) \\
r_{33} &= \cos(\phi)
\end{aligned}
\tag{2.3}
$$

The rotation matrix expresses the Miller indices as {hkl} for planes and ⟨uvw⟩ for directions. The directions are described in the first column of the rotation matrix

7

and the planes are described in the third column in the rotation matrix, which means:

$$r_{13} = h \qquad r_{23} = k \qquad r_{33} = l$$
$$r_{11} = u \qquad r_{21} = v \qquad r_{31} = w$$

(2.4)

The Miller indices reduce the dimension and represent the data in one direction, often the normal direction of the surface. For a full description of a crystal orientation, the crystal plane and the crystal direction must be presented in two different directions in planes, e.g. in normal direction to the surface and in transversal direction.

The Miller indices can be evaluated to any direction and not only to the surface normal. For a sputter experiment, the crystal lattices of the grains can be evaluated in direction of the impacting ions. For this purpose, all crystal orientation data is calculated to the new evaluation direction, e.g. the impacting ions. The following rotation matrix multiplication was used and the Miller indices were calculated from R_{12}:

$$R_{12} = R_1^{-1} \cdot R_2$$

(2.5)

where R is defined in 2.2 and 2.3. The Euler angles of R_1 are defined from the crystal orientation measurement and the Euler angles of R_2 define the rotation. If the Euler angles of R_2 are $\varphi_1 = 0$ and $\varphi_2 = 0$, ϕ will describe a rotation around the X axis (figure 2.3). If $\varphi_1 = 90$ and $\varphi_2 = 0$, ϕ will describe a rotation around the Y axis (figure 2.3). The rotation matrix multiplication is relevant specially for sputter experiments.

In this work, the sputter yields were evaluated to the direction of the impacting ions. Since for a cubic crystal system the planes ("{ }") and the directions ("⟨ ⟩") perpendicular to the planes are equal, the bracket "⟨ ⟩" is used to describe the crystal-dependent properties.

The Miller indices are often visualized in a stereographic projection, which is a visualization of a sphere surface in a 2D plane. A Wulff[23] net, shown in figure 2.4, is such a projection which is angle-preserving. Another projection is the Lambert azimuthal equal-area projection[24], which is especially used for statistical purposes. Crystallographic data often uses a Wulff net, as it enables to evaluate angle relationships between different crystal orientations, e.g. the misalignment angle.

In figure 2.4, the low index directions in a bcc crystal structure are marked by the black dots in the pole figure. Since a stereographic projection plots only the half sphere, orientations on the other half of the sphere (e.g. [00-1]) are not visible.
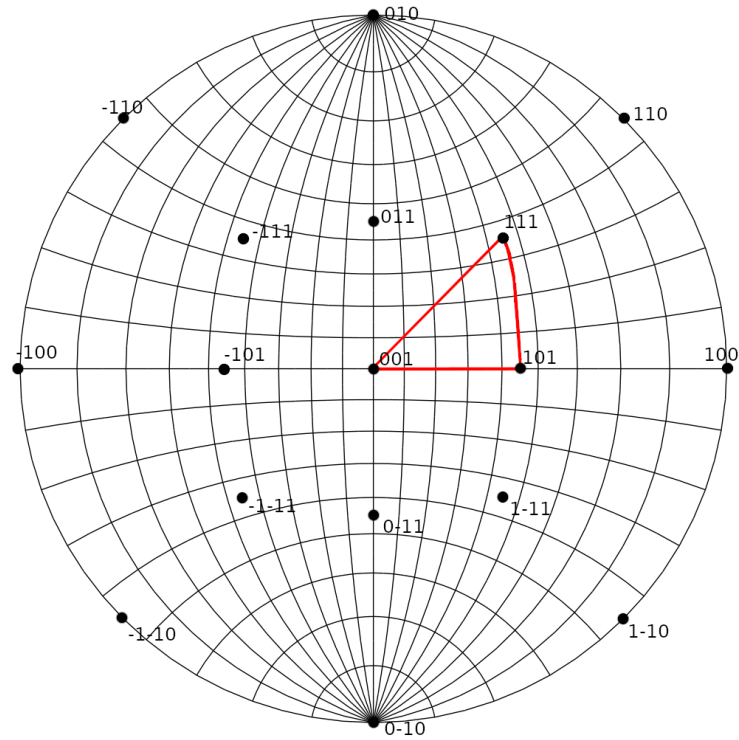
Figure 2.4: Wulff net and the low index surfaces are marked. The triangle represents an inverse pole figure (IPF), which is used in this work for describing the crystal orientation dependent properties.

In this work, all presented data is shown angle-preserving in an inverse pole figure (IPF) form, which will be explained below. The Lambert azimuthal equal-area projection is used for statistical issues, e.g. calculating the mean sputter yield or mean oxidation rate.

2.3 Inverse pole figure

A pole figure is a stereographic projection and includes all 24 symmetric elements for cubic crystal structures[18]. For a cubic crystal lattice, an IPF is $1/24^{th}$ of a pole figure, shown in figure 2.4 as a red triangle. The IPF is a reduced representation of all 24 symmetric elements of a pole figure into a triangle. The IPF represents all possible crystal orientations and is therefore suitable to present properties such as sputter yields as a function of crystal orientation. Often, the color code of an orientation map is presented in such an inverse pole figure for visualizing crystal orientations of a polycrystalline sample. An example of a color coded IPF triangle and a measured W sample for a cubic lattice can be seen in figure 2.5.
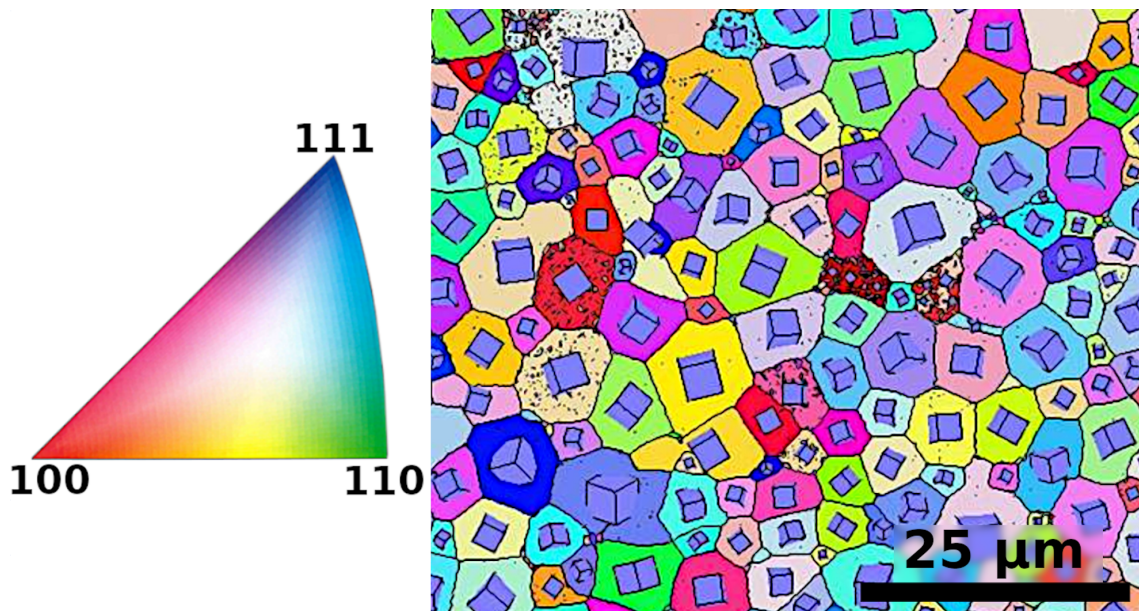
Figure 2.5: Crystal orientation map with cubes as illustration for the crystal orientation. The color coded IPF on the left side shows the crystal orientation for the orientation map derived by EBSD. The IPF is only valid for a cubic lattice.

2.4 Sputtering

The sputter process was discovered over 150 years ago[25,26,27]. At that time the process was called "cathode sputtering", because the cathodes erode during an electric gas discharge. The sputter process describes the removal of surface atoms of the target by energetic particles[28]. Accompanied with sputtering, other surface processes appear[29,30,31], such as ion implantation and secondary electron emission, which are illustrated in figure 2.6.

Physical sputtering is very different from chemical sputtering. Chemical sputtering is a procces where high energetic ions react with the target material, e.g. hydrogen and carbon react to a hydrocarbon compound. This increases significantly the sputter yield. In this work, the focus is on physical sputtering.
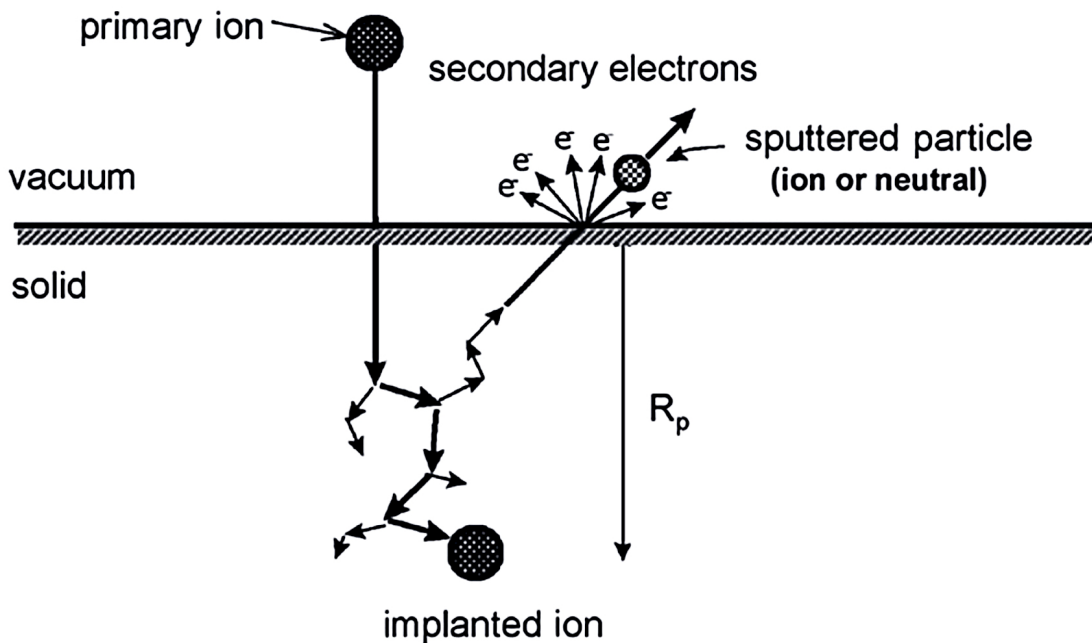
Figure 2.6: Schematic diagram of ion-solid surface interactions happening during a physical sputtering process[32]. R_p represents the implantation depth.

During physical sputtering, the primary ion is elastically scattered and can backscatter to the surface. If the backscattered ion hits a target atom, the target atom will be sputtered only when the energy transfer by the backscattered ion to the target atom is larger than the surface binding energy of the target atom. This energy transfer is called nuclear stopping. Beside nuclear stopping, also electron stopping appears, specially for higher energies it becomes dominant due to the kinetic energy. Figure 2.7 shows the nuclear and electron stopping as a function of the primary ion velocity. Nuclear stopping depends also on the atomic mass and for the condition
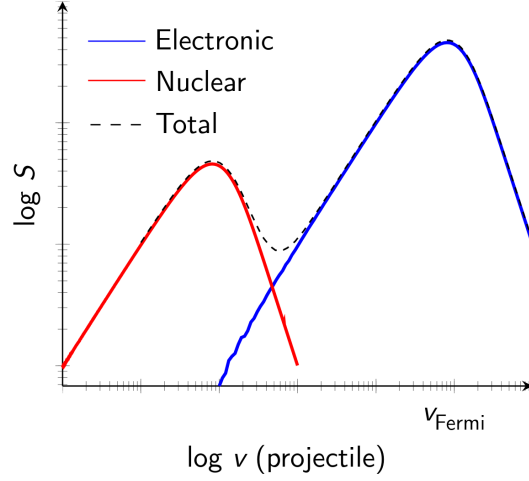
Figure 2.7: "Qualitative picture of stopping power as a function of projectile velocity. At high velocities, when the projectile travels at speeds comparable to those of the electrons, the electronic stopping power dominates. At low velocity nuclear stopping becomes relatively more important depending on the type of projectile."[33]

$E_0/A \leq 1\,\text{keV/u}$, where E_0 is the energy of the incident ions and A is the atomic weight, nuclear stopping is dominant.

In this work, sputter experiments were performed with a $2\,\text{keV}$, $8\,\text{keV}$, $30\,\text{keV}$ gallium ion beam and a $2\,\text{keV}$ D ion beam. For both ion beams, the energy of ions is low enough and they fulfill the requirement of $E_0/A \leq 1\,\text{keV/u}$. It means that the energy loss of the projectile in the target is dominated by nuclear stopping[34].

Nuclear stopping describes the energy transfer of the primary ion to the target ion, which occurs with and without electron shielding. When the electrons do not shield the charge of the nucleons, the distance r between the charged ions is far smaller than the Bohr radius a_0. Under this circumstance, i.e. $r << a_0$, the Coulomb potential is dominant:

$$V(r) = \frac{Z_i \cdot Z_t e^2}{4\pi\epsilon_0 \cdot r}, \tag{2.6}$$

where Z_t and Z_i are the atomic numbers of the target atom and the charged ion respectively, e is the elementary charge and ϵ_0 is the dielectric permittivity of the vacuum. For larger distance ($r > a_0$) the electrons shield the charge of the nucleons. Therefore, a screening function based on the Thomas-Fermi model is multiplied to the Coulomb potential[35]. Lindhard made a good approximation for the screening function[36]:

$$\phi(r, a_L) = 1 - \frac{r}{\sqrt{3a_L^2 + r^2}} \tag{2.7}$$

12

where a_L is the Lindhard screening length which is defined as:

$$a_L = \frac{0.885 \cdot a_0}{\sqrt{Z_i^{\frac{2}{3}} + Z_t^{\frac{2}{3}}}}. \qquad (2.8)$$

For simulation programs the screening function is more complex as the screening function from Lindhard and an universal screening function is often multiplied to the Coulomb potential which is[37]:

$$\phi(r, a_L) = 0.1818e^{-3.2\frac{r}{a_L}} + 0.5099e^{-0.9423\frac{r}{a_L}} + 0.2802e^{-0.4029\frac{r}{a_L}} + 0.02817e^{-0.2016\frac{r}{a_L}} \qquad (2.9)$$

The energy transfer of a 30 keV Ga ion beam to the electronic system is below 10 %. Specially for channeling conditions or for higher energies, the electronic energy loss becomes dominant[34,38]. One popular theory published by P. Sigmund[39] is based on the Boltzmann transport equation. It is assumed that energetic ions or recoil atoms result in cascades of atomic collisions. The majority of sputtered atoms originated from a thin surface layer of around 5 Å. The ratio of released/sputtered target atoms to high energetic impacting ions is called sputter yield.

For the sputter experiments in this work, the sputter yields (SY) were calculated as a function of the focused ion beam (FIB) current I, the sputter time t, the erosion height h and the sputtered area A:

$$SY = \frac{h * \rho}{I * t} * A, \qquad (2.10)$$

where ρ is the atomic density of W. For crystalline targets, the sputter yield can change over one order of magnitudes due to the crystal orientations[8,9,10,11,12]. The main reason for such a big difference is channeling: If the incident ion channels into the crystal lattice, it will not deposit energy at the surface, because it does not collide with a target atom near the surface.

Channeling is a phenomenon known over decades[36,40,41,42]. In contrast to an amorphous target, a crystalline target, especially a single crystal, has a structure with well ordered atoms. In some crystal directions, often the low index surfaces, the lattice atoms are in a row as shown in figure 2.8 (a). After a rotation of the crystal lattice, as shown in figure 2.8 (d), the channels are not "visible" and a high energetic ion will collide with atoms near the surface. There are two types of channeling, axial and planar channeling[34,36,43,44]. The planar and axial channels are often at the low index directions.
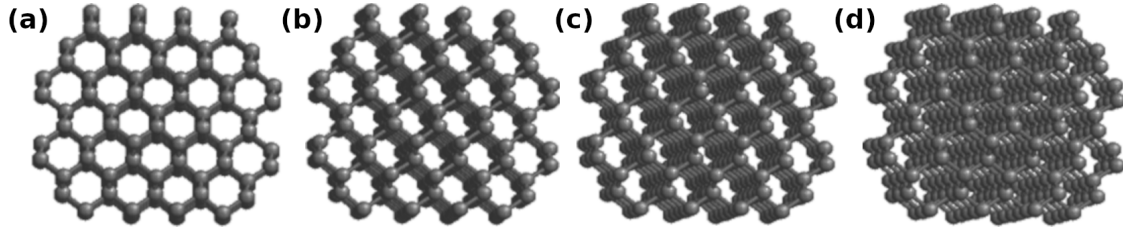
Figure 2.8: Crystal lattice of a diamond[45]. (a-d) show four different rotation states of the crystal lattice. A channeling direction is clearly shown in (a), while the channels are invisible in (d).

A high energetic ion can enter such a channel and does not deposit the energy through atom collisions close to the surface. Because of the positive charges, the ions repel each other. As shown in figure 2.9 the ions oscillate in such a channel. A high energetic ion can dechannel if the impact angle Φ is too big. Lattice defects or implanted ions can induce dechanneling as well.
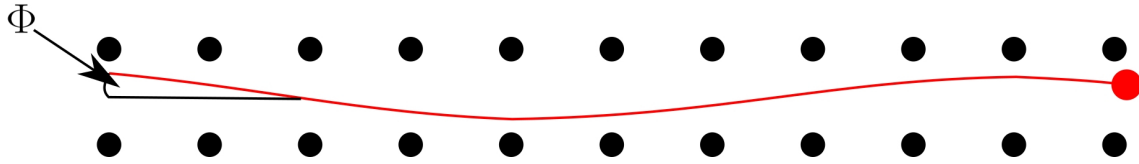
Figure 2.9: Schematic diagram showing the channeling process of a charged particle in a crystalline solid. The black and red dots represent lattice atoms and an energetic ion, respectively. The red line shows the traveling path of the energetic ion.

Lindhard made a classical approximation for the critical angle of axial channeling[36]:

$$\Phi_{C_{ax}} = \sqrt[4]{\frac{3a_L^2 Z_t Z_i e^2}{4\pi\epsilon_0 E d^3}} \qquad \text{(rad)} \qquad (2.11)$$

where a_L is the Lindhard screening length (equation 2.8), Z_t and Z_i are the proton numbers of the target atom and the charged ion, e is the elementary charge and ϵ_0 is the dielectric permittivity of the vacuum, d is the lattice constant in Å and E is the energy of the ion.

The critical angle for planar channeling is[36]:

$$\Phi_{C_p} = \sqrt{Nd}\sqrt[3]{\frac{a_L^2 Z_1 Z_2 e^2}{4\pi\epsilon_0 E d^3}} \qquad \text{(rad)} \qquad (2.12)$$

where N is the number density of the target, and d is the interplanar spacing (equation 2.1). Lindhard[36] described two parts of an ion beam, which are in the direction of crystal lattice channels. One part is called the aligned part of the beam and the other is called the random part of the beam. Onderdelinden[46] called the

random part of the beam nonaligned beam and assumed that only the nonaligned part of the ion beam contributes to the sputter yield. The aligned beam channels into the crystal lattice and does not contribute to the sputter yield, as the incident ions loose their energy in a depth far below the surface. This assumption is still valid nowadays and many researchers simulate sputter yields in accordance with experimental results under these assumptions[47,48,49].

Beside channeling, linear collision sequence occurs in crystalline targets. A linear collision sequence is a phenomenon where each atom collides with its neighbor along a closely-packed row of atoms[50]. There are replacement collision sequences and focusing collision sequences. The last one is also called focuson. A fucoson gives the energy through collision to the neighbor atom but remains at its position in the lattice. By a replacement sequence, the atom collides with its neighbor and replaces it. The contribution of the linear collision sequence to the sputter yield is highly discussed[51,52]. As Robinson said[53]: "The quantitative interpretation of experiments in this area contains many uncertainties, but there is convincing evidence[54,55] that linear collision sequences do occur and that they are an important factor in the development of displacement cascades. There is equally convincing evidence from recent low energy transmission sputtering experiments in gold[56,57] that such sequences are not extremely long ones as has sometimes been suggested. Further experimental and theoretical investigations of these points are needed to resolve the many uncertainties remaining."

In this work, the sputter yields of thousands crystal orientations were evaluated to give a solid experimental data set for this kind of questions.

2.5 Oxidation

In nature, pure metallic W does not exist, but it is available in the form of W oxide like ferberite ($Fe^{2+}WO_4$). To produce W powder, W oxide was reduced at around 1000 K in a hydrogen atmosphere[17].

Oxidation is a chemical reaction process. Atoms, ions or molecules, e.g. W, release electrons to elements like oxygen. W is oxidized and the oxidation number is increased. Oxygen collects the electrons and is therefore reduced. Both reactions together are called redox reaction[17]. In this work, W was oxidized mainly to WO_3 with the following reaction:

$$W + 3O \rightarrow WO_3 \tag{2.13}$$

Besides, there are several different sub-types of W oxide and the major ones are $W_{20}O_{58}$ ($WO_{2.9}$), $W_{18}O_{49}$ ($WO_{2.72}$) and WO_2. The sub-types of W oxides have different colors at room temperature, which is shown in figure 2.10.
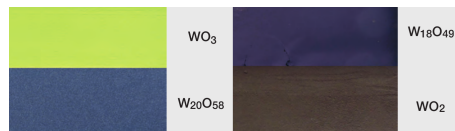
Figure 2.10: Colors of four different W oxides appearing in a dry atmosphere and at room temperature[58].
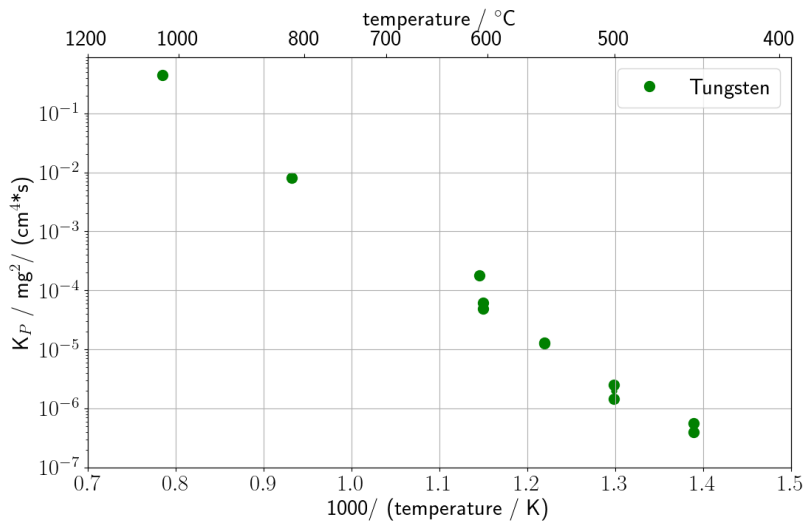
Figure 2.11: Parabolic oxidation rates (K_p) of W[59].

The oxidation rate depends strongly on the temperature. From room temperature to 200 °C the oxidation rate increases slowly. Above 200 °C the oxidation process increases rapidly and a humid atmosphere accelerates additionally the oxidation

16

rate. Figure 2.11 shows the increase of the parabolic oxidation rate as an Arrhenius plot. Above 750 °C W oxides start to sublimate.

The sublimation rate increases faster than the oxidation rate and at 1300 °C the sublimation rate corresponds to the oxidation rate[17]. Above 1300 °C, oxidation of a W sample remains in a nearly oxide free surface because the W oxides sublimate directly.

The temporal oxidation kinetics of W can be separated into the following sub-steps:

- Adsorption of oxygen on the surface (start of the oxidation –> fast oxidation)

- Diffusive transport of oxygen through the oxide layer to the metal interface (parabolic mass gain due to oxygen)

- Cracks in the oxide layer (linear mass gain due to oxygen)

For the experiments in this thesis, sublimation was avoided. Therefore, the oxidation experiments were performed in a temperature range of 400 °C to 600 °C. For resolving the starting phase and the parabolic phase of the oxidation, thin (nm range) and thick (µm range) oxide layers were investigated. The main goal of this work was to investigate the oxidation of "every" W crystal-orientation. Therefore, influences of cracks or oxygen partial pressure, which make the interpretation of the data difficult, were tried to be avoided. This means for this work, the thickness of the oxide layer was kept below 10 µm avoiding cracks, and the oxygen partial pressure was high enough that oxygen is not the limiting factor.

2.6   Tungsten etching with Murakami solution

Etching is a chemical process. In industry, etching chemicals are used to remove material or create an object with a desired shape. In principle, there are two different etching methods to create objects, deep etching and high etching. By deep etching the target object is not masked, while the target object is masked by high etching.

In this work a wet etching technique was used on a microscopic level. For this purpose a W sample was dipped into Murakami solution. This etching agent has two components, potassium ferricyanide $K_3[Fe(CN)_6]$ acting as oxidizing agent and sodium hydroxide (NaOH) acting as base agent. Different reaction cascades are possible, resulting in different kinds of tungstate, such as potassium tungstate (K_2WO_4), iron tungstate ($FeWO_4$), sodium tungstate (Na_2WO_4), sodium paratungstate ($Na_{10}W_{12}O_{41}$) and ammonium paratungstate ($(NH_4)_{10}W_{12}O_{41}$). These tungstates are dissolvable in the etching solutions, thus W atoms are removed from the sample surface. Removing crystalline W grains through etching is an anisotropic process. Here, the expression "anisotropic process" is used as a synonym of crystal-dependent etching[60,61]. The difference in etching rates of various crystal orientations can reach up to several orders of magnitudes.

3 Sample preparation and instruments

This section gives a detailed introduction to the experimental procedures and the used instruments. The samples for experiments were all supplied by Plansee SE (Austria). The standard sample was $12 \times 15 \, \text{mm}^2$ hot rolled W with a purity of 99.97 wt% (hereinafter named as as-received W). The samples were recrystallized, polished and pre-characterized before the oxidation, etching or sputter experiments were performed.

3.1 Recrystallization and grain growth

The recrystallization process provides a "defect-free" crystal lattice. Together with the formation of almost defect free crystal lattice, grains could grow over several µm length depending on the annealing temperatures and time. For this study, a suitable W grain size has a length of around 10 µm.

Recrystallization and grain growth of the as-received W were completed by annealing in a vacuum furnace named "HADES" at Max Planck Institut for Plasma Physics (IPP). HADES has two chambers with a lock in between. The main chamber of HADES was usually kept at a temperature of around 400 K and a pressure below 10×10^{-10} mbar. This operation reduced absorption of residual gases and ensured clean surfaces inside the furnace. During each annealing process, W samples (about 20 pieces) were firstly placed on a round W plate and then put on a sample holder made of W. The sample holder is located in the pre-chamber.
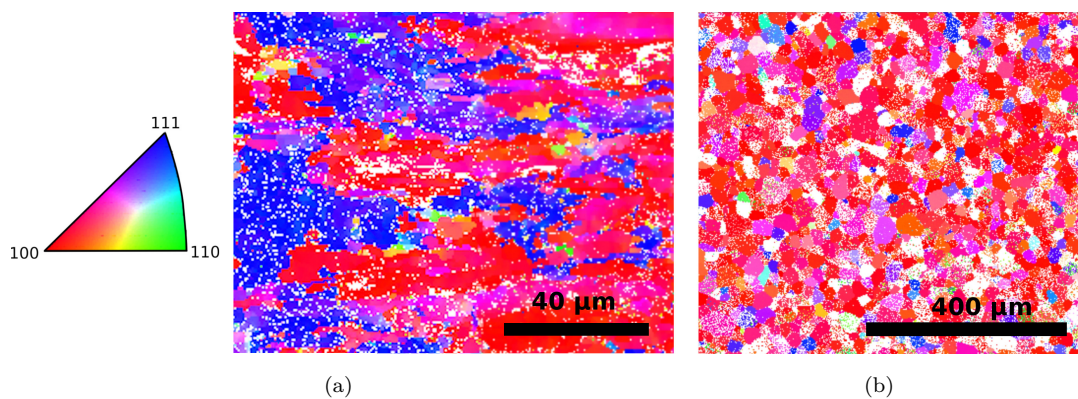
Figure 3.1: Crystal orientation maps of (a) as-received and (b) a recrystallized W sample. Please note the different scale bar.

The initial temperature measured at the sample holder was 295 K. The lock between pre-chamber and main chamber automatically opens when the air pressure in the pre-chamber decreases to a similar level to that in the main chamber. A heating

ramp was set to a target temperature of 2000 K. After holding the target at this temperature for 35 min, a cooling ramp was performed. During the whole ramp-hold-ramp procedure, the pressure in the main chambers was below 2×10^{-7} mbar. At the end, the samples were transferred to the pre-chamber and kept there over night under a pressure below 10×10^{-10} mbar.

The texture of the samples can change after the recrystallization[62], which was also observed in this work . The crystal orientation maps of the as-received and recrystallized W samples derived by EBSD are shown in figure 3.1. The blue regions represent W grains with $\langle 111 \rangle$ crystal orientation in respect to the surface, which were obviously reduced by recrystallization.

3.2   Grinding and polishing procedure

The samples were first ground using the machine "Phoenix 4000", which is shown in figure 3.2 (a), to achieve a flat surface over the whole sample surface.

(a)   (b)
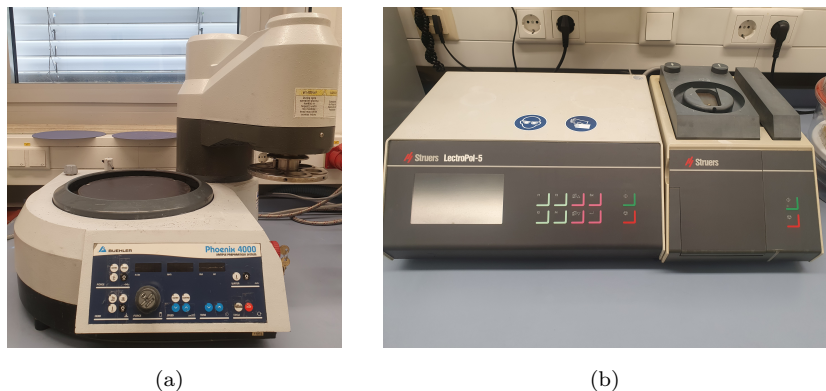
Figure 3.2: (a) Grinding machine Phoenix 4000; (b) Electron polishing machine Struers LectroPol-5.

During the grinding procedure, the W samples were fixed with a double-sided adhesive tape on six metal cylinders. All six metal cylinders together with the W samples were mounted into the grinding machine. The samples were cooled with water during the grinding process. As shown in table 1, several variables were adjusted to achieve a good grinding quality. Note that the grinding time was not the same for every sample, depending whether the surface was scratch-free.

After the grinding procedure, the samples were electro-polished using the machine "Struers LectroPol-5", which is shown in figure 3.2 (b), to produce surfaces with less defects through the mechanical polishing process. The electropolishing procedure was conducted in a 1.5 % NaOH electrolyte at a voltage of 19 Volt for 60 seconds per sample.

Table 1: Parameters of the mechanical grinding procedure for preparing mirror-like W surfaces.

Time / s	Force/ N	Rotation / RPM	Granular / P
30 - 60	45	150	400
30 - 60	45	150	800
30 - 60	45	150	1200
60 - 120	45	150	2500
60 - 120	45	150	4000

3.3 Confocal laser scanning microscope

The confocal laser scanning microscope (CLSM) is an optical imaging technique which enables to reconstruct a three-dimensional surface topology of a sample. The microscope resolves height differences in the nm range and is able to scan an area of several mm^2 in a few minutes. Therefore, reflected light from the sample surface is detected by the detector located behind a pinhole. The pinhole was for the elimination of the out-of-focus signal. The location of maximum reflection along the beam axis is defined as the point of the surface.
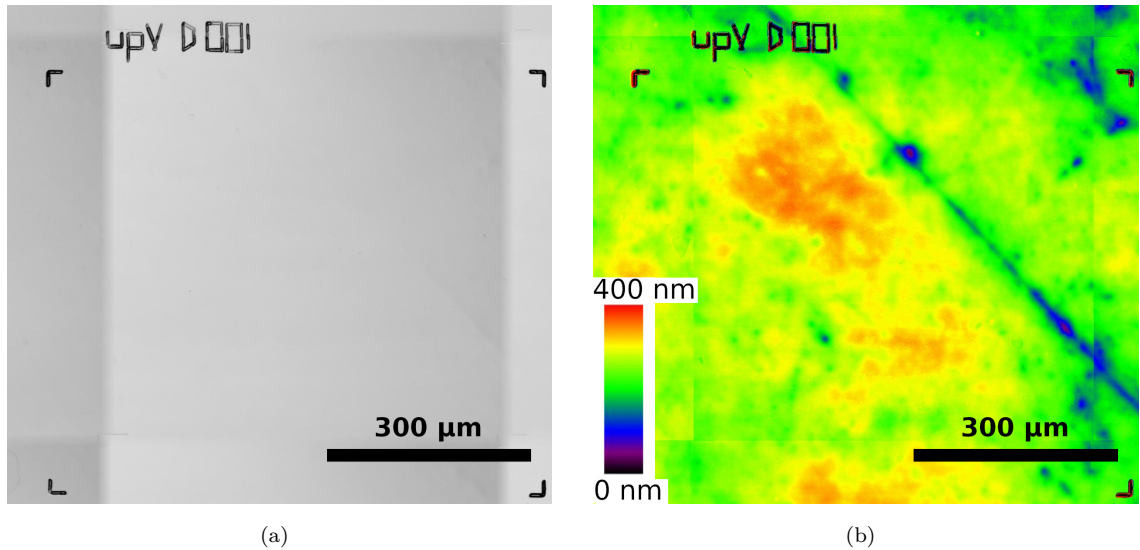
Figure 3.3: Pre-characterization of the polished W sample by CLSM: (a) intensity image, (b) height profile image. Four L markers and the sample name were engraved by FIB for locating the area-of-interest in different analysis systems. The maximal height difference shown in (b) is about 200 nm, which is acceptable for the experiments.

The intensity image provides a high contrast image scanned with a laser as a light source. The height resolution of the Olympus LEXT OLS4000 system can reach up to 10 nm. However, the stitching function of images was used in our experiments, which increased the lateral length to around 1 mm and finally led to a reduction of

the height resolution of 50 nm.

An example for the 3D surface profile of the samples after electropolishing as obtained with the CLSM is shown in figure 3.3. To locate the same area-of-interest in different microscope systems, four L markers and the sample name were engraved by using the FIB (see next subsection). Small scratches are still visible at the sample surface in figure 3.3, but they will not have a big influence on the results, since the area of a scratch is far smaller compared to the W grains (around 10 µm x 10 µm). The height differences induced by the experiments, such as oxidation and sputtering, were designed to be around 1 µm. Therefore, the height difference of below 200 nm (see figure 3.3), which originally existed on the polished samples, is acceptable for our experiments.

3.4   SEM, FIB and the analytics

The used HELIOS NanoLab 600 dual-beam is a scanning electron microscope (SEM) manufactured by the company FEI. It has an electron gun and a Ga ion gun. The electron beam was used to characterize the sample microstructures by forming secondary electron images, making compositional analysis by measuring the characteristic x-ray of the element (EDX), or making crystal orientation analysis by evaluating EBSD patterns. The Ga ion beam was used to prepare sample markers or to perform sputter experiments. Beside these functions, the SEM provides an extensive depth of sharpness, which is an important advantage in comparison to an optical microscope. Detailed descriptions about SEM and focused ion beam (FIB) can be found in[63,64,65].

3.4.1   Scanning electron microscope

The HELIOS NanoLab 600 has a Schottky field emission electron gun. After emission of electrons, the electrons are accelerated and manipulated by electromagnetic fields. This happens in the electron column where the electromagnetic lenses are located. Before the electron beam hits the sample, the electrons are focused to a spot. The spot size defines in principle the resolution of a SEM. The highest achieved resolution of a SEM is below 1 nm. At and below the sample surface, incident electrons interact with the sample atoms. Some primary electrons scatter, others generate secondary electrons or x-rays at the sample surface. Since the primary electron spot is in the nm range, the beam scans step by step and row by row. The standard secondary electron detector, an Everhard-Thornley-Detector, detects the secondary electrons within a few µs for one spot. For example, if the dwell time of the electron beam is 10 µs on each spot, an image with 1000 x 1000 pixels will take 10 s. This scanning principle applies not only to imaging but also to EDX measurements or to EBSD measurements.

3.4.2 Focused Ion Beam

The focused ion beam (FIB) was used in this study for the following four different tasks:

- Marking the sample with name and markers

- Inducing secondary electrons for image taking

- Preparing cross-sections to investigate the thickness of an oxide layer

- Sputtering larger areas, e.g. $700\,\mu m \times 700\,\mu m$

A FIB works in a similar way to an electron beam. The main difference is that the ions are typically generated from a liquid metal source. The HELIOS NanoLab 600 system generates Ga^+ ions in the source. The ions are accelerated and focused by electromagnetic fields. As illustrated in figure 3.4, the FIB column is mounted under a 52° to the electron column in the HELIOS NanoLab 600 system. Therefore, the sample stage is often tilted to a 52° angle so that the ions hit the sample surface perpendicularly. Back-scattered ions or secondary electrons generated from the sample can be detected for imaging. Since the HELIOS NanoLab 600 at IPP does not have an ion detector, the imaging was done by detecting the secondary electrons with the Everhard-Thornley-Detector. The focus of a FIB is not as good as an electron beam, but structures smaller than $10\,nm$ can still be resolved in this way.
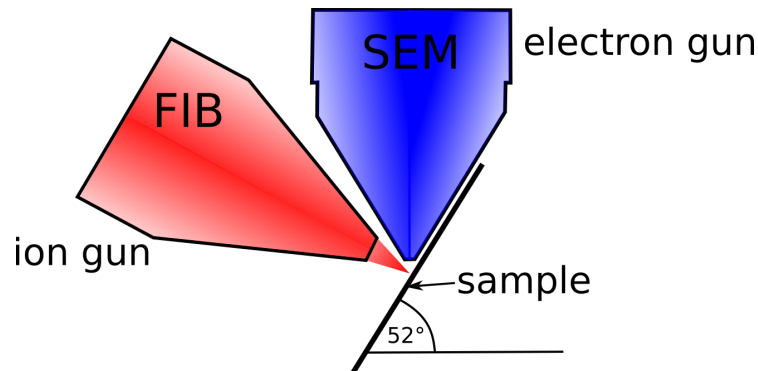
Figure 3.4: Schematic sketch showing a combined SEM - FIB working system.

Another typical application of FIB is the preparation of cross-sections, enabling to investigate the thickness of an oxide layer, or the microstructure below the surface. Prior to the preparation of cross-sections, a protective layer was deposited. Therefore, the gas trimethyl-(methylcyclopentadienyl)-platinum was injected and cracked with the electron or the ion beam. The thin protective layer contained carbon, platinum and hydrogen. Often it also contains Ga as long as the cracking of the gas was

done with the ion beam. The protective layer ensured that the rounding of the cross-section edge did not extent to the interesting part of the cross-section, thus ensuring a precise measurement of the layer thickness. Since the FIB and the electron beam can simultaneously focus the same area at the eucentric point, it is possible to take an electron image under $-38°$ to the cross-section surface normal. Taking images and cutting a cross-section, without moving the sample, is an important advantage of a dual beam device.

A part of the sputter experiments in this work was performed by using the FIB. The technique of sputtering an area as small as $20\,\mu m \times 20\,\mu m$ and with various geometries is usually used to make markers on the sample. The sputtering of large areas is beneficial to investigate crystal-orientation dependent sputtering behavior of W, see section 6.1.

3.4.3 Precharacterization with EBSD

Nowadays, electron backscatter diffraction (EBSD) is a standard technique for detecting crystal orientations on microscope level length scale. The EBSD detector has been greatly improved over the recent years. Nowadays, the detection speed is around 1000 times faster than in the last decade[16]. Therefore, in this work, the Oxford/HKl Nordley II detector was updated to a CMOS-based EBSD detector (Oxford Instruments Symmetry). This update allows identifying millions of crystal orientations in hours.
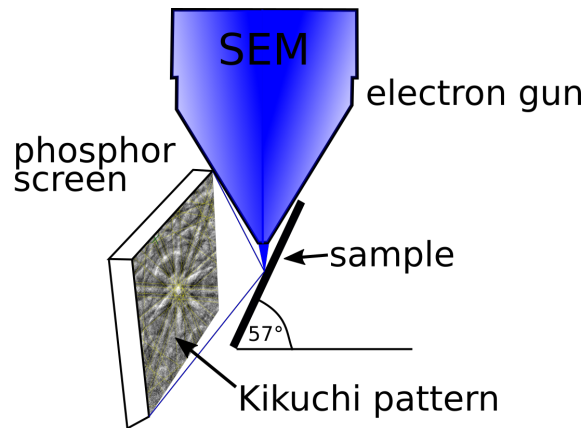
Figure 3.5: Schematic sketch showing an EBSD measurement system.

The principle of crystal orientation identification by EBSD is visualized in figure 3.5. To detect the crystal orientation, the sample was tilted in our system to a maximal tilt angle of 57°. For a better measurement performance and quality, a pre-tilt sample holder should be used to reach a total tilt angle of 70°. Under such an angle, a larger fraction of electrons forward-scatters in the lattice planes as under

a tilt angle of 57°. The electrons, which fulfill the Braggs's law, contribute to a constructive interference. The Braggs's law is defined as

$$\lambda n = 2 \cdot d \cdot \sin(\Phi_B) \tag{3.1}$$

where λ is the wavelength of the electrons, n is the order of reflection, d is the distance between two planes and Φ_B is the Bragg angle. One crystal plane gives two diffraction cones, resulting in two lines on a phosphor screen. The lines are known as Kikuchi lines. Several crystal planes result in several line pairs in space and the arrangement is characteristic for a specific crystal orientation. This arrangement is visualized in figure 3.5 and known as a Kikuchi pattern.

The Kikuchi patterns were resolved by the Oxford software AZtec. After scanning the sample surface using the electron beam of a SEM, an EBSD orientation map was generated and exported as a ".ctf"-File. The file contained the Euler angles, the coordinates of the position and the phase. These were the needed information for the evaluations.

3.4.4 Energy dispersive X-ray spectroscopy

EDX is used to make compositional analysis of the sample surface or the FIB prepared cross-section. As shown in figure 3.6, the primary electron beam hits and kicks out an electron from an inner shell, e.g K shell, leaving behind an exited atom with a vacancy. This "hole" will be filled by an electon from an outer shell and the released energy is emitted by a X-ray photon, which is characteristic for the involved shells and elements. In another possible elementary process the relaxed energy is transferred to an outer shell electron, so called Auger electron, which leaves the atom.
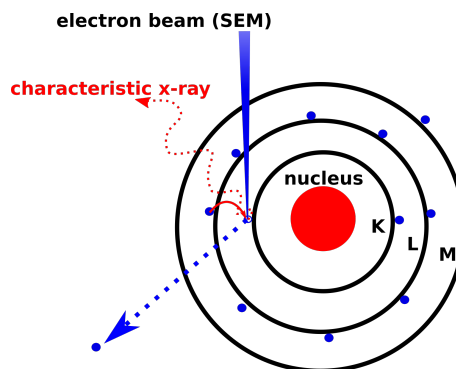
Figure 3.6: Schematic sketch showing the generating mechanism of a characteristic X-ray in a SEM for elemental analysis.

25

4 Python tool: Merging and evaluation of the data

As already mentioned, the EBSD measurement technology was improved over the last decade. The measuring speed increased of a factor of $1000^{[16]}$. Thus, a huge amount of EBSD data can be acquired much faster. To correlate the data generated from different measurement systems (e.g. EBSD data and CLSM data), a python tool was written to improve the work efficiency.

The huge amount of EBSD data gave an opportunity to enhance the results of crystal-dependent data evaluation, e.g. by filtering. With continuous development of data acquisition and evaluation, it turned out that different investigated properties could be optimized in different ways. In this section the basic python tool is introduced, which includes merging of the data, automated data selection and filtering, and data visualization. The description of the python tool can also be found in[66].

4.1 Difference microscopy

Difference microscopy is an optional step and must be applied before the merging procedure. It is essential for resolving small height differences or for surfaces which are rough before starting the experiment. The height data of the CLSM of the polished surface as well as the height data after the experiment are needed. Both CLSM data sets are visualized as images and at least 4 reference points have to be selected, which define an area in the image. The data of the selected areas will be subtracted. Afterwards a plane of the subtracted data is fitted to level the data sets. The leveling was applied, because very often a small misalignment angle was found in the data due to mounting of the sample into the microscope. After performing the evaluation of difference microscopy, the resulting data is used for the following merging procedure. In this work, this technique was relevant for D sputtering on tungsten heavy alloys, because the sample polishing results in a rough surface before the sputter experiment is performed.

4.2 Merging of the data

Merging image data obtained from different measuring systems has not only to deal with a displacement between the two coordinate systems. 3D rotations, differences in magnification, and image distortions are just a few examples of problems that must be taken into account during the merging process. In[67], the data was merged by a manual procedure. In[66], we propose an automated procedure executed by a python tool developed to combine the data from two different microscopes. The

algorithm of the procedure is visualized in the chart presented in figure 4.1.
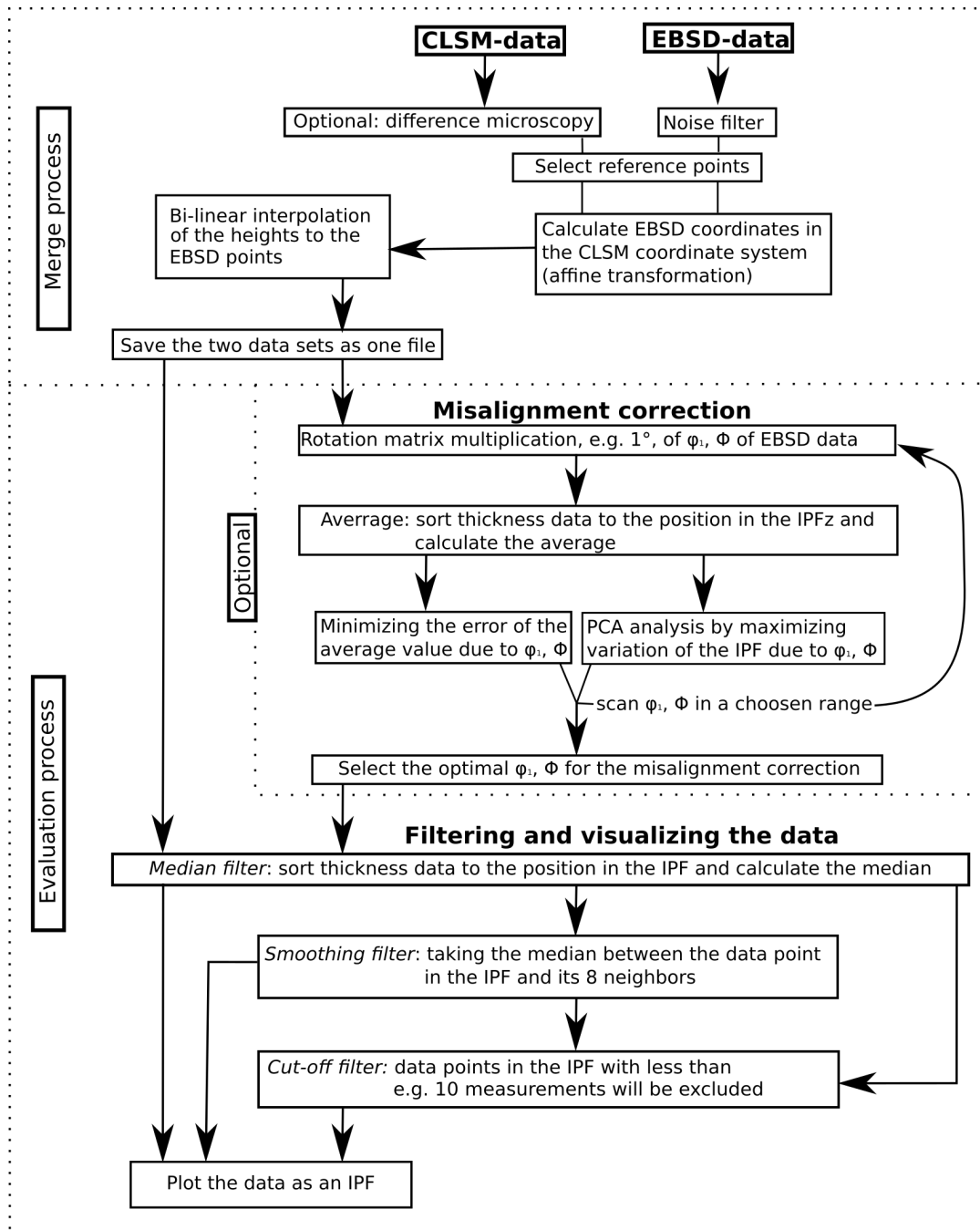
Figure 4.1: Chart of the python tool illustrating the merging and evaluation process.

Figure 4.2 illustrates a typical example of data merging (figure 4.2(c)) of the height information (figure 4.2(a)) and the crystal orientation data (figure 4.2(b)). The EBSD data was plotted by color-coding the three Euler angles, while the height

information obtained by CLSM was visualized by using a gray scale and a shadow effect for a better grain visualization.

In figure 4.2 several markers prepared by FIB are visible too, which were initially used as reference to find the approximate alignment between the two images. White arrows point to those markers. The markers are 2 µm wide and 20 µm long, but are not the best reference points for the merging procedure. The intersections of three grain boundaries are far better and lead to better merging quality. Thus, the markers were used as a first approach to roughly merge the images, subsequently the same grain intersections on both images were used in a second iteration for optimizing the merging process.

After the selection of these reference points on both images, the tool calculates the new EBSD coordinates in the CLSM reference frame by using the python class scikit-image for the affine image transformation[68]. Still, the EBSD space coordinates are slightly different to the CLSM coordinates, e.g. the CLSM data has the coordinate X=10.000/Y=10.000 and the corresponding EBSD coordinate is X=10.001/Y=10.015. Therefore, the heights were assigned to each pixel in the EBSD map. The exact space coordinates of the EBSD were calculated by a bi-linear interpolation of the CLSM data. As the pixel step size in the CLSM data is smaller (the amount of measurements is higher) than in the EBSD data, the data amount is reduced. An overlay of the two microscope pictures indicates the final result on the merging quality as shown in figure 4.2(c).

If the final result on the merging quality is still not satisfactory, additional points may be selected to refine the reference frame transformation. The scikit-image class supports an unlimited number of distinctive points selected in both pictures to improve the affine transformation by correcting deformations. By experience, between 5 to 12 points were typically necessary for a measurement area of around $1\,\text{mm}^2$.

After merging the new coordinates for the EBSD data, the three Euler angles and the height information were combined and saved in one single output file for the evaluation process. The merging with the python tool showed to be more accurate and much more efficient than the methodology used in the previous work[67]. This is because the manual merging only used the four FIB markers at the corners for the alignment of the images, and only a few points of selected orientations were analyzed. Since the new merging tool typically uses more than 4 points (see above) to perform the alignment of the images, a better merging quality is achieved, and more importantly the whole image could be used to extract information on the influence of "all" crystal orientations.
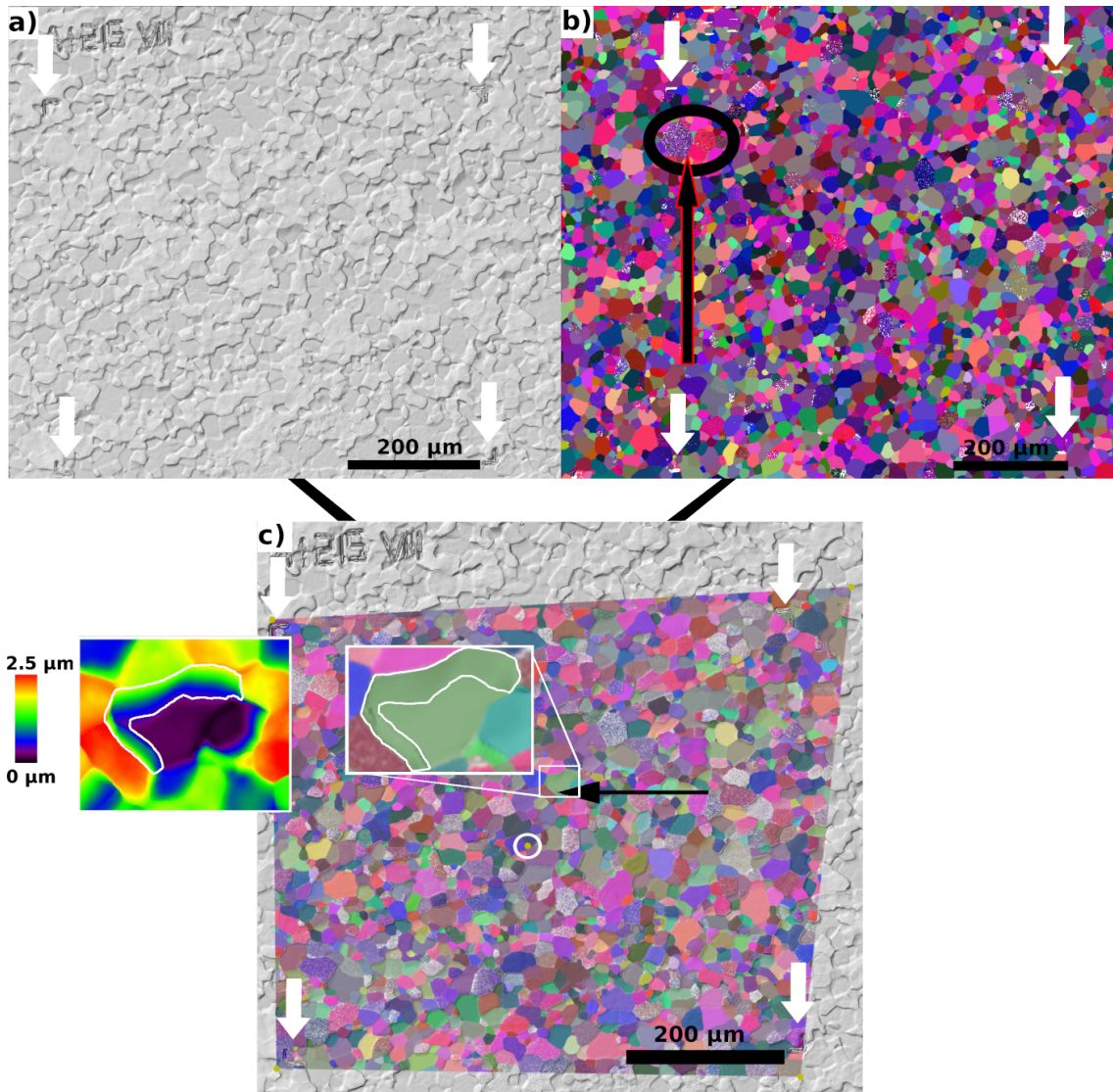
Figure 4.2: (a) CLSM height map coded in gray scale with shadow effect. (b) EBSD orientation map showing the 3 color coded Euler angles. (c) visualization of the merged data sets from (a) and (b) illustrating the merging quality of the data sets from the CLSM and EBSD microscopes. Four L-shaped markers, indicated by white arrows, are used for aligning the CLSM and EBSD data on a tungsten sample. The sample name labeled by FIB is shown clearly on the top left side of (a) and (c). The noisy EBSD areas, indicated by a black ellipse in (b), were eliminated during the data evaluation. The four corners and the center, which are indicated by the yellow points in (c), are the selected positions for the data merging procedure. The color coded height profile map of a representative region (highlighted by a white square) is shown on the left side of (c) with a higher magnification. A grain boundary with pronounced height profile, indicated by the black arrow, is clearly visible.

4.3 Automated data selection and filtering

The goal was to correlate properties like oxidation rates with the surface crystal orientation of tungsten grains. A standard graph to visualize crystal orientation is an IPF. The IPF is a representation of all possible orientations in respect to one direction, here the surface normal "z" (IPFz), i.e., each combination of the 3 Euler angles is assigned to one point in the IPFz. This is described in section 2.2 equation 2.2.
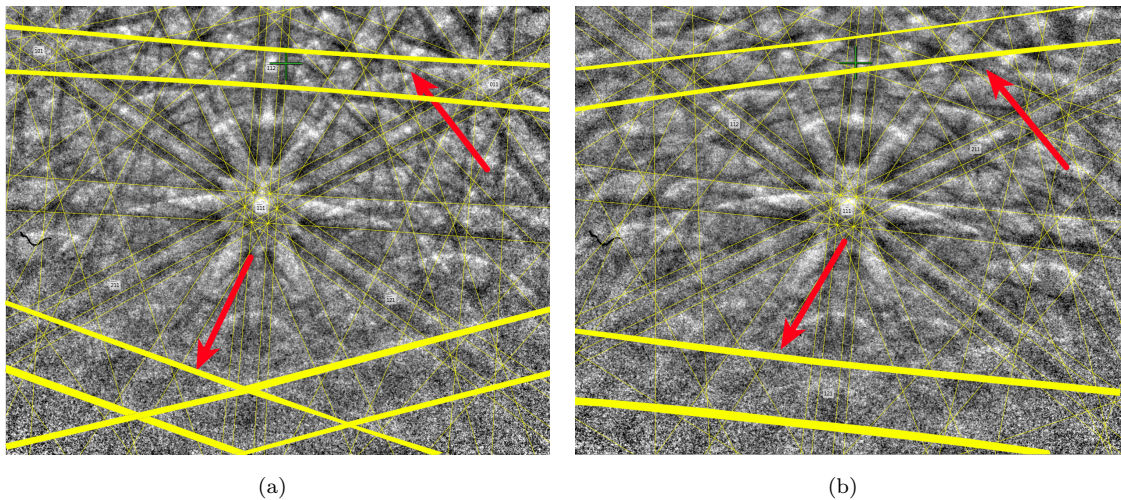
Figure 4.3: Kikuchi lines of the same crystal lattice, showing different solutions by automatic Oxford EBSD solving algorithms: (a) correct Kikuchi and (b) incorrect Kikuchi lines solved by automatic Oxford EBSD solving algorithms. Differences of (a) and (b) are highlighted by the red arrows.

Often thousands of EBSD measurements lay very close to each other, which means that single crystal grains has a similar surface orientation. Therefore, the measurements are sorted in clusters. The orientation range in one cluster is around 0.2°. The scatter of the Euler angle determination and therefore the crystal orientation is assessed to a few degrees, because several measurements are combined and the different samples have a misalignment error through sample mounting. This misalignment can be corrected in the evaluation, which will be described later. Several areas on different samples were measured and these data were combined to one data set, i.e., IPFz plot. All IPFz plots contain millions of measured data points. Therefore, it is reasonable to apply filters to enhance the data quality.

The first quality enhancement was performed on the EBSD data itself. A typical error is the miss-indexing by the automated pattern solving algorithms leading to wrong Euler angles. This leads mostly to isolated indexed data points in the orientation map (spikes), but for some specially orientated grains, the patterns of two orientations were very similar and the solution tends to oscillate between both. In

figure 4.2(b), a grain, which led to different solutions, is marked by a black circle. The oscillation is visible by two different colors (patchwork grains).

Obviously in this case, the Kikuchi lines are wrongly indexed, which is shown in figure 4.3. To remove such data, a noise filter was applied on the EBSD data, which bins 2 x 2 pixels and calculates the variance of the position in the IPFz plot. If the variance is bigger than 30 pixel in the IPFz, which corresponds to a misorientation angle of around 6°, all 4 points will be removed from the data set. In a second step, the binning and removing of the data points were once repeated, but the starting position of the binning process was shifted by one pixel to the right and one pixel down. So, if one EBSD data point is a spike, the incorrect data point and the 6 data points next to it will be removed. In addition to the spikes and the patchwork grains, the data points at the grain boundaries, which are not reliable, will be partially erased, too. Overall, this noise filter removes correctly and wrongly indexed data points, but due to the large number of available data points the slight reduction of statistic is negligible.
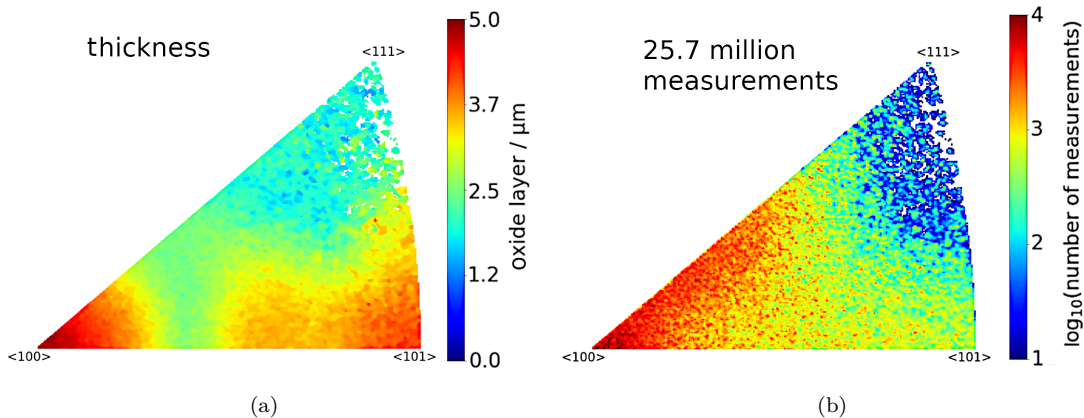
Figure 4.4: Evaluation results of oxidation experiments performed at 600 °C for 0.5 h: (a) oxide layer thickness versus crystal orientation after applying all three types of filters introduced in figure 4.1, (b) measurement numbers versus crystal orientation. For each pixel, the median was calculated of up to thousands of thickness measurements. The texture of the sample is visible in (b), because a lot of measurements were evaluated at the $\langle 100 \rangle$ corner.

For data sets evaluated in this work, typically one pixel in the IPFz plot results from several thousand of measurements as visualized in figure 4.4(b). Therefore, the standard deviation of the height values for all these measurements was chosen as a statistical indicator for the amount of variation between the measurements. The standard deviation is shown without and with the above described noise filter in figure 4.5. The reduction of the standard deviation due to the noise filter is 20% (100 nm), which is mainly caused by the wrongly indexed EBSD patterns and the partially removed data points along the grain boundaries.

The oxide layer thickness variation at the grain boundaries is shown in figure 4.2(c).

(a)   (b)
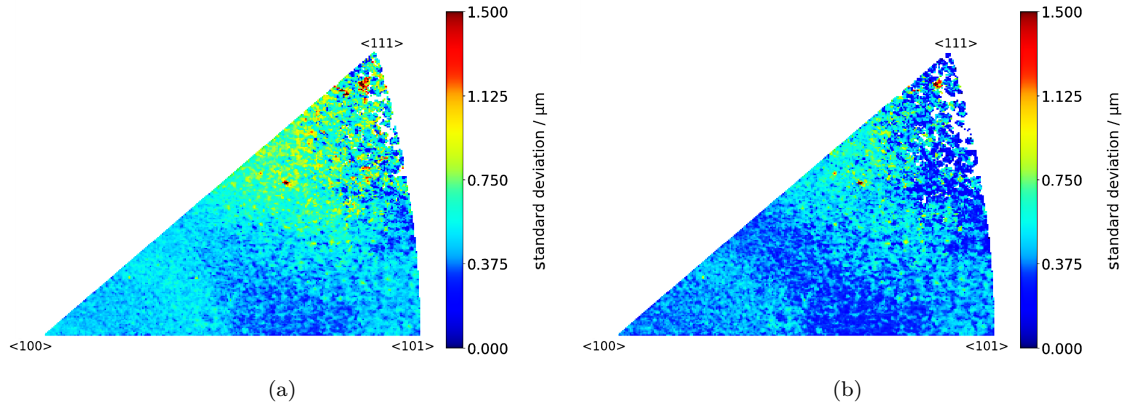
Figure 4.5: Standard deviation of the height measurements in figure 4.4(a): (a) without a noise filter for the EBSD data, (b) with a noise filter for the EBSD data. For each pixel, the median was calculated of up to thousands of thickness measurements. The average of standard deviation over all crystal orientations is $0.5\,\mu m$ in (a) and $0.4\,\mu m$ in (b), respectively.

The grain boundaries were only partially removed by the noise filter of the EBSD data, i.e. the influence of the boundary extents more than only some pixel in the orientation map into the grains. Therefore, the median instead of the mean of the height values was taken for each cluster (median filter), which was used for IPFz plot as shown in figure 4.4.

Since the cluster size of around $0.2°$ is an oversampling of the data, the neighboring pixels in the IPFz plot should be similar. Consequently, the median of thickness values from each pixel in the IPFz plot with its direct eight neighboring pixels was taken as a smoothing filter. This erases spikes in the IPFz plot.

Some crystal orientations were not present in the analyzed area of the polycrystalline W samples used in this study, which resulted in white areas in IPFz figures. Isolated pixels often existed in this white areas, which resulted from less than 10 measurements. These pixels exhibited an unusual oxidation rate and were assessed as unreliable. As over 20 million measurements were evaluated for figure 4.4 and a grain resulted in at least several 100 measurements of the crystal orientation and of the heights, an additional filter was applied to remove these pixels. Each pixel in figure 4.4 resulting from less than 10 measurements was excluded in the IPFz plot (cut-off filter). In general, the cut-off filter is flexible and depends on the total data amount. Figure 4.4(a) shows the final result after applying the noise filter to the EBSD data, taking the median of all measurements assigned to each pixel in the IPFz plot (median filter) and applying the smoothing filter and the cut-off filter (see figure 4.1).

33

4.4 Misalignment correction

The misalignment correction was developed after the first sputter experiments with deuterium, because of a misalignment error of 5° of the surface to the ion beam became obvious in some cases. This correction is an optional step, but for misalignment error bigger than 2° it increases the data quality significantly. For correcting the misalignment angle, a rotation matrix multiplications was applied on the merged data sets with equation 2.5.
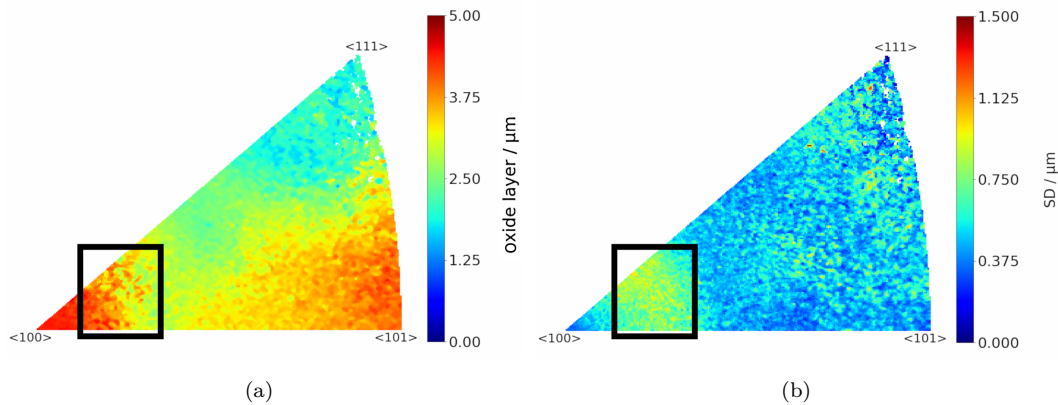
Figure 4.6: Thickness of oxidation layers measured with a misalignment angle of 5°. The average of standard deviation over all crystal orientations is 0.1 µm higher by a misalignment of 5°, which is a significant increase of the error. The black rectangle shows an area with a strong variation of the oxidation rates. Specially there the error is high.

To illustrate this, the data were reevaluated with a slightly misalignment angle. Figure 4.6(a) shows the reevaluated data of figure 4.4 with a misorientation angle of 5°. After the reevaluation, the average standard deviation, shown in 4.6(b), is 0.5 µm and 20% higher than for the data in figure 4.5(b).

This concludes that the experimental setup and workflow, like mounting the sample in different devices, should be better than at least 5° to get a correlation between crystal orientation and a property, e.g. oxidation. Specially, if the investigated property is sensitive to the angle, e.g. impact angle during sputtering, an exact known angle is important. The correction of the impact angle and the optimization procedure will be discussed in detail in sections 6.3 and 6.4.3.

4.5 Summary of the Python tool

A Python tool was developed to correlate data obtained from two different measuring systems. An affine transformation was used to correlate different data sets. With this method, millions of data points were merged, making it reasonable to apply filters to enhance the quality.

After demonstrating the reliability of this Python tool in combining different data sets, it was applied to investigate different kinds of properties, including crystal orientation dependent sputtering, etching and oxidation. Results to them are presented in the next sections.

5 Oxidation of tungsten

A lot of research focuses on the application of W oxides[69], while some other research aims at the avoidance of the oxidation of W at elevated temperatures[70] [71]. In the field of semiconductors, such as solar cells[72] [73], photocatalysis[74], water splitting[75], sensors[76], and electrochromic devices[77], W oxidation has attracted a great attention from scientists and engineers. On the other hand W is a promising plasma-facing material in nuclear fusion reactors. However, in the case of a loss of coolant and a simultaneous ingress of air, activated tungsten oxide could be formed and sublimated, ultimately leading to a potential safety issue if the volatile tungsten oxide is released into the environment[78]. Recent research indicates that the production of volatile W oxides can be strongly suppressed when using self-passivating tungsten alloys[79,80,81,82].
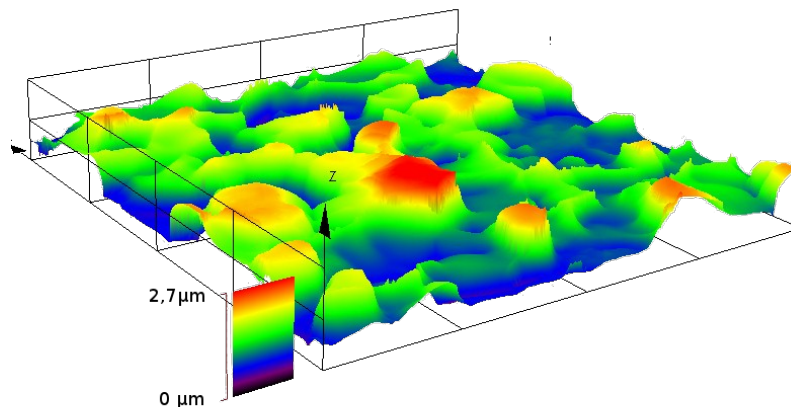
Figure 5.1: 3D CLSM image of a tungsten sample oxidized at 600 °C for 30 min in a 20 % oxygen/argon atmosphere, showing clearly the height differences among the tungsten grains.

Oxidation is a very complex process, as it is correlated with the absorption of oxygen onto the sample surface and further diffusion of oxygen into the bulk material[17]. It is known that oxidation is crystal orientation dependent[83] [84] [85]. Figure 5.1 is a 3D CLSM image of a tungsten sample oxidized at 600 °C for 30 min in a 20 % oxygen/argon atmosphere. Height differences among the different grains, induced by the fact that tungsten oxide has a lower density than tungsten and that different tungsten grains have different oxidation rates, are clearly visible. It illustrates that the CLSM is a powerful and efficient tool in providing oxidizing information of a large amount of grains at a time, thus opening up a possibility to determine the oxidation rates of many individual grains with various crystal orientations.

Parts of the presented results are already published and can be found in[66,67].

5.1 Experiment

The sample material for oxidation experiments is polycrstalline tungsten, which was prepared by recrystallizing the as-received tungsten purchased from Plansee SE (Austria) at 2000 K for 30 minutes at a pressure below 1×10^{-7} mbar (see section 3.1). Prior to the oxidation experiments, the polycrystalline tungsten was ground and electro-polished to obtain flat surfaces with a height difference among the grains of less than 50 nm[86]. Crystal orientation maps of the polished polycrystalline W samples were then obtained by EBSD with an electron scanning microscope (FEI, HELIOS Nanolab 600) for some predefined areas. The samples were oxidized in a thermobalance (Netzsch, Jupiter, STA449 F1) at different temperatures and for different time durations.
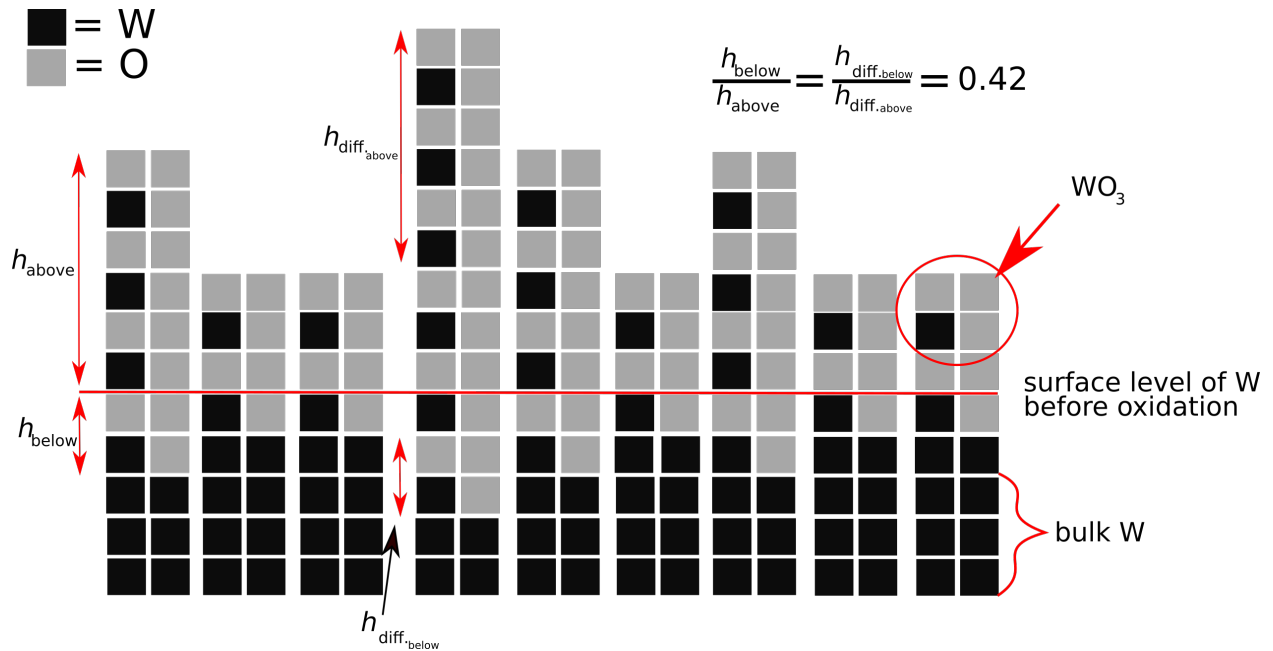
Figure 5.2: Schematic illustration of the oxidation process. Growth of oxide layer happens both above and below the original surface layer. Different thicknesses of the oxide layer are results of distinct oxidation rates.

After oxidation, the microstructure was characterized using: (i) CLSM to determine the 3D surface profile and (ii) preparation of cross-sections by FIB cutting to unveil the absolute thickness of the oxide layers. The surface profile data obtained from CLSM was ultimately converted to the thickness of the oxide layers. In the data conversion, the growth of oxides below the original surface level (as illustrated in figure 5.2) must be taken into account. The ratio of h_{above} to h_{below} gives a correction factor of 0.42 for the data converting[67]. With these three information the thickness of the oxide layer was determined with following equation

$$h_{\text{abs}} = h_{\text{abs}\langle 100 \rangle} - h_{\text{diff.above}} \cdot (1 + 0.42), \tag{5.1}$$

where $h_{abs\langle 100 \rangle}$ is the thickness of the oxide of the $\langle 100 \rangle$ crystal orientation obtained by FIB cuts and $h_{diff.above}$ is the difference measurement with the CLSM.

The Python tool used this equation during the data evaluation. For a detailed introduction to the correction factor, please refer to the bachelor thesis of Melissa Will[87].

5.2 Temperature dependent oxidation

The developed Python tool was applied to investigate crystal orientation dependent oxidation at different temperatures. To test the tool, the EBSD data reported in Ref.[67] and obtained with the old Oxford system (Oxford/HKl, Nordley II detector, Channel 5 acquisition software) was reevaluated. Note that the resolution of the IPF is reduced by a factor of 2 because of the low amount of data generated by the old EBSD system. To facilitate a direct comparison of oxidation experiments at different temperatures, the oxidation durations were adjusted by taking into account the oxidation rates reported in Ref.[88], so that a comparable thickness of oxide layers can be achieved for different oxidation conditions.
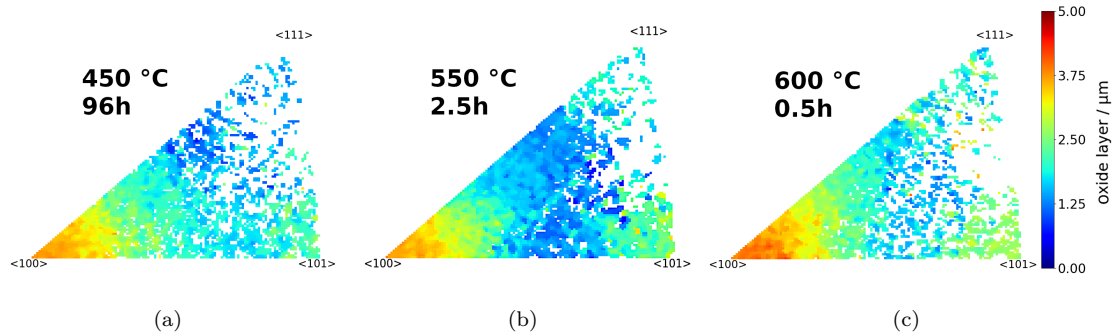
Figure 5.3: Oxidation layer thicknesses versus crystal orientations at various oxidizing conditions: (a) 450 °C for 96 h, (b) 550 °C for 2.5 h, (c) 600 °C for 0.5 h.

The resulting crystal orientation dependent oxidation at different temperatures is shown in figure 5.3. The absolute thickness of oxide layers was plotted against the crystal orientation. At the $\langle 100 \rangle$, $\langle 110 \rangle$ and $\langle 111 \rangle$ orientation, the oxide layer has a thickness of around 3.5 µm, 2.5 µm and 1.5 µm, respectively, which fits very well to the results of the manual evaluation reported in Ref.[67]. Within the error range, the oxidation experiments at 450 °C, 550 °C and 600 °C show a similar crystal orientation dependent behavior, i.e. the oxidation rates vary with surface crystal orientation in the same way at all 3 temperatures. The slight differences observed in figure 5.3 may be correlated with the influence of neighbor grains with different crystal orientations, which will be specially discussed in the next section.

5.3 Oxidation of textured samples at 600 °C

As shown in figure 5.3, the samples oxidized at 3 different conditions showed a not equal distribution of the data points. Probably, different textured samples could influence the oxidation rate in respect of the crystal orientation. For this reason some of the initial measurements were repeated with the new (faster) system. As shown in figure 5.4, 9 areas with a larger size were measured by the new EBSD detector. In comparison to the old detector used for figure 5.3, the new one increases the detected data amount by more than a factor of 10, thus promoting the chance to find crystal orientations which are less frequent in a textured sample. The faster detector allows to perform more experiments, i.e. to vary parameters, and to compare different textured sample directly to each other.

(a)	(b)
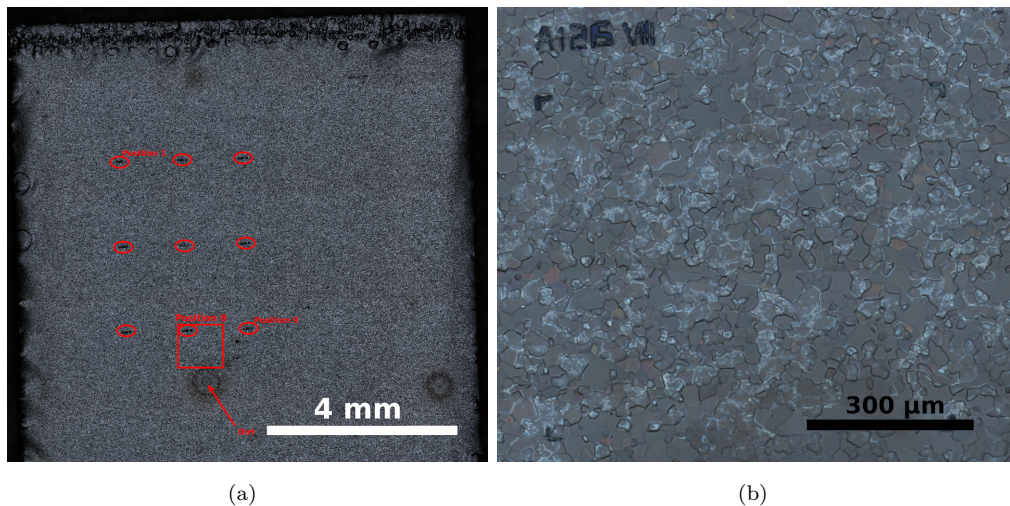
Figure 5.4: (a) Overview of an oxidized tungsten sample, showing the positions of areas where the crystal orientation is measured (highlighted by red ellipses). Surface contamination is indicated by the red arrow. This area was excluded during the evaluation. (b) Enlarged image showing the microstructure details in the red rectangular marked region of (a).

To examine whether the orientation of neighboring grains influences the oxidation via laterally increased oxygen diffusion, W samples with two different textures (A and B) were utilized[62]. While the $\langle 100 \rangle$ orientation was dominant in the sample with texture A, the sample with texture B was mainly composed of grains with $\langle 110 \rangle$ and $\langle 100 \rangle$ orientations. The two samples with the different textures were from the same processing batch and obtained from top and back side the same wrought material[62].
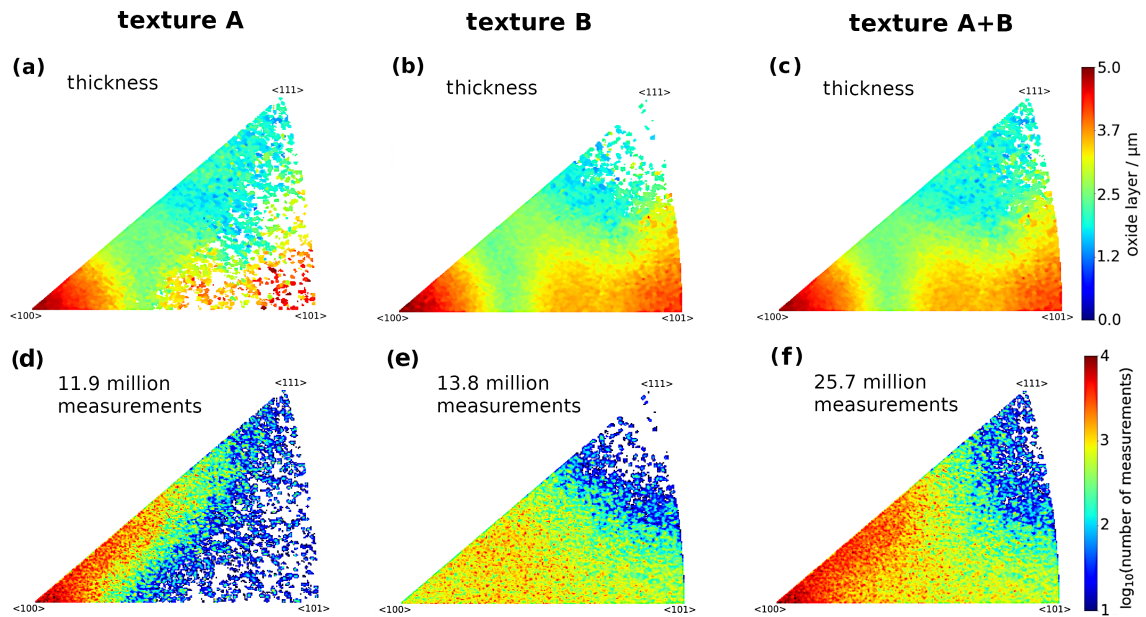
Figure 5.5: (a)-(c): oxidation layer thicknesses versus crystal orientations after applying all three types of filters. (d)-(f): measurement numbers versus crystal orientations. Tungsten samples with texture A and B were oxidized at 600 °C for 30 min. Data shown in (c) and (f) is a combined result of texture A and texture B.

As shown in Figure 5.5, over 10 million measurements were made for each sample with texture A or B. Both textures A and B exhibit similar oxidation dependencies on crystal orientations (see figure 5.5(a) and (b)). A second cross-check was made on the standard deviation. The standard deviation for textures A and B (not shown) was visualized separately and compared to that for all measurements (figure 4.5(b)). All three data sets show the same pattern of the standard deviation.

This agreement indicates that the automated methodology is robust and that the data of both samples can be combined to produce a more complete IPFz plot, as presented in figure 5.5(c). This figure includes above 25.7 million measuring points and shows the oxidation dependency for almost 'every' crystal orientation. The amount of measurements, actually the sum of texture A and B, is shown in figure 5.5(f). The thickness of the oxide layer shown in figure 5.5(c) is up to 5 µm, which is slightly larger than the thickness reported in figure 5.3(c).

41
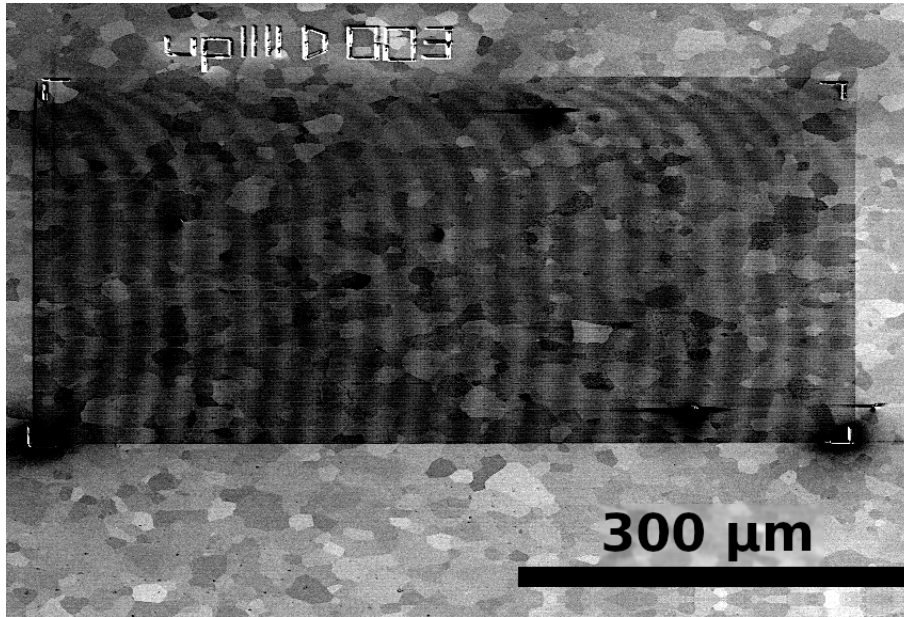
Figure 5.6: Secondary electron image showing the region where an EBSD measurement was performed. The L markers were made using FIB. Due to electron beam scanning induced carbon coating, the EBSD measured region appears to be darker than the rest regions.

The reason for thicker oxidation layer in the new oxidation experiment at 600 °C could be mainly caused by the used thermogravimetric analysis (TGA) system. The heating filament inside the TGA had hair cracks, which resulted in a different temperature field and a slower regulation of the temperature. The target temperature was overshot and oscillated for a few minutes during the oxidation experiments. Another explanation could be related to the carbon coating induced by two different EBSD detectors. When using the new EBSD detector, the exposure time of electron beam was reduced by more than a factor of 100, resulting in an obvious reduction of coated carbon layer on the sample surface. The residuum gas at a pressure of 10×10^{-6} mbar contains carbon, which is cracked by the electron beam. The carbon coating phenomenon, induced by the old EBSD detector, was strongly visible in the secondary electron image as shown in figure 5.6. The coated carbon layer is less than 1 nm thick, which is negligible in terms of its contribution to the measured thickness of oxidation layers. However, it cannot be excluded that such a thin carbon layer may have a non-negligible influence on the oxidation behavior of various grain orientations.

5.4 Different thickness of the oxide layer

Oxidation is a process which consists of several sub-processes like absorption and diffusion. Figure 5.7 is a mass gain plot of an oxidation experiment at 600 °C for 120 min. Different oxidation phases are marked with red fonts. Initially the W surface was electro-polished which cleaned and removed the tungsten oxides. After a short exposure, the first oxide layer is built up, the oxygen continues to diffuse through the first oxide layer and thus, W oxides are formed at the W oxide-W interface[89]. During this phase, the mass gain due to the diffusion of oxygen follows a parabolic behavior. With the influence of cracks, the parabolic mass gain behavior changes to a linear behavior. The formation of cracks relies on the Pilling-Bedworth ratio (PBR), which is defined in Ref.[90] as:

$$PBR = \frac{V_{oxide}}{V_{metal}} = \frac{M_{oxide} \cdot \rho_{metal}}{n \cdot M_{metal} \cdot \rho_{oxide}} \tag{5.2}$$

where V is the volume, M is the molecular mass, n is the number of atoms of metal per molecule of the oxide and ρ is the density. Cracks will be formed when PBR is bigger than 2. Note, the PBR is 3.39 for tungsten/tungsten oxides.
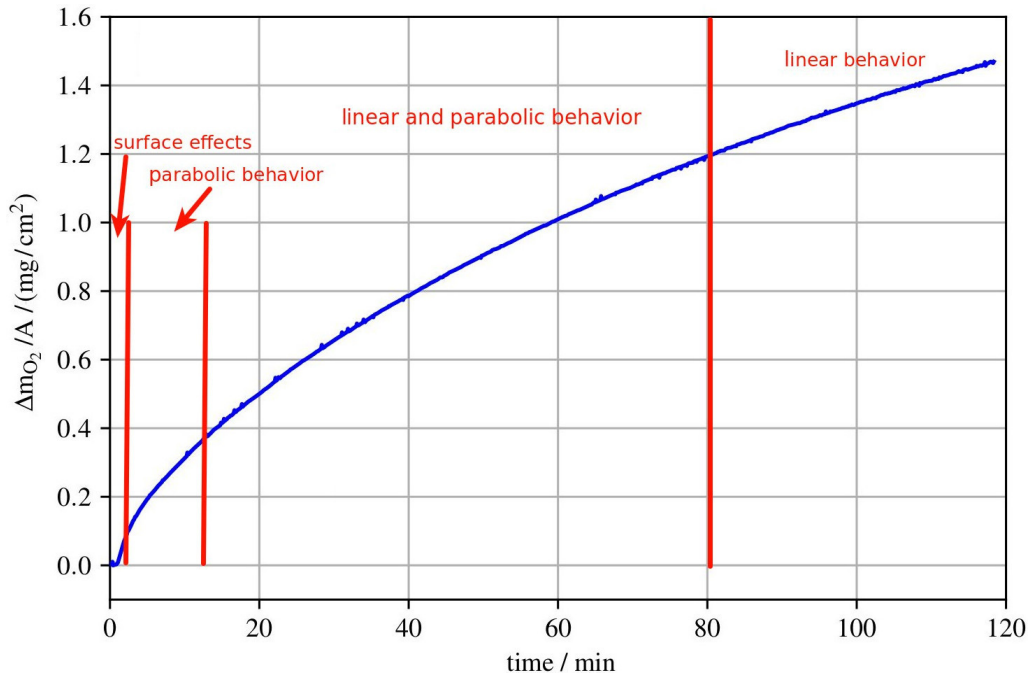
Figure 5.7: TGA measurement of an oxidizing experiment conducted on a tungsten sample at 600 °C for 120 min. Different oxidation stages are separated by red perpendicular lines and labeled.

The oxidation temperature was reduced to 400 °C for a controlled oxidation of an oxide layer of several nanometer thickness. To measure the height differences at

nanometer scale, the CLSM microscope is no longer suitable. An atomic force microscopy (AFM) is adequate for making nanoscale measurements, but it is very challenging to perform the measurement of a square millimeter area[91] [92].

After oxidation at $400\,°C$ for $10\,min$, it is observed that different grains have different gray scales in an intensity microscope image with a laser as a light source. Thin tungsten oxide layers are transparent, making it possible to generate different contrasts through interference[93]. However, the differences were slight and not suitable for an evaluation. Therefore, the oxidation experiment was repeated twice, i.e. at the end the sample was oxidized at $400\,°C$ for $30\,min$ in total, to achieve a condition that is suitable enough to analyze the oxide layer. The goal of the next step was to correlate different shades of gray to the thicknesses of the oxide layers. As shown in figure 5.8, the areas with a bright contrast in the CLSM image contain a higher concentration of oxygen than the areas with a dark contrast. Such a good correlation between gray tone and oxygen concentration is observed in an area with a size of over $1\,mm^2$. Since the modified CLSM and EDX analysis techniques do not give details on the thickness of oxidation layers, three cross-sections were prepared using FIB for a direct thickness measurement of the oxide layer.
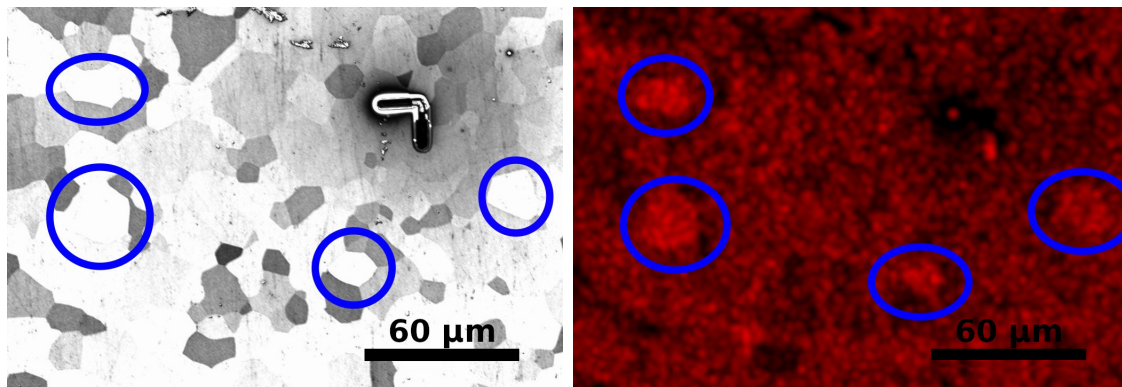
Figure 5.8: Oxygen concentration information revealed by (a) a CLSM image and (b) an EDX analysis image in the same surface region. The bright contrast in (a) and strong intensity of red color in (b) indicate a high tungsten oxide level. As indicated by the blue circles, some tungsten grains are clearly visible in both (a) and (b).

The areas for the cross-section were selected to contain a bright and a dark gray tone in the CLSM image to analyze the differences between the gray tones. Figure 5.9 shows a representative image of a cross-section. A tungsten oxide layer with a thickness of between $30\,nm$ to $45\,nm$ was found on the surface. In figure 5.9, the oxide layer on the left hand side was a tungsten grain with the bright gray tone in the CLSM image. This tungsten grain had a thicker oxide layer than the grain on the right hand side, where the tungsten grain had a dark gray tone in the CLSM. Observations of the other two cross-sections further demonstrated such a correlation of gray scales with a similar thicknesses of oxide layers.

44
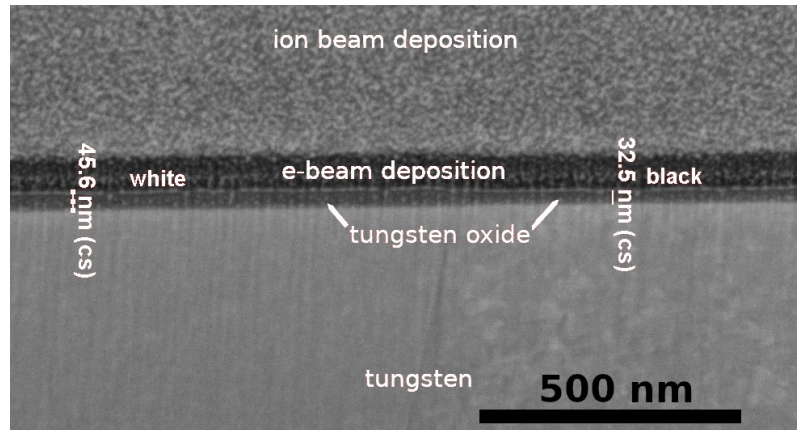
Figure 5.9: Secondary electron image of the cross-section of a tungsten sample oxidized at 400 °C for 30 min. In the corresponding CLSM image, the tungsten grain on the left side appears with white while the right side grain is black, corresponding to an oxide layer on the left tungsten grain, which is thicker than that on the right tungsten grain. To protect the oxidation layer for precise measurements, two deposition layers were made first by electron beam and second by ion beam.

The gray scales of the oxidized tungsten sample were evaluated versus the crystal orientation and compared to oxide layers with different thicknesses.

Figure 5.10 (a) shows the shades of gray of various crystal orientations in a 8 bit scale, which correspond to the starting phase of the oxidation and has an oxide layer thickness between 30 nm and 50 nm. To unveil the crystal orientation dependency of oxide layer thicknesses, oxidation of polycrystalline tungsten was performed at 600 °C for different time duration (including 10 min and 60 min), as shown in figure 5.10.
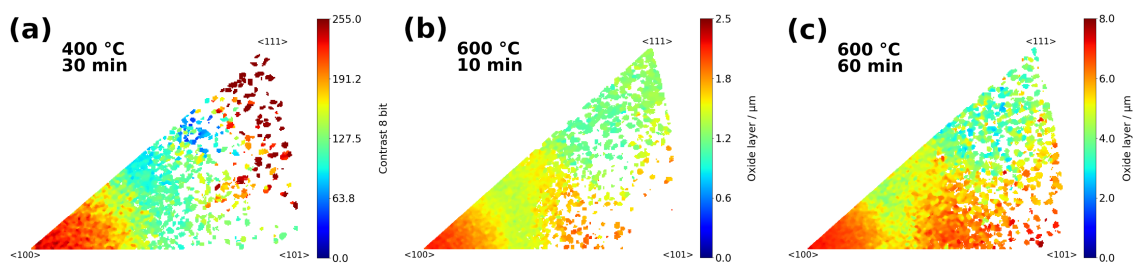
Figure 5.10: Crystal orientation dependent oxidation behavior of tungsten samples at various experimental conditions: (a) shades of gray versus crystal orientations for a tungsten sample oxidized at 400 °C for 30 min. The maximum and minimum oxide thicknesses are ∼47 nm corresponding to white (0) and ∼32 nm corresponding to black (255). Note that some crystal orientations were not found on the sample, which result in white areas. Therefore, the gray scale data of the image was visualized in a color scale; (b) oxide thicknesses versus crystal orientations for a tungsten sample oxidized at 600 °C for 10 min; (c) oxide thicknesses versus crystal orientations for a tungsten sample oxidized at 600 °C for 60 min (Figure 5.5(c) shows a tungsten sample oxidized at 600 °C for 30 min).

45

Oxidation at 600 °C for 30 min was already shown in figure 5.5, acting as a comparison to figure 5.10. Whereas the experiments with µm W-oxide layers showed the same distribution of oxidation rates versus crystal orientation (see figures 5.5(c) and 5.10 (b),(c)) the crystal-dependent oxidation looks quite different in the initial phase (nm thick oxide layer).

For a nm thick oxide layer, the ⟨111⟩ crystal orientation had the highest oxidation rate, and for an oxide layer several µm thick, the ⟨111⟩ crystal orientation had the lowest oxidation rate. It is unlikely that this is due to different oxidation temperatures, because for a temperature range between 450 °C to 600 °C the distribution of oxidation rates to crystal orientation was the same, which can be found in section 5.2, figure 5.3.

Surface effects are dominant during the initial oxidation process forming thin oxidation layers. As shown in figure 5.11, the ⟨111⟩ orientation of bcc tungsten has the lowest atomic surface density and the ⟨111⟩ orientation exhibited the highest oxidation rate for a nm thin oxide layer. The atomic surface density of the ⟨110⟩ orientation is higher than that of the ⟨100⟩ orientation. Obviously, the surface density of the crystal orientation correlates very well to the oxidation rates, which was discussed in Ref. [85].

The oxidation process forming thick oxide layers should be different from the process forming thin oxide layers. At first, oxidation starts rapidly at the ⟨111⟩ crystal

(a) A crystal lattice in ⟨100⟩ direction. The distance between atoms in the ⟨100⟩ direction is one unit cell length.

(b) A crystal lattice in ⟨110⟩ direction. The atoms are close together in the first atom layer. The atomic surface density is the highest compared to the other low index surfaces.

(c) A crystal lattice in ⟨111⟩ direction. The atoms are far away from each other in the first atom layer. The atomic surface density is the lowest compared to the other low index surfaces.

Figure 5.11: Comparison of the low index surface orientation [94].

orientation through surface effects. The $\langle 111 \rangle$ crystal orientation showed the fastest oxidation rate compared to the other crystal orientations. After the formation of the oxide layer of dozens of nm, diffusion of oxygen through the oxide layer becomes the dominant process. The $\langle 111 \rangle$ crystal orientation showed the lowest oxidation rate compared to the other crystal orientations in experiments with a µm thick oxide layer. Such a change with the thickness of the oxidation layer in the crystal orientation dependent oxidation behavior can also be seen in Ref.[95].

5.5 Discussion of crystal-dependent oxidation

The investigations show that the crystal orientation dependent oxidation behavior is insusceptible to the temperatures in the range between 450 °C to 600 °C, the crystal textures, and the neighboring grains. On the contrary, the thickness of oxide layers has an impact on the crystal orientation dependent oxidation behavior. This is due to the fact that different mechanisms control the oxidation process when forming an oxide layer with different thicknesses. For the formation of thin oxide layers (nanometer-scaled), surface effects play a dominant role in the oxidation process. As a result, tungsten grains with $\langle 111 \rangle$ direction show the highest oxidation rate. When the oxide layers reach up to µm, diffusion of oxygen through the oxide layers is the dominant process and thus tungsten grains with $\langle 111 \rangle$ direction show the lowest oxidation rate. For the surface effects, the sample preparation by electropolishing might be crystal orientation dependent.

Since electropolishing is an etching process, these grains could have an atomic surface roughness which influences the oxidation at the beginning. In general, roughness increases the surface area and therefore the oxidation rate is influenced[96].

In the investigations by Fluton G. and Luneve A.[95] the samples were polished with an 1 µm diamond suspension, and nevertheless the same temporal development of the oxidation rate for the $\langle 111 \rangle$ crystal orientation as in this work was found. Since the study in this work and the investigation by[95] used different polishing techniques, it is supposed that it is not a polishing effect but an effect of the oxide layer.
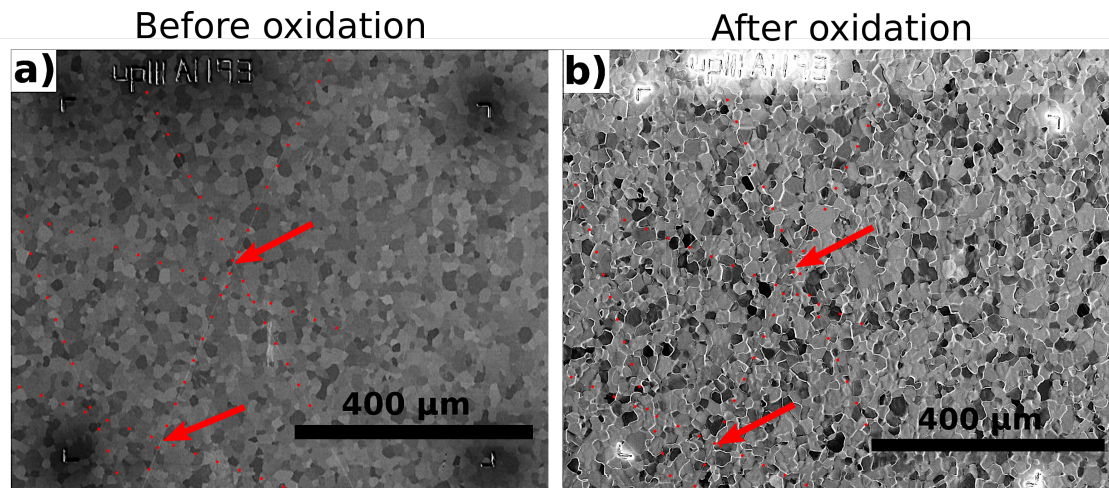
Figure 5.12: Secondary electron images of a recrystallized tungsten sample at the same region: (a) prior to oxidation scanned with an electron beam, (b) after oxidation at 600 °C for 30 min scanned with a Ga ion beam. In (b), the different shades of gray represent differences in the oxides, e.g. could be different crystal orientations. The scratches indicated by red arrows are hardly visible after the oxidation process, but still present at the surface.

Figure 5.12 supports that the tungsten oxide is different on different grains, because figure 5.12 (b) shows that a Ga ion induced secondary electron (SE) picture with different shades of gray. In addition, the surface structure from the initial tungsten surface was visible in a several µm thick oxide layer. Figure 5.12(a) shows a recrystallized tungsten sample with little scratches after polishing. Figure 5.12(b) shows an oxidized tungsten sample of the same area and the scratches are slightly visible.

The surface information of the W surface was transferred to the oxide layer which could influence the oxidation behavior. This means that roughness through the grinding or deformation of the surface influences the oxidation continuously and it could be assumed that it is not a temporal phenomenon at the starting phase of the oxidation.

On a µm thick oxide layer, it is possible that the crystal lattice information of W is transferred to W oxides, which would have an influence on the diffusion of oxygen. The different diffusion rates of oxygen could make a change of the oxidation rate in the $\langle 111 \rangle$ orientation.

There are several hints that the grain dependent oxidation in the current studies is influenced by the diffusion of oxygen through crystalline W oxide. First, the temporal weight increase of the oxidation indicates a parabolic behavior. Second, Kikuchi patterns on the W oxide were observed with the EBSD system, but they were ambiguous. Two Kikuchi patterns are shown in figure 5.13, but an evaluation of these patterns was not possible, i.e., no crystallographical oxide phase and orientation could be assigned. At least they show a crystalline structure, which could influence the diffusion.

(a)   (b)
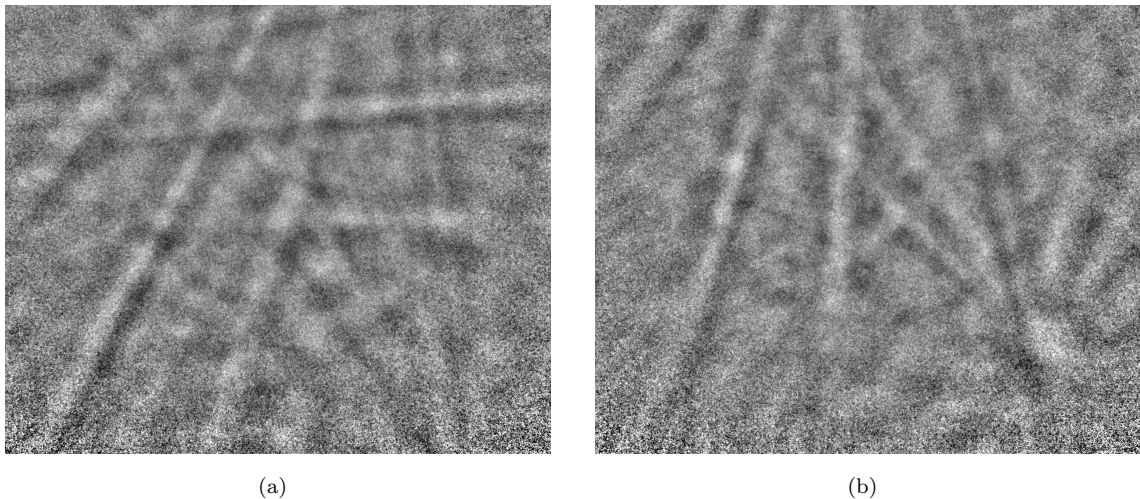
Figure 5.13: Two Kikuchi pattern examples of a several micrometer thick oxide layer. The Kikuchi patterns are not clear and therefore, it was not possible to evaluate the crystal lattice. But the existance of Kikuchi lines shows that the oxide layer has an ordered atomic arrangement.

Third, a Ga ion induced SE picture is dominated by a crystal orientation contrast (figure 5.12(b)). An interpretation of these contrast data is speculative, because the W oxide crystallographical phase could be different at room temperature compared to the phase at the temperature of the oxidation. The most stable W oxide is WO_3, which has an orthorhombic crystal lattice at 600 °C. But at room temperature it could be reduced to, e.g. a monoclinic crystal lattice[17]. Since the Ga-ion induced secondary electron picture (figure 5.12(b)) is dominated by the crystal lattice contrast, it indicates that W oxides with different crystal orientations exist.

6 Sputtering of tungsten

Many researchers have found that the sputtering behavior of crystal materials are grain orientation dependent [8,9,10,11,12,13]. Figure 6.1 shows a polycrystalline tungsten sample sputtered with a 30 keV Ga ion beam. The different shades of gray show W grains and indicate different crystal orientations. Height differences between the W grains, which resulted from different sputter yields, are clearly visible too.
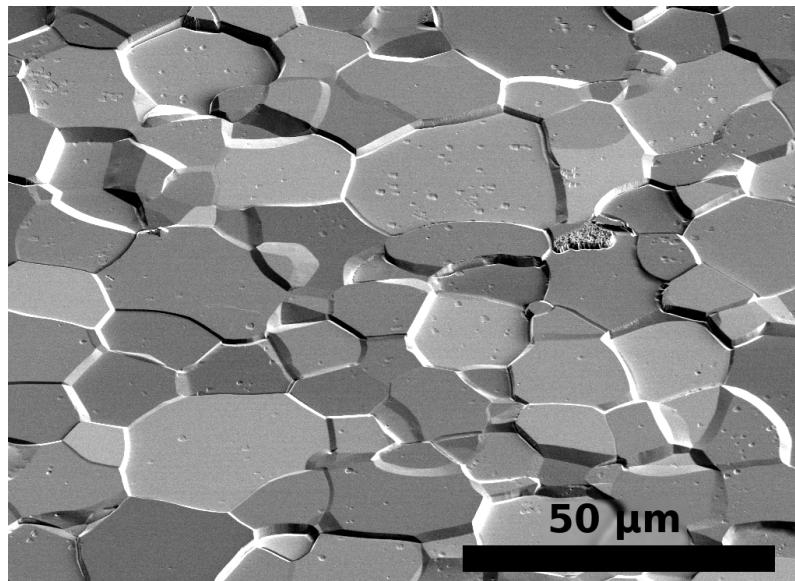
Figure 6.1: Secondary electron image of a polycrystalline tungsten sputtered with a 30 keV Ga ion beam. The image was taken under a tilt angle of 52°. Different tungsten grains can be well distinguished from the brightness level.

The impact of crystal lattices, especially the low index surfaces, on the sputter yields of crystalline materials was often investigated. However, a systematic study evaluating sputter yields over many different crystal orientations was missing. A comprehensive knowledge of crystal-dependent sputtering enables to benchmark simulations to experimental data, to predict the sputter behavior of strongly textured material, to study the impact of channeling directions and to predict roughening of polycrystalline samples induced by ion polishing.

Sputter simulation programs, e.g. static/dynamic transport of ions in matter with the calculation mode serial or parallel (SDTrimSP), assume an amorphous target. That means, the crystal lattice structure is completely ignored [39,97]. Often, the experimental sputter yields of a polycrystalline sample having a preferred crystal orientation at the sample surface [86,98], are compared to simulations assuming an amorphous target [99].

Previous studies focused on investigating the sputter yields of single crystals and

generating data from some specific crystal orientations[9,10,11,12]. The developed tool is suitable for investigating sputter yields in every crystal orientation. In this work, tens of thousands of grains with various orientations were sputtered. The sputter yields were evaluated to create an erosion map in an inverse pole figure (IPF). Subsequently, the measured sputter yields were compared to the values generated from three different kinds of simulations (SDTrimSP[100], molecular dynamic (MD) and binary collision approximation (BCA)). Among the three simulations, the MD simulation was performed by Kai Nordlund, from the University of Helsinki, Finland, and the BCA simulation was conducted by Gerhard Hobler, from TU Wien, Austria. Some details of the MD and BCA simulations can be found in[49].

In this section, the details of the sputter experiments are introduced. Since a Ga ion beam at 30 keV provides the highest sputter yield, the crystal-dependent sputtering experiments were mostly performed with this energy. Therefore, the influence of fluence or flux density was investigated at this energy. In terms of the crystal-dependent sputtering with different Ga ion energies, a detailed comparison between experimental results and simulations was made. Since the impact angle of the ions has an impact on the sputter yield, different ion impact angles were investigated too (shown in section 6.3). There it was noticed that the sensitivity of the experiment to the ion impact angle was around 1°. This was important for D sputtering of tungsten and HPM1850 at 2 keV, because the accuracy of the impact angle in the D sputter device second ion experiment for sputtering and TDS analysis (SIESTA) was around 5°.

After recognizing that the experiments were very sensitive to the impact angle of the ions, an algorithm was written to detect the impact angle and thereby to evaluate the D sputter experiments and reevaluate the 30 keV Ga sputtering data. Descriptions and explanations on this algorithm can be found in section 4.4 and in the angle-dependent sputtering section 6.3.

In addition to sputtering, Ga implantation was investigated versus the crystal orientations as well as the secondary electron emissions induced by a Ga ion beam. This all together gives a detailed picture of the influence of the crystal orientation on the interaction between a textured material and the impinging ion beam.

6.1 Experiment

The investigated samples were hot rolled polycrystalline tungsten samples with a purity of 99.97 wt% (Plansee SE, Austria). To create grains with proper sizes and little internal stress and strain, the material was first recrystallized at 2000 K for 30 minutes under vacuum pressure below 10^{-7} mbar, and then ground up to P4000 and electro-olished (for details, please see section 3). The sample preparation was the same as for the oxidation experiments. Figure 6.2 shows a sputtered tungsten sample with a 30 keV Ga ion beam. All sputter experiments were located within a frame where the zero level was determined. The height differences along the frame were less than 150 nm. Since the erosion depths measured from grains with the same crystal orientation of different locations are comparable (i.e. around 1 µm), we conclude that the height measuring error has a negligible influence on the final results. In the final version of the Python tool, difference microscopy was implemented which could reduce the error significantly in some experiments. Since applying difference microscopy needed data sets before the erosion experiments, only the data sets were reevaluated where the data sets existed. This was the case for 2 keV deuterium sputtering on the High Performance Materials 1850 (HPM1850), because the sample was rough after polishing. The crystal orientations and their respective heights were merged together by using the python tool described in section 4.2.
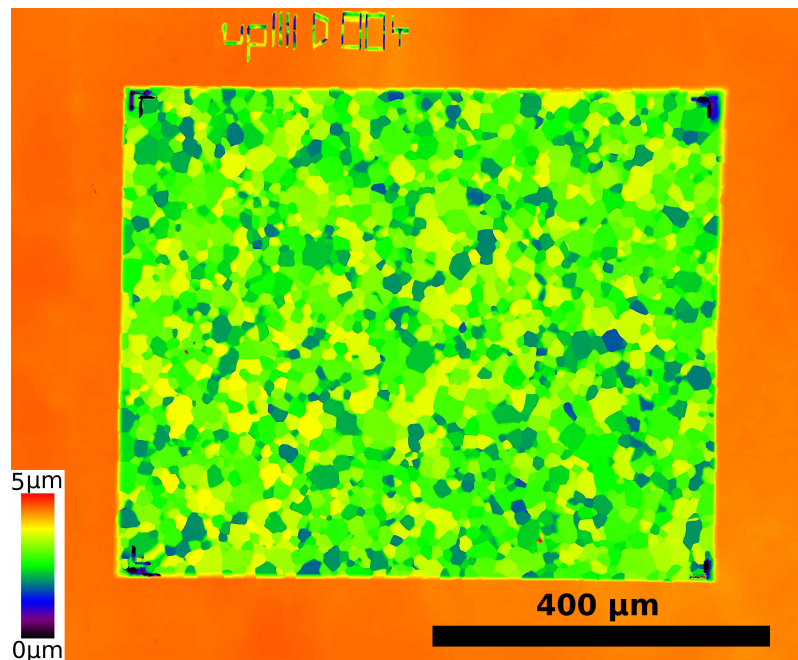
Figure 6.2: Height profile map of a sputtered region on a polycrystalline tungsten sample. The sputtering was performed by a 30 keV Ga ion beam. The frame outside the sputtered area has a height difference of less than 150 nm. The height of the frame is set as the zero level for the erosion data in figure 6.3.

The experiments were mainly performed with the standard settings of the FIB-SEM for sputtering of small areas. For large areas, e.g. 600 µm x 600 µm, the default value of the 'pitch', i.e. defocusing the ion beam, had to be changed from 127 nm to 500 nm, because two ion beam spots should have an overlap between each scan step. The time for sputter experiments at 30 keV was about 13 hours. Usually, the sputter experiments were conducted over night and the corresponding sample evaluations were performed during the day. For different energies, the sputter time was adjusted according to the erosion depths and area sizes. In general, the sputter depths were fixed to 1 µm. The markers made by FIB (e.g. marker 'D004' in figure 6.2) were used to find the same area in different microscopy systems.

In figure 6.3, the erosion depth was plotted against the crystal orientation for a 30 keV Ga ion beam on tungsten. To compare the experimental results to the simulations, the sputter yield had to be calculated from the erosion depth by using equation 2.10 (for the corresponding result, please see figure 6.12(a)).
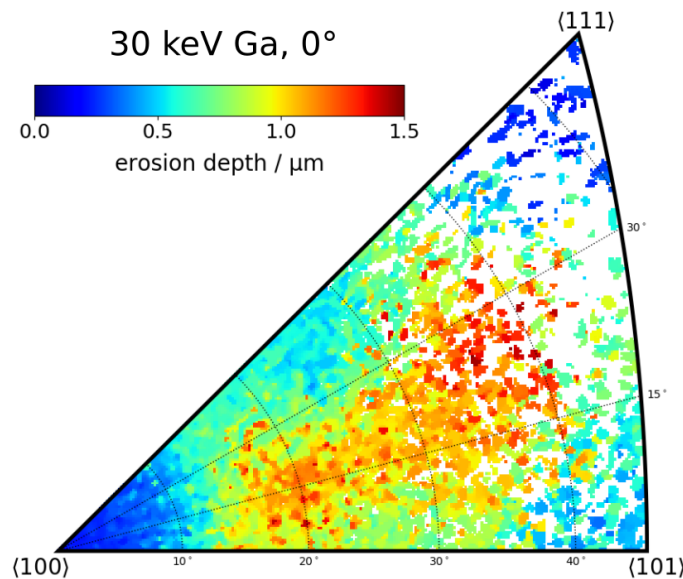
Figure 6.3: Erosion depths versus the crystal orientations in an IPF. A 30 keV Ga ion beam was used to sputter polycrystalline tungsten samples. Statistics for the experimental evaluations are shown in figure A.4 in the appendix.

The sputter experiments with D ions were performed in the linear plasma device named "SIESTA". The sputter experiments were performed at a D ion energy of 2 keV and took about 30 hours to reach an erosion depth of 500 nm. Details of the machine, e.g. profile of the beam spot, can be found in [101].

6.1.1 Influence of fluence on the sputter yield

From literature it is known that the sputter yield can depend on the fluence[102]. During the sputter experiment, Ga ions were implanted into the crystal structure and after a certain fluence they could influence the sputter yield. Therefore, the settings of the FIB, like the energy of 30 keV, current of around 17 nA and the scan size of around $700 \times 600\,\mu m^2$, were fixed. Only the sputter time was adjusted between 6 h to 48 h for different fluences. In this section, line diagrams present the sputter yields allowing a more detailed comparison of the data. This means that the sputter yields are visualized in one rotation axis from the $\langle 100 \rangle$ to the $\langle 111 \rangle$ crystal orientation.
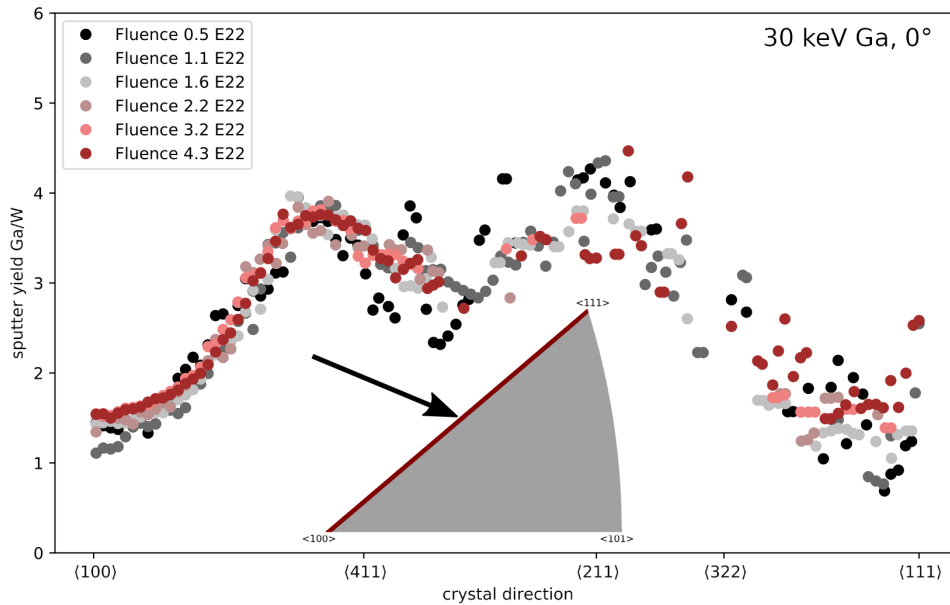
Figure 6.4: Sputtering of a polycrystalline tungsten by a 30 keV Ga ion beam under an incident direction parallel to the surface normal: influence of ion fluences on the sputter yields of tungsten grains with various crystal orientations. Note that only the crystal orientations along the straight line from $\langle 100 \rangle$ to $\langle 111 \rangle$ of the inserted IPF figure are displayed.

The comparison is shown in figure 6.4. The experiments show a high reproducibility and that a different fluence does not have an impact on the experiment or evaluation. The data spread is bigger between the $\langle 211 \rangle$ and $\langle 111 \rangle$ crystal orientation. As shown in figure A.4 in the appendix for the fluence $1.12 \times 10^{22}\,\frac{Ga}{m^2}$, the amount of measurements for these orientations are orders of magnitudes lower compared to the $\langle 100 \rangle$ crystal orientation, because of the textured sample. This means that one sputter yield evaluation results from one or a few grains between the $\langle 211 \rangle$ and $\langle 111 \rangle$ crystal orientation. The sputter yield from one grain is not reliable, because this

grain is not specific characterized, e.g. the grain size is unknown and the erosion could be influenced by a second grain.

As a second check, the experiments were repeated for an ion impact angle of 60°. Under different impact angles the fluence was different, because of geometrical aspects of the experiments, respectively the scan size of the FIB was not adjusted. Another reason is that the damage level next to the surface could be changed due to the ion impact angle. Also, by tilting the sample to 60° a lot of grains will have the ⟨111⟩ orientation to the directions of the impacting ions and therefore a lot of measurements will be evaluated for this crystal orientation, which are missing in figure 6.4.
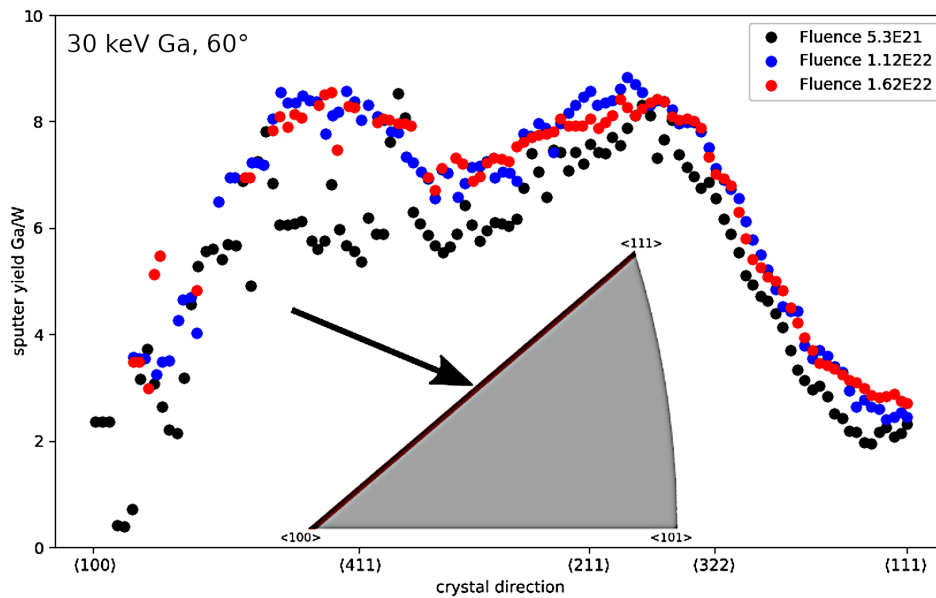
Figure 6.5: Sputtering of a polycrystalline tungsten by a 30 keV Ga ion beam under an incident angle of 60° with respect to the surface normal: influence of ion fluence on the sputter yields of tungsten grains with various crystal orientations. Note that only the crystal orientations along the straight line from ⟨100⟩ to ⟨111⟩ of the insert IPF figure are displayed.

The result of the second comparison is shown in figure 6.5. For 60°, the experiments show a high reproducibility and that the lowest fluence showed a reduced sputter yield. Four sputter experiments with the fluence of $1.12 \times 10^{22} \frac{Ga}{m^2}$ showed an average erosion of around 1.4 µm and four sputter experiments with the fluence of $5.3 \times 10^{21} \frac{Ga}{m^2}$ showed an average erosion of 0.6 µm. This is around 10 % (100 nm) lower as expected, but the standard deviation (SD) is around 200 nm as shown in the appendix in figure A.2 and A.3. Figure 6.6 shows the complete data sets as an IPF of the two fluences. There are only slight differences observed. For a solid statement,

experiments with a higher accuracy are needed, e.g. difference microscopy without the stitching function of the CLSM.

In figure 6.5, the spread of the data between the ⟨100⟩ and ⟨411⟩ crystal orientation, could be due to the low amount of measurements, which is over a factor of 10 lower than for the ⟨111⟩ crystal orientation. In contrast to sputtering perpendicular, the crystal surface orientations and the crystal orientations facing to the ion beam were different. This additional dimension is ignored during the evaluation and could lead to a higher spread of the data.
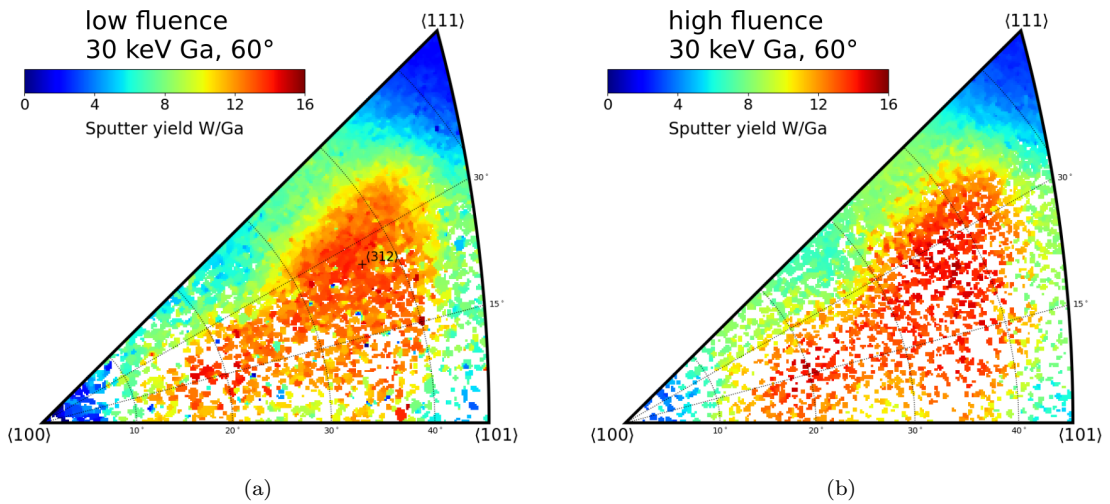
Figure 6.6: Sputter yields versus crystal orientations for tungsten sputtered with a 30 keV Ga ion beam under an incident angle of 60° with respect to the surface normal. Two different fluences are shown, where (a) was sputtered with a fluence of 5.3×10^{21} Ga/m² and (b) was sputtered with a fluence of 1.21×10^{22} Ga/m².

6.1.2 Influence of flux density on the sputter yield

From literature it is known that the sputter yield can depend on the flux density[103], because the target material can chemical react with the residuum gas. A pure physical sputter process should not be effected by the flux density. For a FIB, the flux, which is defined by the current of the ion beam, was the same for all experiments, but the scan size was different. The FIB scans over a defined area and if the area is bigger, the ion beam will need a longer time for scanning the whole area. The expression "flux density" is used as the average flux over a defined area.

Most of the sputter experiments were performed with a 30 keV Ga ion beam and the scan size of the FIB was eventually adjusted to the workflow of the laboratory and experimental conditions. Therefore, a possible effect due to this variation in flux density was investigated.

For all sputter experiments in this section, a polycrystalline recrystallized tungsten target was used and the current of the FIB was not changed, but the scan size and the resulting sputtered area were different. For this purpose, 4 different scan sizes were used which resulted in 4 different flux densities. The fluence was the same for all areas and therefore the time was adjusted. The parameters are summarized in table 2.

Table 2: Sputter experiments using a 30 keV Ga ion beam under an incident angle parallel to the surface normal. Four different ion flux densities were studied with a fluence of $1.12 \times 10^{22} \frac{\text{Ga}}{\text{m}^2}$. The ion beam current for all experiments was around 19 nA.

Flux	Area / μm^2	Sputter time / hh:mm	Flux density / $\frac{Ga}{m^2 \cdot s}$
1	975 x 845	22:46	1.37×10^{17}
2	700 x 600	11:36	2.87×10^{17}
3	700 x 300	05:48	5.74×10^{17}
4	350 x 300	02:54	11.48×10^{17}

An IPF was generated for all flux densities, which looks similar to figure 6.3. For a comparison, a line scan was performed from the $\langle 100 \rangle$ to the $\langle 111 \rangle$ crystal-orientation. The line scan is shown in figure 6.7. The experiments show a high reproducibility and that a different flux density has no impact on the experiment or evaluation.
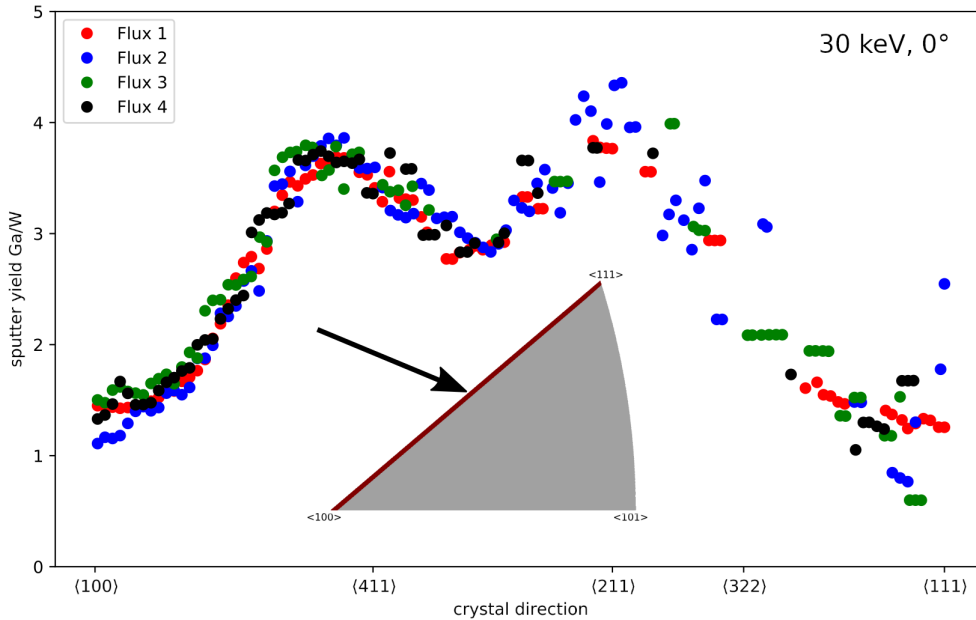
Figure 6.7: Sputtering of a polycrystalline tungsten by a 30 keV Ga ion beam under an incident direction parallel to the surface normal: influence of ion flux densities on the sputter yields of tungsten grains with various crystal orientations. Note that only the crystal orientations along the straight line from $\langle 100 \rangle$ to $\langle 111 \rangle$ of the inserted IPF figure are displayed.

The experiments were repeated under an impact angle of 60° to the surface normal for the same reasons as for the fluence dependency. The used sputter scan size and time for the sputter experiments are shown in table 3. The fluence is the same for each experiment.

Table 3: Sputter experiments using a 30 keV Ga ion beam under an incident angle of 60° with respect to the surface normal. Three different ion flux densities were studied with a fluence of $5.3 \times 10^{21} \frac{\text{Ga}}{\text{m}^2}$. The ion beam current for all experiments was around 19 nA.

Flux	Area / μm^2	Sputter time / hh:mm	Flux density $\frac{Ga}{m^2 \cdot s}$
1	850 x 1400	15:54	0.93×10^{17}
2	700 x 600	05:18	2.78×10^{17}
3	350 x 300	01:27	10.15×10^{17}

For all flux densities, an IPF was generated and a diagram presents the sputter yields around one rotation axis from the $\langle 100 \rangle$ to the $\langle 111 \rangle$ crystal-orientation. Figure 6.8 shows similar sputter behavior for all flux densities and the average erosion depth was around 600 nm in all experiments. The spread of the data between the $\langle 100 \rangle$ and $\langle 311 \rangle$ crystal orientation could be due to the low amount of measurements, which is over a factor of 10 lower than for the $\langle 111 \rangle$ crystal orientation.
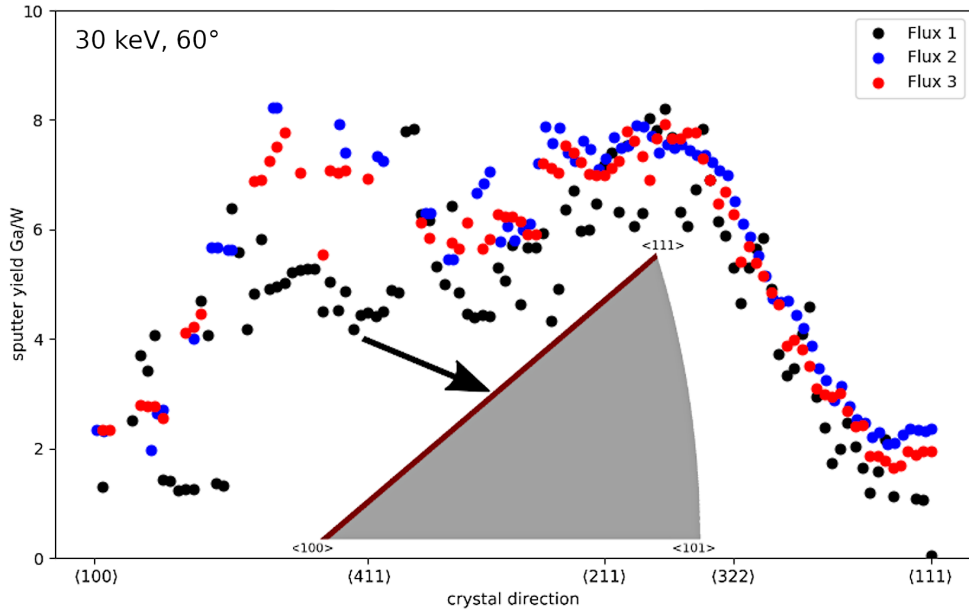
Figure 6.8: Sputtering of a polycrystalline tungsten by a 30 keV Ga ion beam under an incident angle of 60° with respect to the surface normal: influence of ion flux densities on the sputter yields of tungsten grains with various crystal orientations. Note that only the crystal orientations along the straight line from $\langle 100 \rangle$ to $\langle 111 \rangle$ of the insert IPF figure are displayed.

59

For a 2 keV gallium ion beam the erosion depth was unexpected low. Due to the simulation, the experiment was designed to erode 1 µm into tungsten grains and the experimental erosion depth was at the end around 0.3 µm.
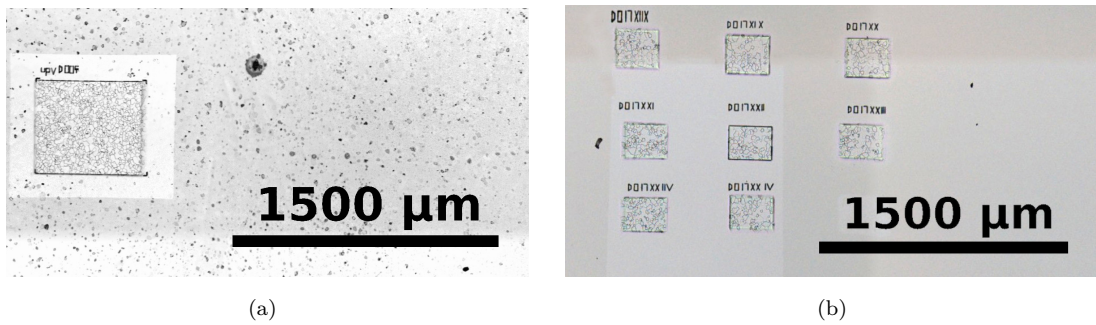
Figure 6.9: CLSM images showing 2 keV Ga ion beam sputtered tungsten surface areas: (a) 1 area with a size of $900 \times 750 \, \mu m^2$ was sputtered. (b) 20 areas with a comparable size of $250 \times 200 \, \mu m^2$ were sputtered and 8 of them are shown here. Each area in (a) and (b) was sputtered with the identical ion fluence.

Therefore, 2 keV Ga ions were checked regarding the flux density. The experiments were repeated with a different flux density. The first experiment with the low flux density, an area of around $1 \, mm^2$ was sputtered, which is shown in figure 6.9(a). The area size was similar to the area when using the 30 keV Ga ion beam. The height data of this experiment was evaluated and the erosion depths were plotted in an IPF, shown in figure 6.10(a). The average sputter yield of this experiment was 0.51 W/Ga whereas the SDTrimSP simulation provided a sputter yield of 1.63 W/Ga, being a factor of 3 different.

A reason of the lower erosion rate could be the influence of the residuum gas in the SEM chamber, e.g. oxidation of the target or deposition of non-volatile impurities. To avoid these effects, the sputtered area sizes were reduced by a factor of 14, as shown in figure 6.9(b), and therefore, the sputter time was shorter by a factor of 14, due to the higher flux density. The fluences were the same of each sputtered area. The erosion depth versus the crystal orientation is shown in figure 6.10(b). The average sputter yield of 1.57 W/Ga was within the error range of the SDTrimSP simulation and in average a factor of 3 higher than the sputter yield data extracted for the larger area. Although it was not investigated at which flux density the sputter yield is constant, it is assumed that the effect of residuum gas is negligible at these flux densities and does not effect the experiment strongly for sputtering an area.
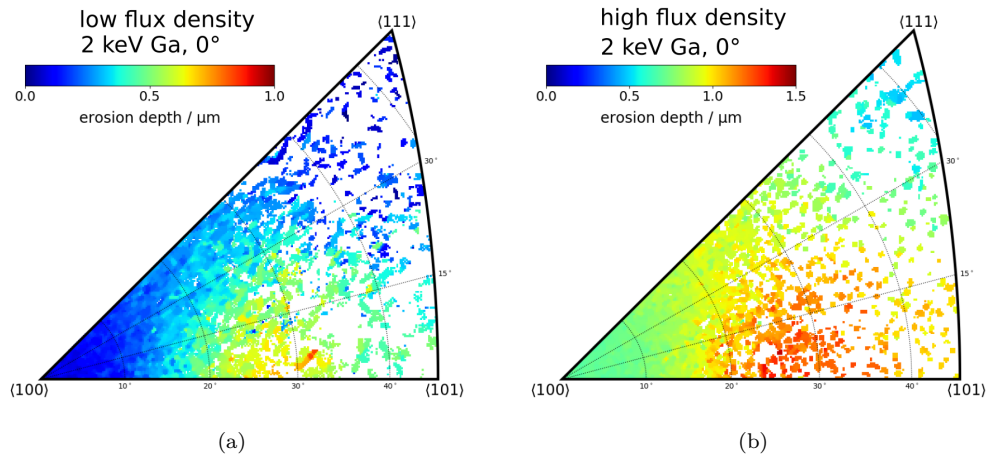
Figure 6.10: Erosion depth versus crystal orientations for tungsten sputtered with a $2\,\text{keV}$ Ga ion beam. (a) tungsten sputtered with a high flux density (the sputtered area in (a) was $250 \times 200\,\text{µm}^2$). (b) tungsten sputtered with a low flux density (the sputtered area in (b) was $900 \times 750\,\text{µm}^2$). Each area in (a) and (b) was sputtered with an identical ion fluence, which should result in the same erosion depth. Note that the color scales are not the same and that there is a significant difference in the erosion depth.

In general the flux density could influence the results for energies lower than $30\,\text{keV}$ Ga ions. In the next section, the energy-dependent sputter yields will be shown. The experimental sputter yields were in good agreement with simulations and due to the good agreement, it is unlikely that the flux density had a strong effect.

6.2 Energy-dependent sputter experiments with gallium ions

The sputter experiments with Ga ions were performed for four energies, 2 keV, 5 keV, 8 keV, and 30 keV. For an overview of the sputter yields, SDTrimSP simulations were performed in a larger energy range from 50 eV to 5 MeV for Ga ions, and from 50 eV to 500 keV for D ions. The program SDTrimSP assumes an amorphous tungsten target[100], while in the sputter experiments a polycrystalline tungsten sample was used. SDTrimSP simulations fit to the average crystal-dependent sputter yields and they are often used as a comparison for experimental crystalline data[99,104,105]. The energy-dependent sputter yields generated from the SDTrimSP simulations are shown in figure 6.11. The input file showing the SDTrimSP simulation details is attached to section A.2.1. As indicated by the black dotted lines, the sputter experiments with Ga ions were conducted within the energy range from 2 keV to 30 keV. Here it is worth to mention that the sputter yield with Ga ions reaches nearly its maximum at 30 keV. Thus, it is suitable to perform parameter investigations (e.g. angle-dependent sputtering) at this energy. At energies higher than 100 keV, the sputter yield decreases, as the energy is deposited deeper into the specimen.
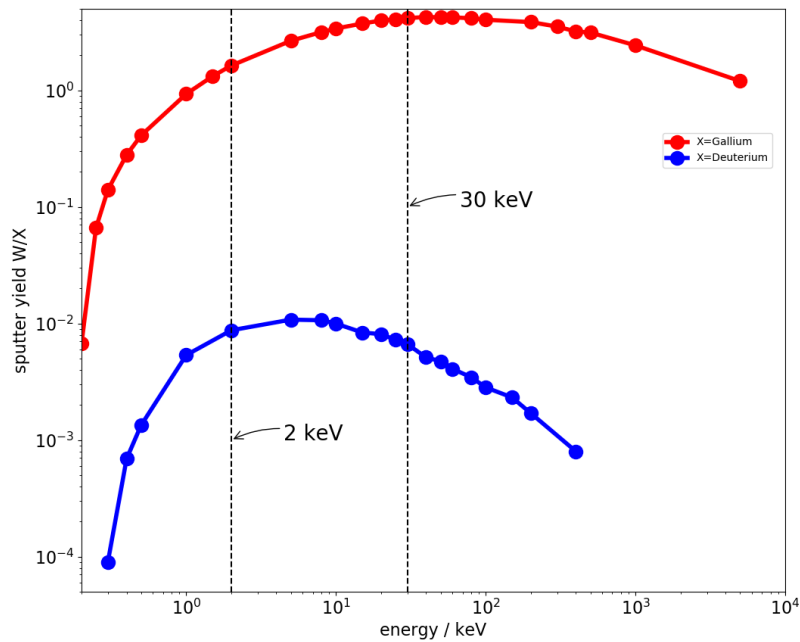
Figure 6.11: SDTrimSP simulations of the sputter yields of the target W by deuterium and gallium ions versus the incident energy.

6.2.1 Sputtering with Ga ions at 30 keV

Figure 6.12 (a) shows the sputter yield of a polycrystalline tungsten sputtered with a 30 keV ion beam. As already mentioned, the white areas contain no sputter yields because no grains were measured with these crystal orientations. Over ten thousands of grains with different crystal orientations were investigated and the sputter yields visualized. As mentioned in section 6.1, the sputter yields were calculated from erosion depths (i.e. height measurements).

(a)

(b)

(c)
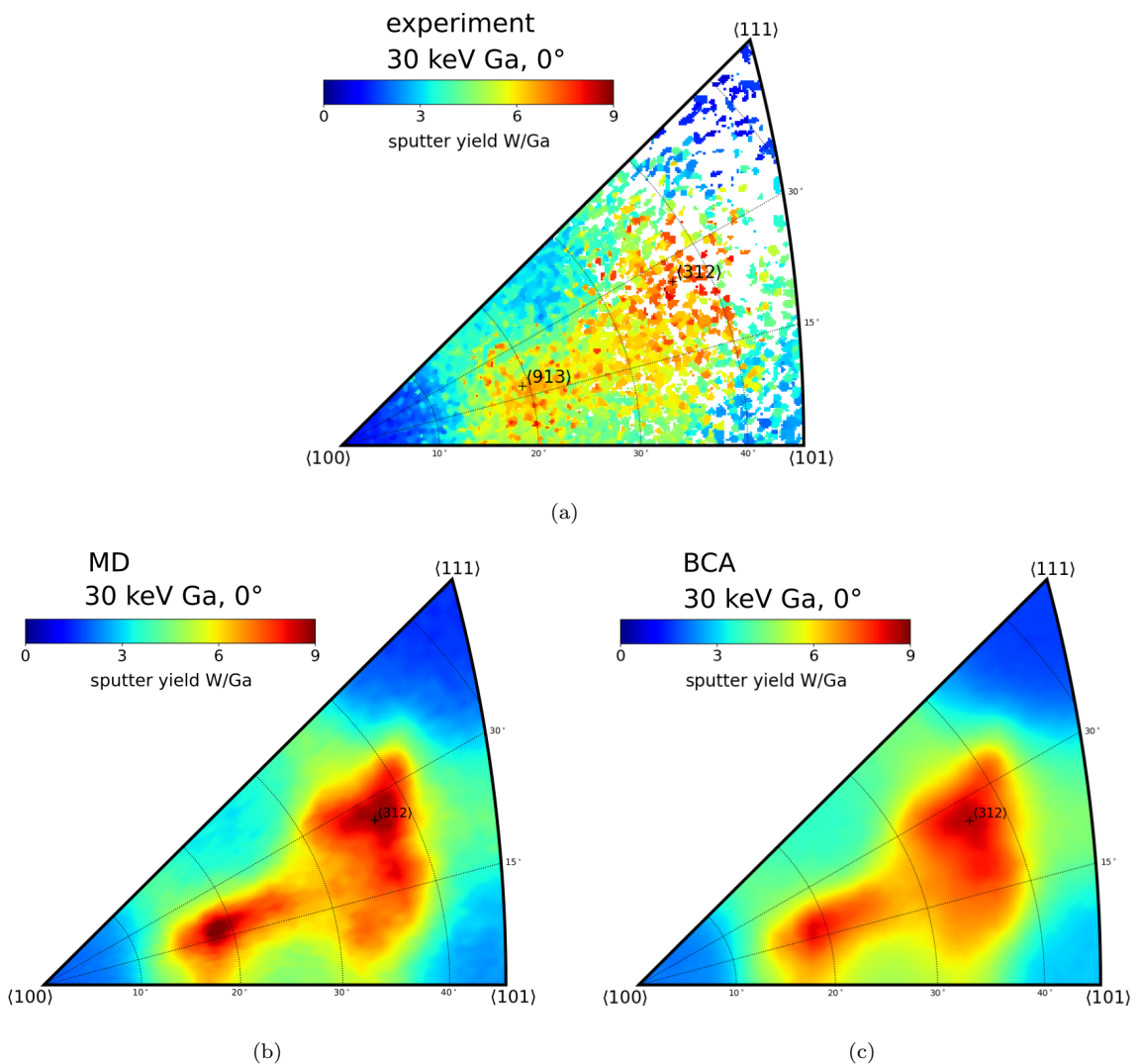
Figure 6.12: Sputter yields versus crystal orientations for tungsten sputtered with a 30 keV Ga ion beam: comparison of experimental data (a) to MD (b) and BCA simulations (c). The experimental sputter yields were calculated from the erosion depths shown in figure 6.3. Statistics for the experimental evaluations shown in (a) can be found in the appendix in figure A.4. The MD and BCA simulations were performed by Kai Nordlund and Gerhard Hobler, respectively [49].

63

The mean erosion depth is around 800 nm and as shown in the appendix in figure A.4, the SD is around 100 nm. The roughness prior to the sputter experiments was in the order of 100 nm.

The experimental results were compared to molecular dynamic (MD) and binary collision approximation (BCA) simulations and shown in figure 6.12. For BCA simulation, the software code IMSIL was used[106], which considers the crystal lattice of tungsten. IMSIL has originally been developed for the simulation of ion implantation in silicon[106], and has been augmented over the years for other crystal systems and to allow sputtering simulations[107,108].

The MD simulation was performed using the program MDRANGE, which is based on an implementation of MD recoil interaction approximation (RIA). RIA considers lattice interactions during ion irradiation[109,110] and provides the energy deposition of the ions in the tungsten surface. For transforming the energy impact to sputter yields, a few full MD simulations were performed. Since the MD and BCA simulations were performed by Kai Nordlund and Gerhard Hobler, respectively, only the simulation results were presented here as a comparison. The simulation details are available in[49].

As shown in figure 6.12, the experimental results and the two simulations are in very good agreement. The $\langle 100 \rangle$ and the $\langle 111 \rangle$ crystal orientation exhibit the lowest sputter yield and the sputter yields are around one order of magnitudes higher for the high index surfaces. The line diagrams show the agreement of the sputter yields clearer as a color scaled IPF. As a different visualization, the sputter yields from experiment and simulations were evaluated along lines in the IPFz, which are visualized in figure 6.15.

The two simulation approaches agree well to the experimental data. The highest differences between simulations and experiment are at $\langle 100 \rangle$ crystal orientation, however the reason for this discrepancy could not be solved.
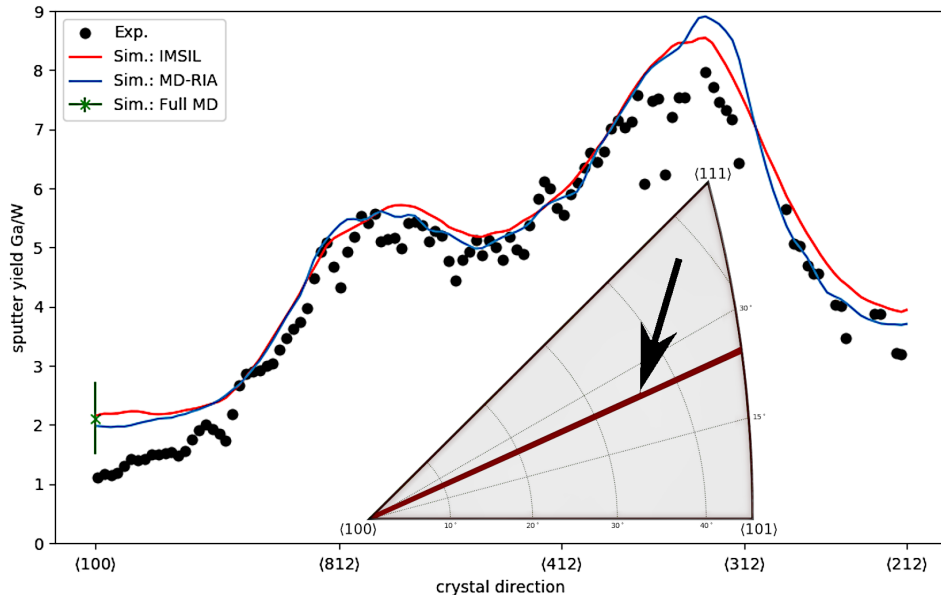
(a)
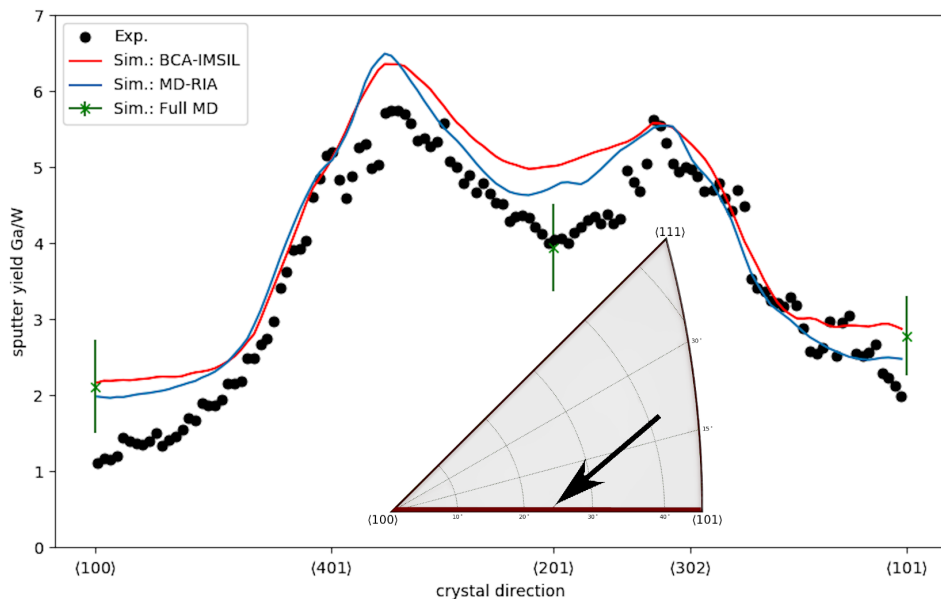
(b)

Figure 6.14: Sputtering of tungsten with a 30 keV Ga ion beam. Comparison of experimental data to MD and BCA simulations along the red line indicated by the black arrow. The experimental data was extracted from figure 6.12.
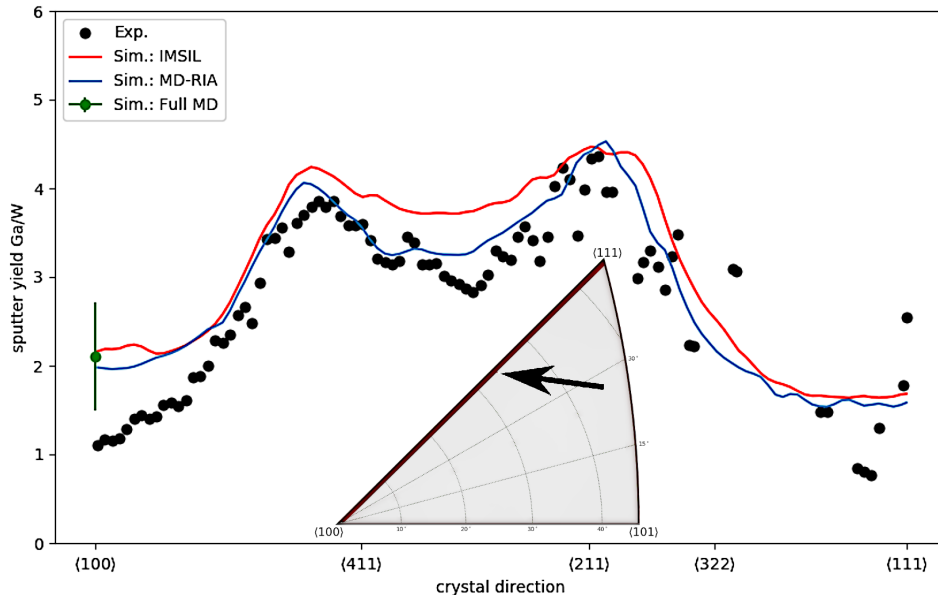
(a)
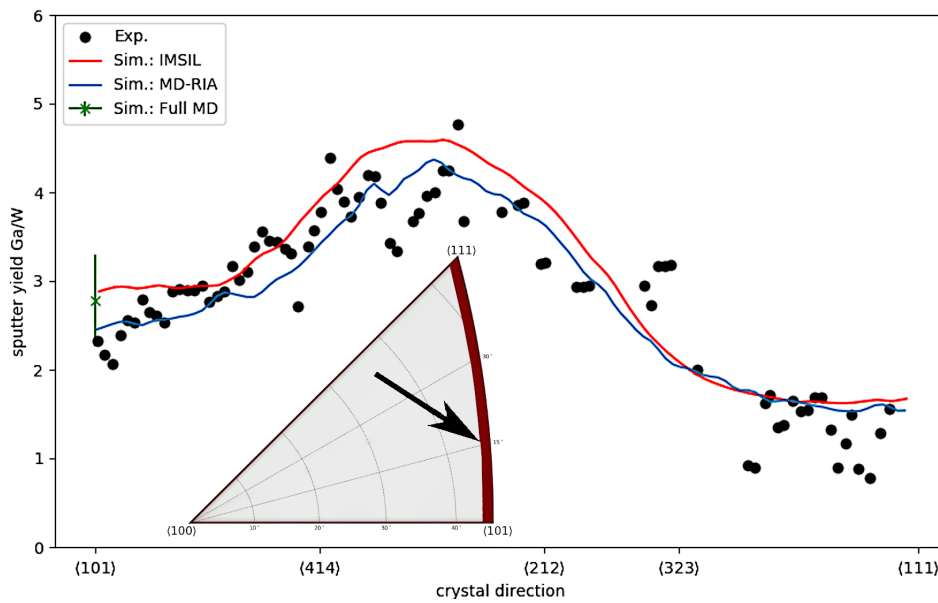
(b)

Figure 6.15: Sputtering of tungsten with a 30 keV Ga ion beam. Comparison of experimental data to MD and BCA simulations along the red line indicated by the black arrow. The experimental data was extracted from figure 6.12. Note that the red line in the IPF in (b) is thicker. The red line represents the area, where the values are taken.

6.2.2 Sputtering with Ga ions at 8 keV

Figure 6.16 shows the sputter yield versus the crystal orientation for 8 keV Ga ions on tungsten. Compared to sputtering at 30 keV, the distribution of the sputter yields was slightly different.
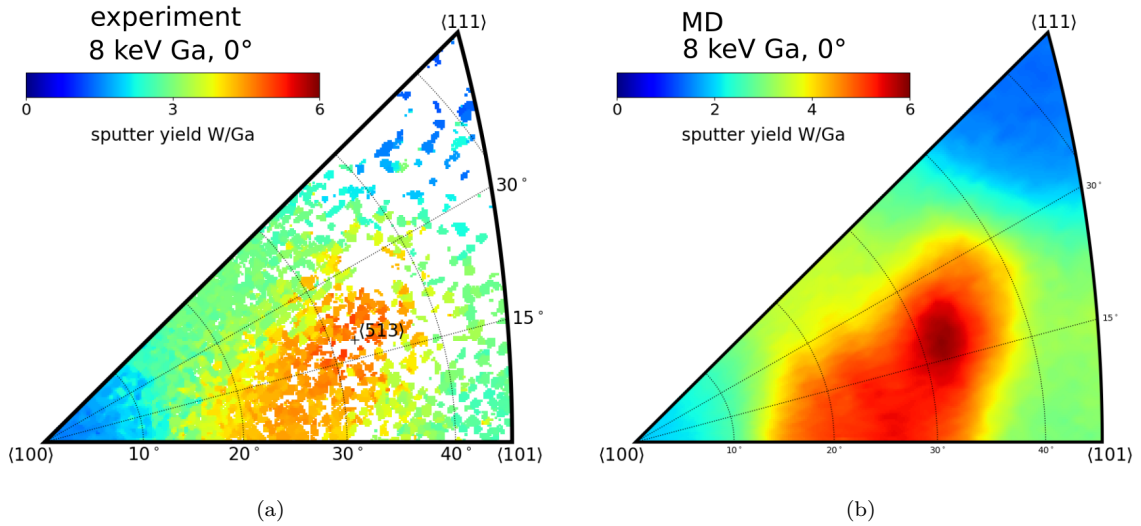
Figure 6.16: Sputter yields versus crystal orientations for tungsten sputtered with a 8 keV Ga ion beam: comparison of experimental data (a) to MD simulations (b). Statistics for sputter yield evaluations can be found in figure A.6 in the appendix. The MD simulations were conducted by Kai Nordlund.

Sputtering with 30 keV Ga ions shows two maxima at ⟨913⟩ and ⟨312⟩ crystal orientation in the IPF (see figure 6.12) whereas sputtering with 8 keV Ga ions shows one maximum at the ⟨513⟩ orientation in figure 6.16. In addition, the maximum is more smeared out for 8 keV Ga ions than for 30 keV Ga ions. The differences of the sputter yields between the low and high index surfaces were smaller for sputtering with a 8 keV Ga ion beam than for sputtering with a 30 keV Ga ion beam. Note the different scales in figure 6.12 and figure 6.16. The simulations and the experiments are again in very good agreement. The sputter data for 5 keV Ga is shown in the appendix in figure A.7.

6.2.3 Sputtering with Ga ions at 2 keV

The sputter experiments with 2 keV Ga ions have the highest experimental uncertainty. This is due to the flux density, which is described in section 6.1.2. Here only the high flux density sputter yields are presented. Due to the smaller sputter yields compared to a 30 keV Ga ion beam, the sputter time is longer for a 2 keV Ga ion beam. Therefore, a smaller amount of measurements was evaluated. Figure 6.17 shows the sputter yield versus the crystal orientation for a 2 keV Ga ion beam on the target tungsten. Compared to sputtering under 8 keV and 30 keV Ga ions the distribution of the sputter yield was again different.
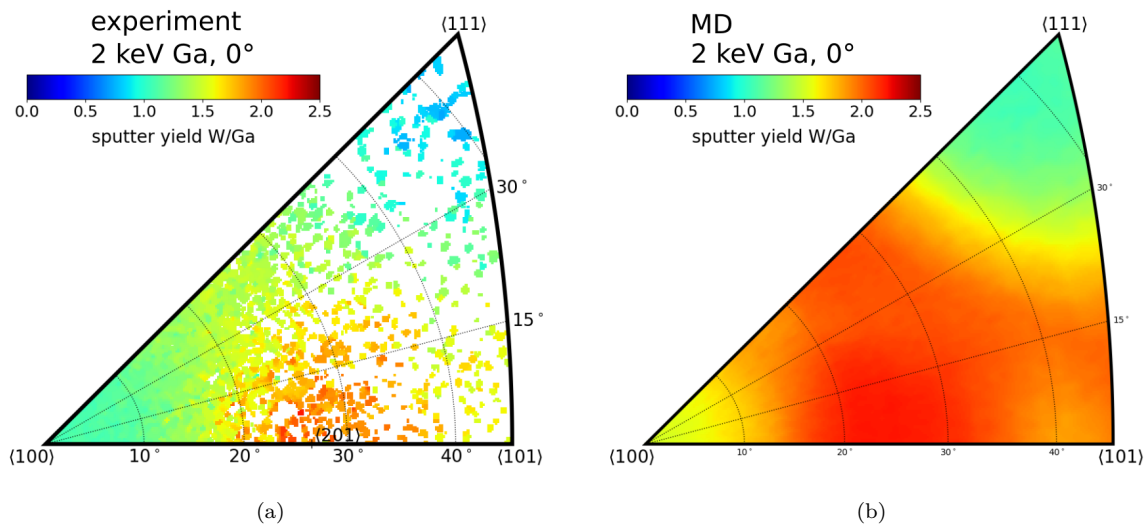
Figure 6.17: Sputter yields versus crystal orientations for tungsten sputtered with a 2 keV Ga ion beam: comparison of experimental data (a) to MD simulations (b). Statistics for sputter yield evaluations can be found in figure A.8 in the appendix. The MD simulations were conducted by Kai Nordlund.

For a 2 keV Ga ion beam, the differences of the sputter yield between the low and high index surfaces were smaller than for the higher energies. The channeling crystal orientations, e.g. ⟨100⟩, had nearly the same sputter yield as for a 30 keV Ga ion beam. In addition, these low index crystal orientations were only a factor of two different than the high index surfaces. The maximum sputter yield is located around ⟨201⟩ crystal orientation and different located as for the sputter experiment at 30 keV and 8 keV. A comparison was performed between the different energies for the experimental and simulated data points. Figure 6.18 shows for 2 keV, 8 keV, 30 keV the minimum, maximum, and averaged sputter yields. In addition, the sputter yields from SDTrimSP simulations are shown and they fit to the average crystal dependent sputter yields. The differences between minimum and maximum are higher for higher energies.
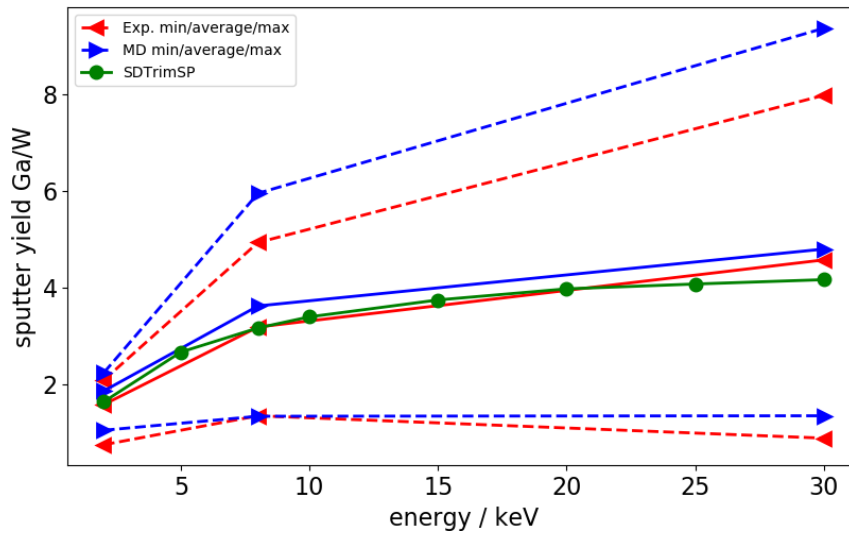
Figure 6.18: The dependence of sputter yields on the incident Ga ion beam energies: a comparison of the experimental data (red triangles) to the MD (blue triangles) and SDTrimSP (green dots) simulations is given. For the experimental data and MD simulations, the maximum and minimum sputter yields originated from figure 6.12, 6.16 and 6.17 are displayed. The minimum sputter yields are typically found at the low index surfaces. In the SDTrimSP simulations, the tungsten target is assumed to be amorphous.

Figure 6.18 shows that the minimum sputter yields are nearly constant for different energies. Typically, the smallest sputter yields were measured at the low index surfaces which fulfill the channeling conditions. From this follows that the major increase of the average sputter yields results from the high index surfaces.

6.3 Angle-dependent sputtering

In this chapter, angle-dependent sputtering results are presented and its application as an ion direction detector is described. It was discovered that sputtering is sensitive to less than 1° of the misalignment of the sample mounting, respective the ion impact angle. Therefore, an optimization algorithm was written. For optimizing data, it is common to work with the raw measurements and not with the processed values, which includes additional measurements like, sputter time, beam current and the sputtered area. Using the raw data makes the interpretation of the optimization easier and avoids mistakes. Therefore, the results are often presented in erosion heights and not in sputter yields.

It is known from literature[99] that the sputter yield changes with the impact angle of the ions. Figure 6.19 shows SDTrimSP simulations with different ion impact angles to the surface normal for 30 keV Ga ions on the target tungsten. From SDTrimSP simulations, the sputter yields are higher with higher impact angles until the impact angle reaches around 77°. Beyond this impact angle, reflection of Ga ions dominates. The reflected Ga ions do not enter the tungsten target and therefore, the sputter yield decreases. In figure 6.19, the dashed black lines show impact angles, which were selected for the experiments.
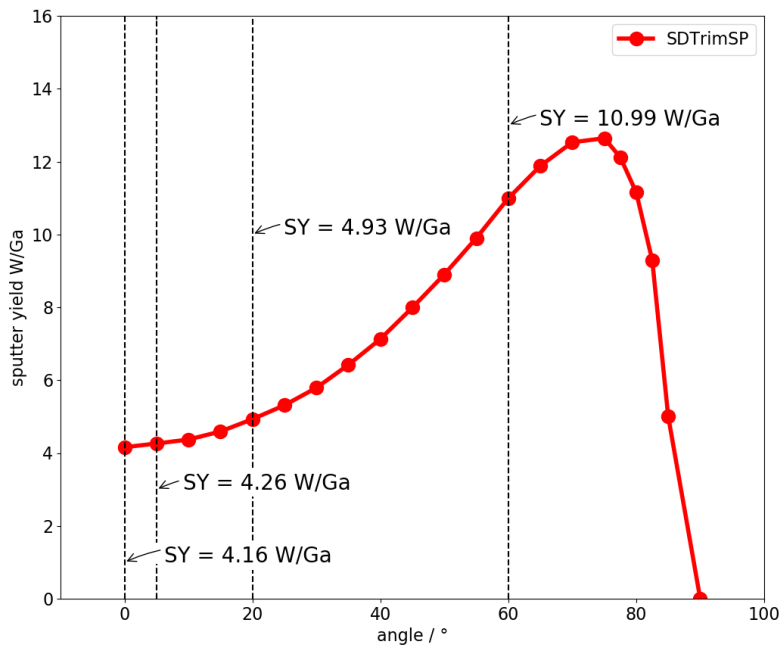
Figure 6.19: SDTrimSP simulations on the sputter yields of target tungsten (W) using a 30 keV Ga ion beam with various incident angles with respect to the surface normal. The black dotted lines highlight the incident angles used for the sputter experiments.

An angle of 5° was selected to test the sensitivity to the impact angle. In principle,

the experiment was an estimation of the misalignment error of the ion beam or the misalignment error of crystal-orientation measurement. An angle of 20° was selected, because the change of the sputter yield is moderate and should show similar results as sputtering perpendicular to the surface. Therefore, this data set was suitable to optimize the data according to the impact angle of the ions. For 60° the sputter yield is more than two times higher compared to 0° and could show an inhomogeneous increase of the sputter yield, which means that some crystal orientations show a different behavior to the impact angle of the ions. For the experiments, again the scanning FIB was used with indentical settings as for the other experiments. As the area increases due to the angle of 60° by a factor of 2, the fluence is a factor of two lower. Of course this effect is valid for all angle dependent sputter experiments, but the area increase is low below 20°. As already shown for the 30 keV Ga ion beam, the sputter yields do not depend on the fluence or flux density and the area increase should also be negligible for higher impact angles than 20°.

Except for sputtering under 5°, all erosion depths in this section are similar, e.g. between 0 µm and 1.5 µm, which includes the data of the figures (6.3, 6.21, 6.22). This allows a good comparison between 0°, 20° and 60° impact angle of the ions.

6.3.1   Sputtering under 5°

According to simulations, shown in figure 6.19, the sputter yield is only slightly higher for sputtering under 5° to the surface normal than sputtering under the surface normal. Therefore, it is expected to get the same distribution of sputter yields as for the impact angle to the surface normal, shown in figures 6.3 and 6.12. Sputtering under 5° should show the sensitivity of the experiment to the misalignment error due to sample mounting or other alignment errors, e.g. calibration of the EBSD detector.

The erosion depths in the IPF were evaluated to the surface normal (IPFz) and by using equation 2.5 the crystal orientations are rotated to evaluate the sputter yields in the IPF to the direction of the impact angle of the ions (IPFion). Figure 6.20 (b) shows the evaluation to the ion beam and this figure has the same sputter yield distribution as for sputtering under the surface normal (figure 6.12). Figure 6.20 (a) shows the evaluation of the crystals to the surface normal and the sputter yield distribution of the IPFz does not fit at all to the sputter experiment under the surface normal (figure 6.12). Obviously already 5° is enough to loose the previously measured and calculated correlation of the sputter yields.
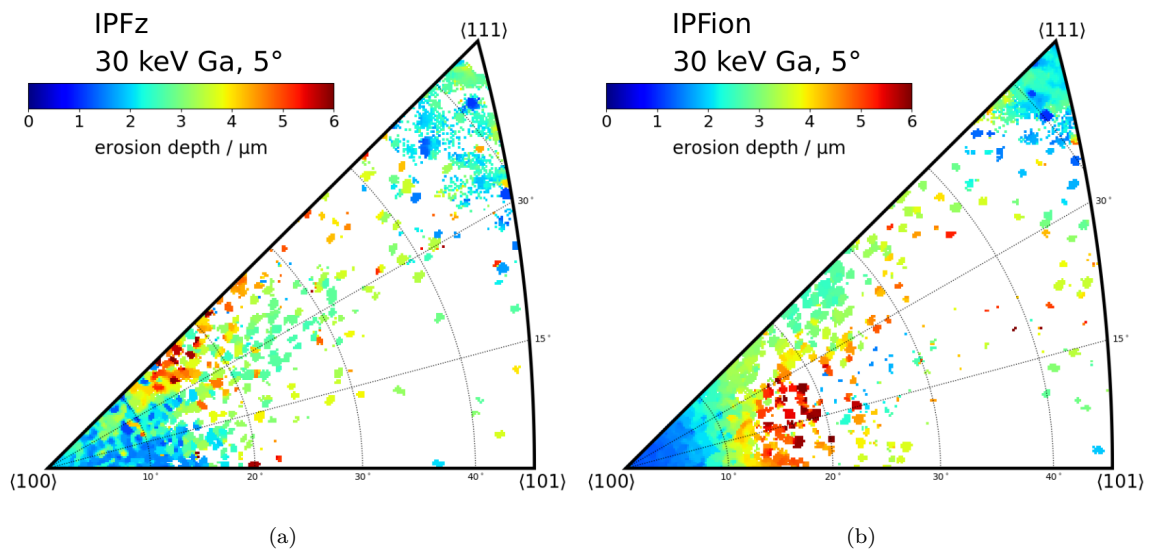
Figure 6.20: Influence of evaluation methods of crystal orientations on the correlation of the erosion depths of tungsten sputtered with a 30 keV Ga ion beam under an incident angle of 5° with respect to the surface normal: (a) crystal orientations were evaluated to the surface normal (IPFz), (b) crystal orientations were evaluated relative to the ion beam direction (IPFion).

The erosion depth was unexpectedly high in figure 6.20. A reason could be the condition of the FIB. Normally, the Ga reservoir should be exchanged every 1000 h and the Ga reservoir in the FIB was already over 2500 h used. Therefore, the FIB was overdue for service. The current measurement before and after the experiment was different and not constant as for all other sputter experiments. Also, the current was in both measurements above 30 nA. With the used settings of the FIB, usually the current is around 19 nA. Due to the uncertain ion current, only the erosion depth distribution to the crystal orientation was compared and not the absolute erosion depths.

6.3.2 Sputtering under 20°

The sputter experiment was performed with a 30 keV Ga ion which was tilted 20° from the surface normal. The evaluation strategy was the same as for sputtering under 5° from the surface normal.
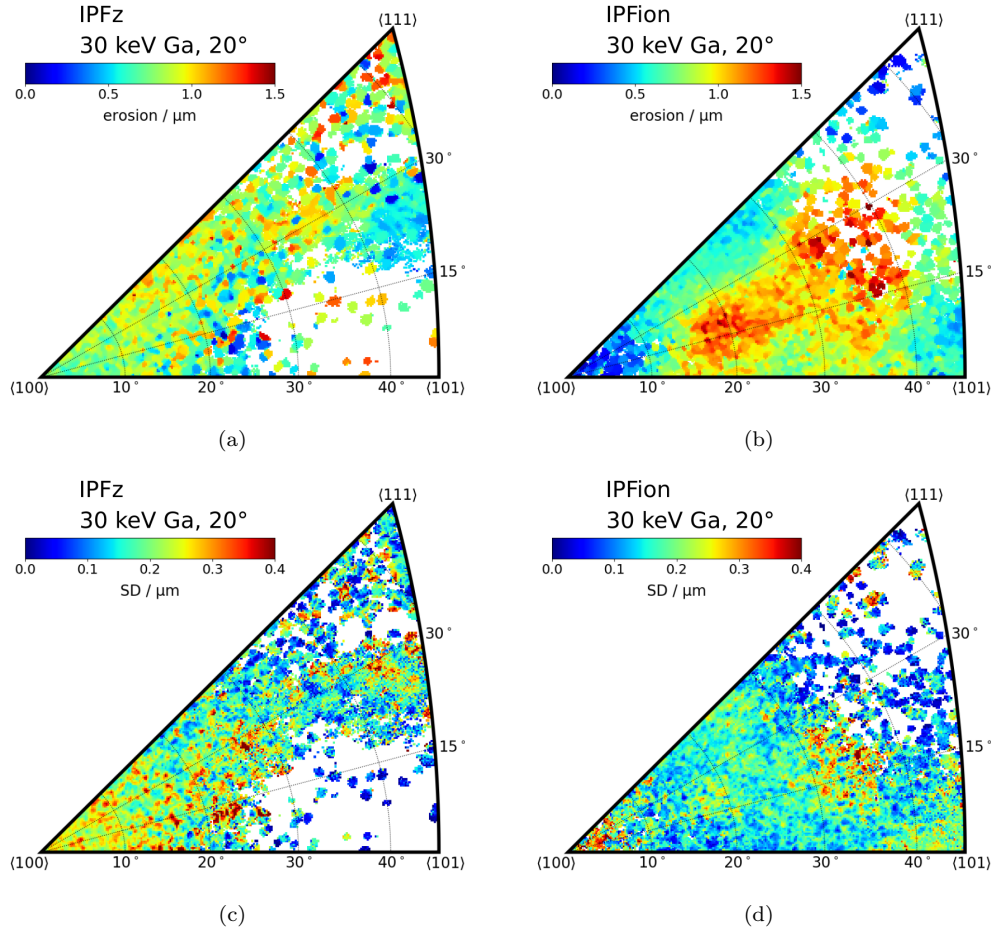
Figure 6.21: Influence of evaluation methods of crystal orientations on the erosion depths of tungsten sputtered with a 30 keV Ga ion beam under an incident angle of 20° with respect to the surface normal: (a) crystal orientations were evaluated to the surface normal (IPFz), (b) crystal orientations were evaluated relative to the ion beam direction (IPFion), (c) the SDs of the errosion data in (a), (d) the SDs of the errosion data in (b).

Figure 6.21 (a) shows the erosion depths versus the crystal orientations evaluated to the surface normal in an IPFz. In this evaluation a random distribution of the erosion was observed. In figure 6.21(b), the erosion depths were plotted versus the crystal orientation evaluated in the direction of the ion beam in an IPFion. They show a similar erosion distribution as for sputtering under the surface normal. The SDTrimSP simulations (figure 6.19) show an insignificant increase of the sputter

yield between sputtering under the surface normal and sputtering 20° from the surface normal. Therefore, a similar distribution of the erosion depths was expected.

6.3.3 Sputtering under 60°

For sputtering under 60°, the evaluation of the crystal orientation was only performed under the impact angle of the ions (IPFion) and the result of the erosion versus the crystal orientation is shown in figure 6.22.
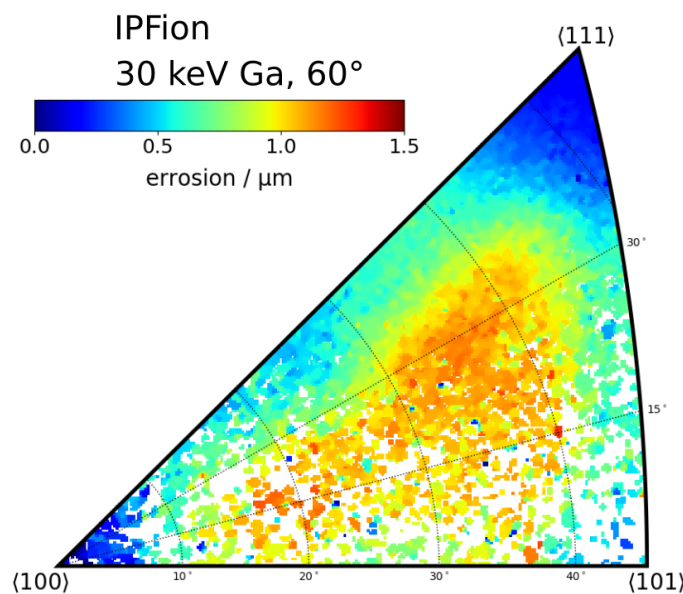
Figure 6.22: Erosion depth versus crystal orientations for tungsten sputtered with a 30 keV Ga ion beam under an incident angle of 60° with respect to the surface normal. The crystal orientations were evaluated relative to the ion beam direction (IPFion).

The ratio between lowest erosion depth and highest erosion depth is a factor of 8 and is similar compared to sputtering under 0° to the surface normal. Since the fluence is a factor of two lower, because the area increases by a factor of two due to the impact angle of 60° to the surface normal, the resulting sputter yields are around a factor of 2 higher compared to the sputter experiments under 0°. The sputter yields are visualized in figure 6.6(a). As expected from the calculations for the average sputter yield by SDTrimSP, the crystal orientation dependent sputter yields are also significantly larger.

6.3.4 Comparison of angular distribution of the sputtering

Four different impact angles (0°, 5°, 20°, 60°) were studied with a 30 keV Ga ion beam. Since the ion beam was not stable during the experiment for the impact angle of 5°, the other three impact angles are compared to each other in this section.

Figure 6.23 shows a comparison of angle dependent sputter yield data of SDTrimSP simulations and the experimental sputter yields. The fluence of the experimental sputter yields were the same and the minimum, mean and maximum sputter yields are visualized. Although there is a higher spread of the sputter yields in absolute values towards higher impact angles, the ratio between minimum and maximum is about the same. In general, the simulations are in well agreement with the experimental data.
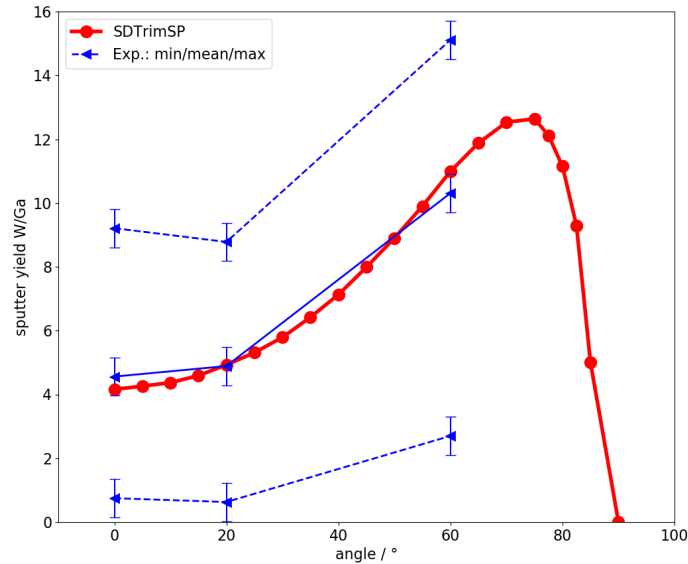
Figure 6.23: SDTrimSP simulations of the tungsten sputter yields using a 30 keV Ga ion beam with various incident angles with respect to the surface normal. The blue line is the mean sputter yield and blue dotted lines highlight the min and the max sputter yield of figure 6.30, 6.21 and 6.6(b).

Crystal-dependent sputtering under the surface normal shows clearly two maxima in the IPF at the high index surfaces in figure 6.12 respectively 6.30, whereas sputtering under 60° to the surface normal does not show two maxima at the high index surfaces in the IPF (figure 6.6). Therefore, under each impact angle, e.g. 0°, 20° and 60°, the amount of the sputter yield values was counted for each IPF. Several crystal directions have a similar sputter yield analyzed by frequency distribution analysis, which is shown in figure 6.24.

For a better comparison of the frequency distribution analysis, the sputter yields under an impact angle of 60° to the surface normal were plotted a second time, but re-scaled with the ratio of the mean sputter yield under 0° and 60° to the surface normal, which is $\frac{4.56\,\text{W /Ga}}{10.31\,\text{W /Ga}} = 0.443$.

In figure 6.24, it is visible that two peaks, respectively the two maxima, have shifted between sputtering perpendicular and 60° to the surface normal. For sputtering under 60°, more crystal directions have higher sputter yields compared to sputtering under the surface normal. In other words, two crystal orientations have two different functions which could describe the sputter yield for different impact angles.

This is an interesting fact and it shows that angle-dependent sputter yields can not be described by one $\cos(\phi)$ function, which is often done[28]. Maybe this effect is due to linear collision sequences. Some crystal orientations could have a stronger increase of linear collision sequences compared to other orientations. This would change the frequency distribution analysis.
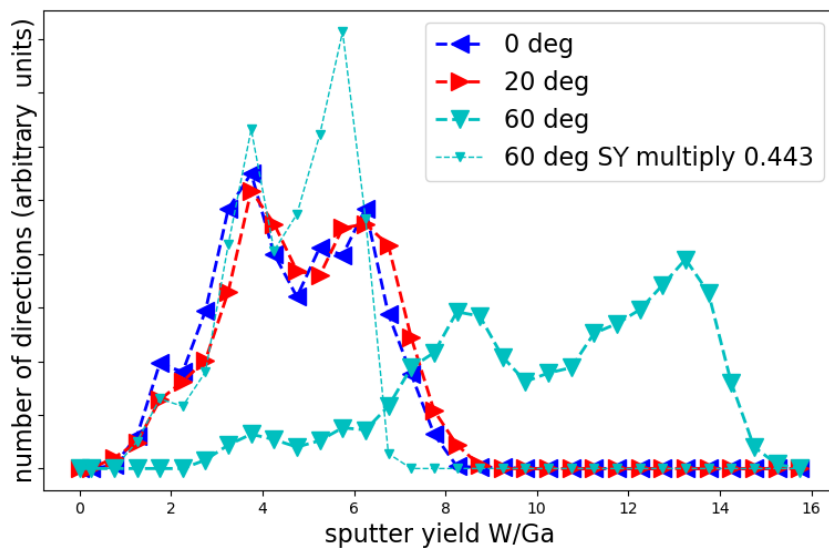
Figure 6.24: Number of crystal directions versus sputter yield for tungsten sputtered with a 30 keV Ga ion beam. For a better comparison the data sputtered under an angle of 60° is shown a second time but re-scaled with the ratio of the mean sputter yield under 0° and 60° to the surface normal. The sputter yield distribution changed between them.

6.4 Ion impact angle detection

The sputter experiment with an impact angle of 5° showed that the known distribution of crystal-dependent sputter yields was lost (see figure 6.20). Due to the high sensitivity of the evaluation to the direction of the ion beam, a method was developed to detect the impact angle of the ions. In principle, different ways are possible to detect the impact angle of the ions or the misalignment error of the experimental setup. Two of them are described here with sputter data of a 30 keV Ga ion beam under an impact angle of 20° on the target material W.

6.4.1 Minimizing the error

For finding the impact angle of the ions, the error was reduced between the sputter yields for different single crystal grains. Ten thousands of single crystal grains were rotated in 0.33° steps of ϕ by using equation 2.5 and the error of the erosion depth of each crystal orientation was determined for every possible ion impact angle. The used error was the SD, which is not the optimal statistic value because it ignores the amount of measurements. In future, this should be optimized, e.g. with the "mean absolute error". For each rotation step of tilt angle ϕ, the SD was calculated for each crystal orientation. Often, many grains corresponded to the same crystal orientation and for each rotation matrix multiplication a new arrangement of grains corresponded to the same crystal orientation.
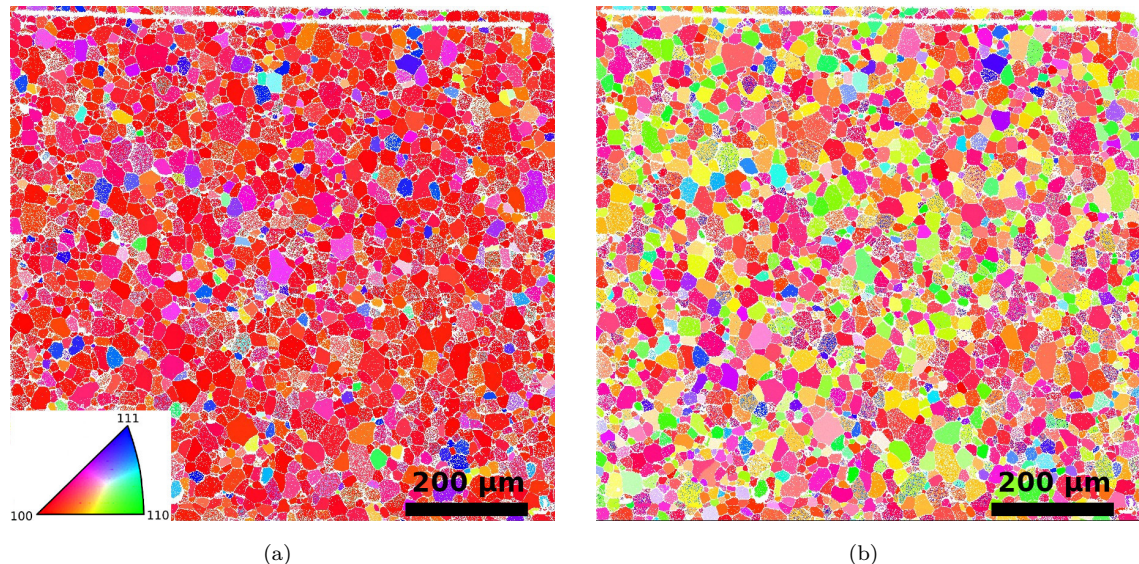
Figure 6.25: One EBSD measurement presented in two orientation maps. (a) shows the crystal orientation to the surface normal (IPFz) and (b) shows crystal orientation under ϕ =20° to the surface normal (IPFion). The EBSD color scale shows a new pattern in (b) compared to (a).

To illustrate this, one EBSD map is shown in figure 6.25 in two different perspectives of the same area for the tilt angle $\phi = 0°$, which corresponds to an IPFz, and $\phi = 20°$, which corresponds to an IPFion. In these images, grains with the same color have the same crystal orientation for a perspective, e.g. IPFz. By changing the perspective, a new arrangement of grains shows the same color, respectively the same crystal orientation.

In one IPF figure, thousands of sputter yields were evaluated and therefore, thousands of SDs were calculated for each tilt angle. To generate one value over the whole IPF, the average value was taken of all the derived SDs for each tilt angle ϕ and visualized in figure 6.26. A minimum of the error is visible at $\phi = 20°$, which is the impact angle of the ions. This method will not work for poor data sets, which means a lot of crystal orientations were not evaluated because of a textured sample or an insufficient amount of grains was measured. An example of an insufficient data set is shown in figure 6.20.
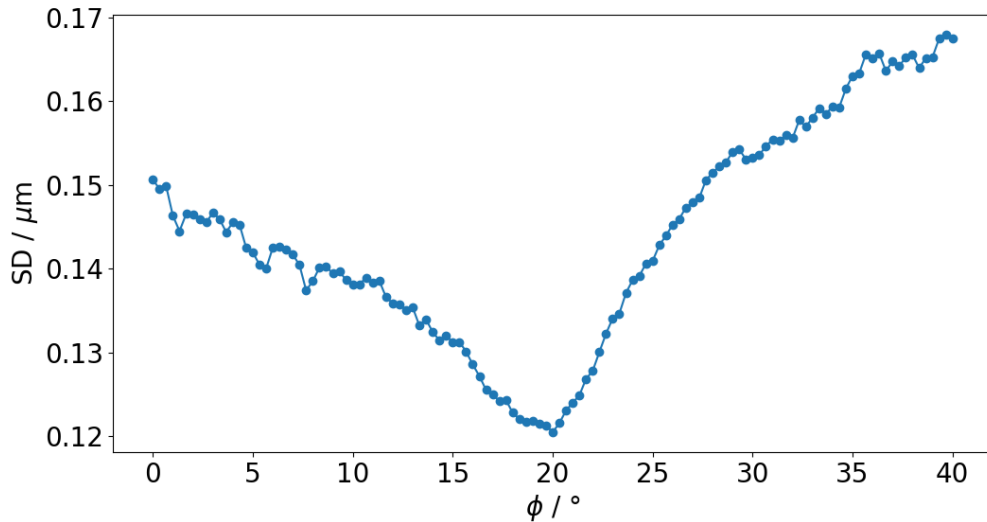
Figure 6.26: Average SD versus the tilt angle of the IPF. For example for $\phi = 0°$ the average of the SDs of figure 6.21(c) and for $\phi = 20°$ the average of the SDs of figure 6.21(d) is given. More IPFs examples with different tilt angles ϕ are shown in figure 6.27. At the lowest SD the crystal orientation of the grains was directed to the ion beam. The W sample was sputtered under 20° to the surface normal with a 30 keV Ga ion beam, which is in line with the proposed evaluation scheme.

6.4.2 Principal component analysis

A principal component analysis (PCA) is a second method to find the impact angle of the ions. An IPF is a reduced representation of a linear projection, which includes 24 symmetry points in a bcc lattice.
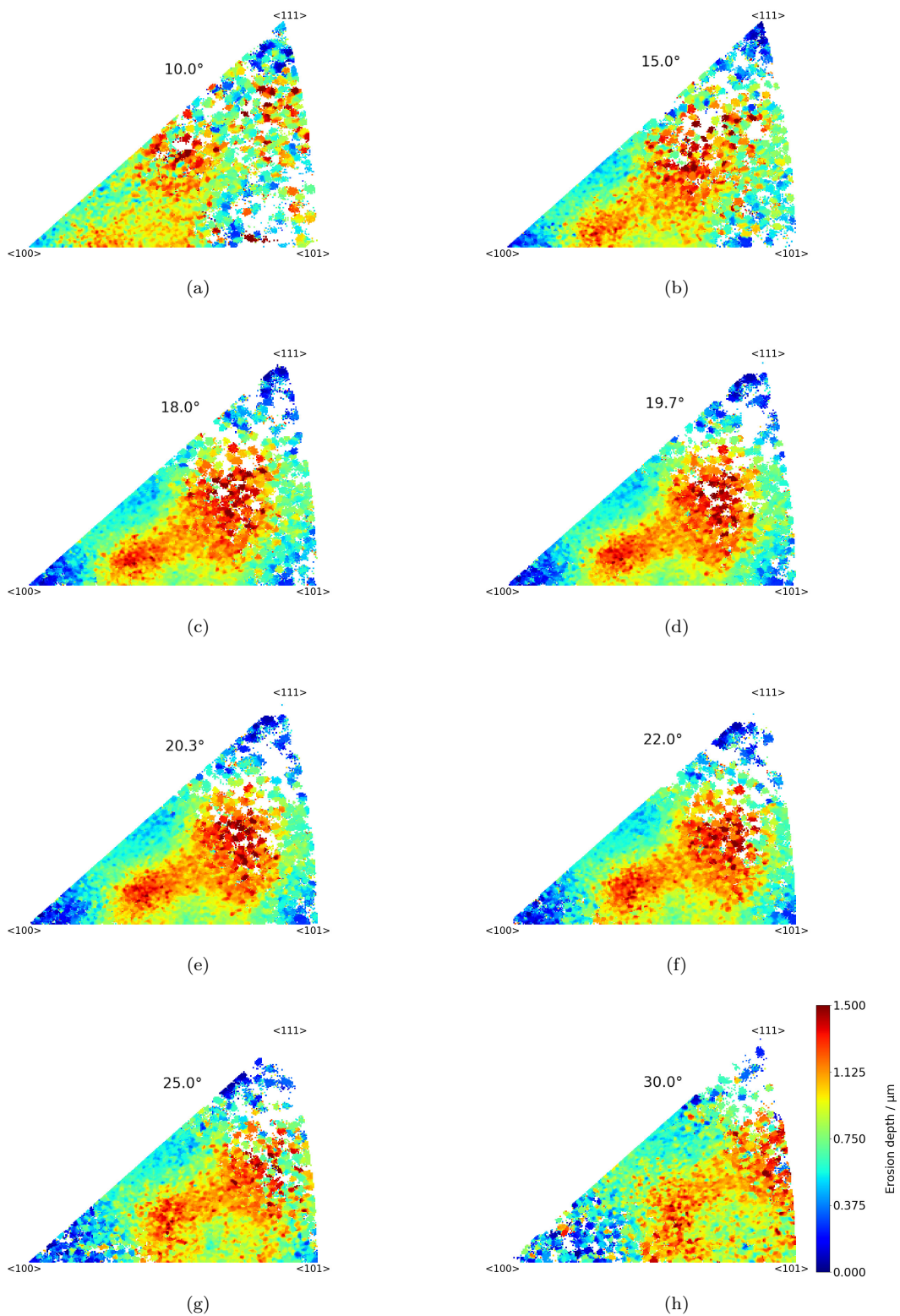
Figure 6.27: Influence of misalignment angles of crystal orientations to the surface normal on the erosion depths of tungsten sputtered with a 30 keV Ga ion beam under an incident angle of 20° with respect to the surface normal: (a) 10°, (b) 15°, (c) 18°, (d) 19.7°, (e) 20.3°, (f) 22°, (g) 25°, (h) 30°.

79

"The main idea of PCA is to find a linear projection of the data that optimally matches the data structure in the well defined sense of accounting the maximum amount of variance that can be captured in the lower dimensional representation of the data"[111].

In principle, this technique is similar to the one used above, but focuses not on the error between the measurements for one crystal orientation. Instead, the method focuses on the highest differences on the measured data in the IPF, which are the differences of the erosion depths. For the PCA, the full data set with the three Euler angles was used to rotate every measured crystal orientation with equation 2.5 in 0.33° steps of ϕ (see Euler angle chapter 2.2).
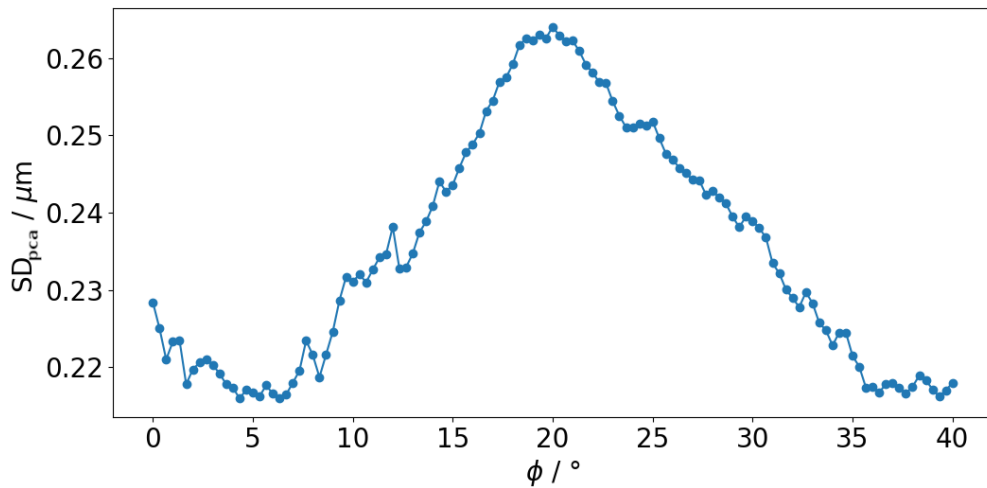
Figure 6.28: SD$_{\mathrm{pca}}$ of erosion depths as a function of the misalignment angles. The erosion of target tungsten was caused by sputtering with a 30 keV Ga ion beam under an incident angle of 20° with respect to the surface normal. The standard deviations of the IPF calculated at $\phi = 0$ and $\phi = 20$ correspond to the cases shown in figure 6.21. The standard deviations at a few other misalignment angles were calculated based on figure 6.27.

For a cubic crystal lattice, an IPF is $1/24^{th}$ of a pole figure and it is a reduced representation of all 24 symmetric elements of a pole figure into a triangle. The first Euler angle φ_1, which rotates the crystal lattice around representation plane normal, is not taken into account in an IPF, whereas for the rotation matrix multiplication the first Euler angle φ_1 is necessary. Each rotation matrix multiplication resulted in a new arrangement of the erosion depths in the IPF. For the PCA, the SD was taken of all evaluated erosion depths in the IPF and for this work, the SD taken by the PCA is called SD$_{\mathrm{pca}}$. The SD$_{\mathrm{pca}}$ was plotted to the second Euler angle ϕ (tilt angle around the X axis of the sample surface plane, see figure 2.3) in figure 6.28. The SD$_{\mathrm{pca}}$ of the erosion depths is in other words the differences between the erosion depths. The maximal SD$_{\mathrm{pca}}$ was searched.

If the chosen ϕ is close to the impact angle of the ions, the distribution of sputter yields fits to figure 6.3 and the maximum SD_{pca} was found at $\phi = 20°$, which is shown in figure 6.28.

A few IPFs of this evaluation are shown as examples in figure 6.27. The SD_{pca} was taken over these data points. In figure 6.27, the influence of the misalignment ϕ is visible to the erosion depth. Already 2° mismatch ends in a "blurry" IPF. As a result of these figures, the sensitivity is very high to the misalignment angle, e.g. error angle due to sample mounting, respectively to the impact angle of the ion. Since the method looks promising for detecting the impact angle of high energetic ions at the material surface, the sensitivity of the impact angle detection will be investigated in the next section in more detail.

As figures 6.26 and 6.28 show, both methods yield similar results and the best optimization procedure depends on the experimental data set. Probably the PCA provides better results for higher energies, because the crystal-dependent sputter yields show a higher variance (see figure 6.18).

6.4.3 Optimization of 30 keV sputter data

Section 6.4.1 and 6.4.2 show that sputtering is sensitive at least to the impact angle of the ions around 2°. Also it shows, that it is possible to find the impact angle of the ions through PCA or to minimize the error between the measurements and to correct this misalignment during the evaluation. The sputter experiment with 30 keV Ga ion perpendicular to the surface consists of 4 independent data sets. But the evaluation in the IPFz shown in figure 6.17, was done by combining them to one data set.
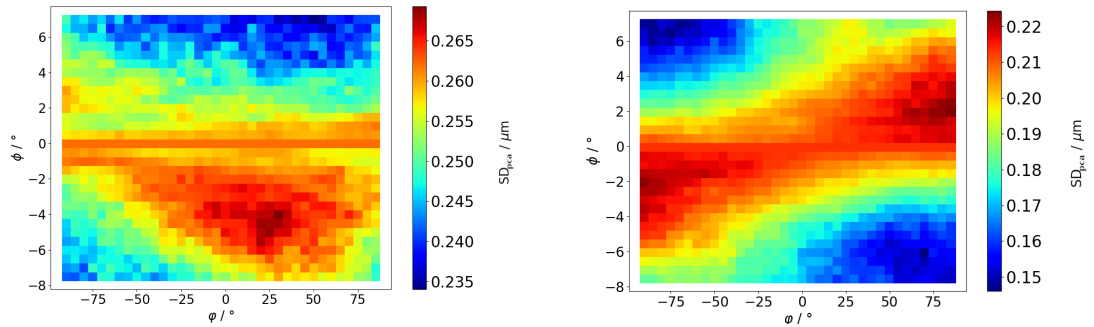
(a) The sample misalignment is in $\varphi_{max} = 30°$ and in $\phi_{max} = -4°$.

(b) The sample misalignment is in $\varphi_{max} = 80°$ and in $\phi_{max} = 2°$.
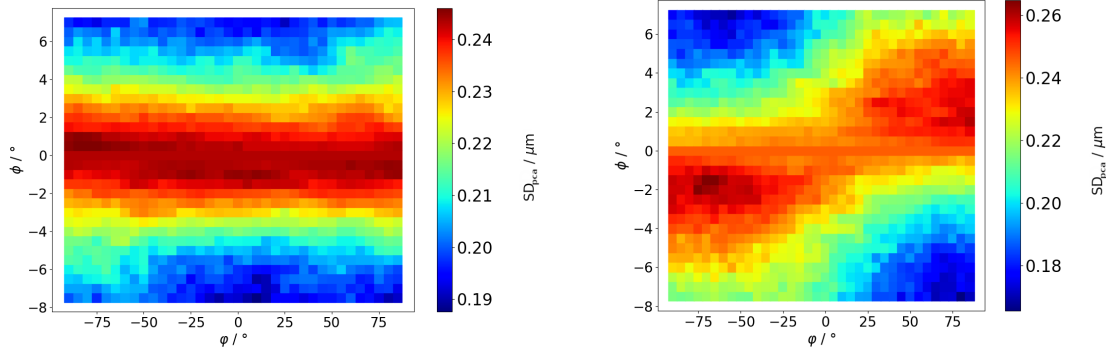
(c) The sample misalignment is in $\varphi_{max} = -90°$ and in $\phi_{max} = 0.5°$.

(d) The sample misalignment is in $\varphi_{max} = -70°$ and in $\phi_{max} = -1.5°$.

Figure 6.29: PCA evaluation shows the misalignment error of the sample mounting in the 4 different experiments. SDs_{pca} are shown in regard of two Euler angles. The crystals were twisted in ϕ and φ, which results in a different SD_{pca} for the IPF. A second illustration of these figures are polar plots, which are shown in the appendix in figure A.9. The maxima SD_{pca} is used to find the angles to correct the misalignment with equation 2.5. The four corrected data sets were combined and visualized as an IPF shown in figure 6.30.

By these experiments, the EBSD measurements were not performed on the same day as the sputter experiments, which means that for the sputter experiments and

for the EBSD measurements the samples were mounted independently. Therefore, each mounting procedure could include another error and that can be checked by calculating them separately.

Figure 6.29 shows the PCA results independently for the four data sets sputtered with a 30 keV Ga ion. In these data sets, the angles which had the maximum SD_{pca} were taken to correct the measurements with roation-matrix multiplication for each measurement (see equation 2.2). For the four sputter experiments the highest SD_{pca} was found for $\phi_{max} = 0.5°$, -1.5°, 2°, -4° and $\varphi_{max} = $ -90°, -70°, 80°, 30°, respectively. The strong variation of φ is not surprising, because φ is a rotation around the surface normal and a rotation of 90° means that the tilt axis for ϕ is now the Y axis instead of the X axis (see figure 2.3 and for this case is X' = Y). Note that only a rotation φ ($\phi = 0$) does not change the crystal orientation to the surface normal in an IPF representation. The correction by $\phi_{max} = $ -4° resulted from an obvious sample misalignment, which was already noticed after the experiment. The optimized IPF is shown in figure 6.30(b). After the correction, the distribution of the sputter yields of figure 6.30(b) is more similar to the simulations of figure 6.12(b) and (c) than the distribution of the sputter yields of figure 6.30(a) and 6.12(a).

(a)

(b)
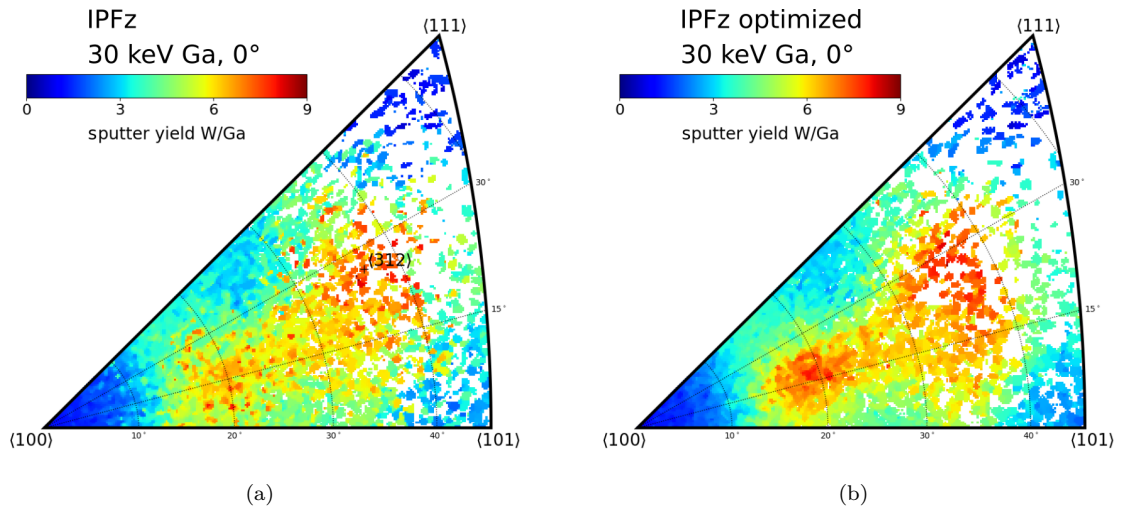
Figure 6.30: Sputter yields versus crystal orientations. (a) the evaluation without optimization as already shown in figure 6.12(a). (b) after correcting the measurements by rotation matrix multiplication due to PCA (see figure 6.29). The sputtering experiment was performed on a polycrystalline tungsten sample using a 30 keV Ga ion beam. The optimized figure looks much clearer than the non-optimized figure.

To illustrate the error of the impact angle detection algorithm, figure 6.31 shows the SD_{pca} to ϕ_{max} for a constant $\varphi = \varphi_{max}$. With a fixed rotation angle φ_{max}, the four maxima of the SD_{pca} to the impact angle ϕ is clearly visible. If in figure 6.31 one of the four curves was shifted by 1°, it would be clearly off the others. This shows that the impact angle ϕ can be evaluated better than 1° accuracy. In addition,
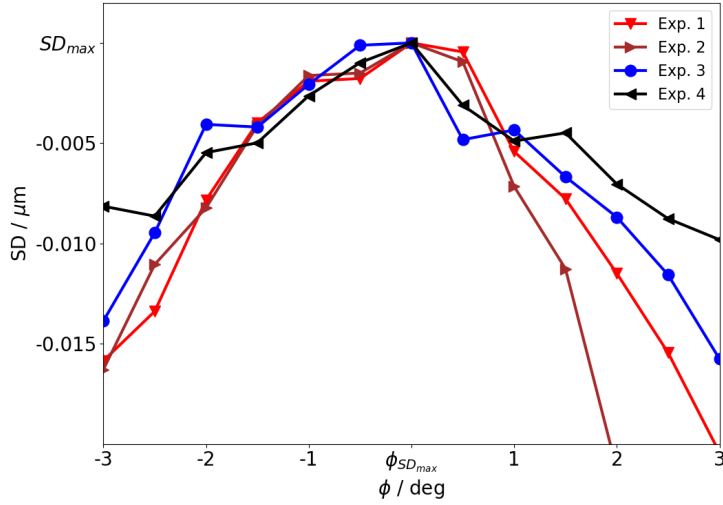
Figure 6.31: Standard deviations as a function of misalignment angles for four different sputter experiments shown in figure 6.29. The standard deviations were evaluated by the PCA analysis. The maximum standard deviation for each experiment is normalized to 0.

the corrections of the impact angles ϕ of around 2° (ϕ_{max} = 0.5°, -1.5°, 2°, -4°) in figure 6.30 show a significant effect in the IPF, which illustrates the sensitivity of the impact angle detection algorithm. The sensitivity and therefore, the resolution of the impact detection algorithm correlates with the width of peak shown in figure 6.31.

It can be hypothesized that the width of that peak is due to the ion impact angle distribution of the FIB and not due to the EBSD measurement. A FIB scans over the sample and deflects the ion beam around 1°. An estimation of the maximum deflection angle can be done with the working distance of the FIB and the scan area of the FIB. The working distance of the used FIB was around 16.5 mm and the maximum scan area was around $1000 \times 1000 \, \mu m^2$.

To verify the assumption, the scan area was split in 4 smaller scan areas and each area was sputtered with a 30 keV Ga ion beam. The stage was not moved during the experiment, only the ion beam was deflected. The sputtered areas are shown in figure 6.33. If the accuracy of the ion impact angle detection is better than 1°, the algorithm should detect different impact angles in each sputtered area and all four ion directions should point to one spot, which is the source of the FIB.

The distance between the center of each sputtered rectangle is around 400 µm in figure 6.33. Therefore, the maximum difference in the impact angle is

$$\arctan(\frac{0.4\text{mm}}{16.5\text{mm}}) = 1.4° \quad (6.1)$$

between the areas. Since the lens system of a FIB does not end at the pole peace, which means that the deflection point is inside the FIB, the distance to the deflection

point is even larger than 16.5 mm. Therefore, the difference of the impact angles would be smaller than 1.4° by detecting the impact angles of the 4 areas. The 1.4° is an upper boundary value of the impact angle variation.
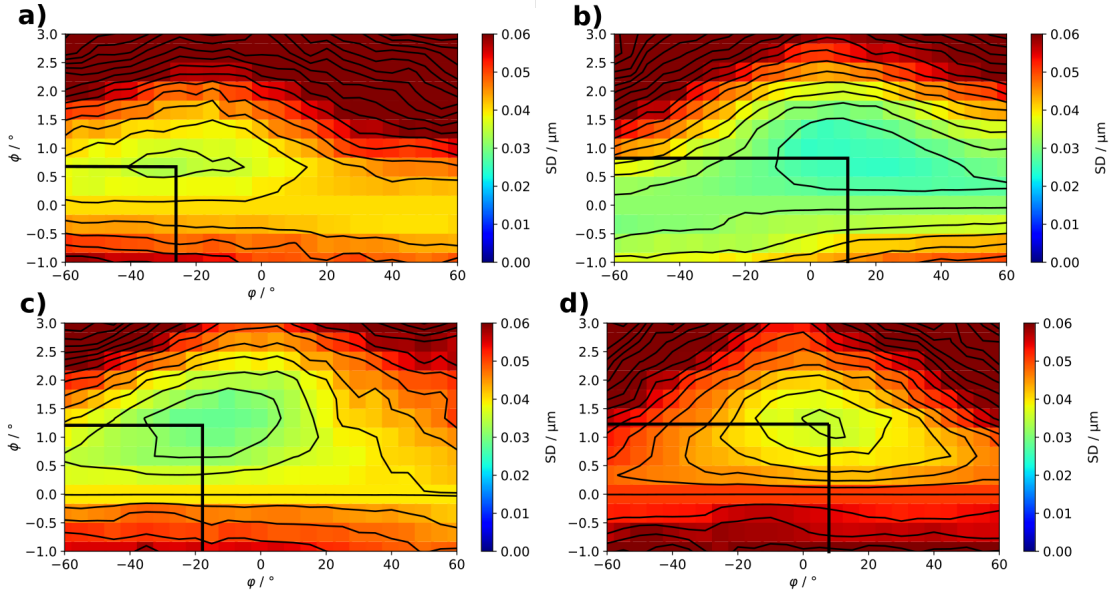
Figure 6.32: Mean standard deviations between the erosion measurement of different perspectives due to two different Euler angles. The minimal standard deviation was used to find out the impact angle of the ions.

After the sputter experiment, the 4 areas were evaluated separately and the impact angles were detected with the detection algorithm introduced in section 6.3. Due to the smaller sputter area only a low number of sputter grains were measured. Thereby the sputter yields of around 300 grains were evaluated. As already shown in section 3.1, the sample has a strong texture, which is in this case an advantage. For finding the impact angle of the ions, the SD between the sputter yields is minimized in the IPF-corner of the $\langle 100 \rangle$ orientation. The result of the impact angle detection is shown in figure 6.32 and illustrated in figure 6.33 with a circle which has a line of the radius. The radius length illustrates the impact angle ϕ and the direction of the radius line was selected due to the rotation angle φ.

The difference of the impact angle ϕ is around 0.5° between the sputtered area (a)/(b) and (c)/(d) shown in figure 6.33. This is often a negligible error for the electron microscopy, because small structures are investigated with this kind of microscopes. The differences of the impact angle fit to the above mentioned assumptions and show that the detection limit of the impact angle of the ions is even better than 1°. Due to the high sensitivity of the impact angle detection, the method is suitable for an ion direction detector.

Figure 6.33: Secondary electron image showing four areas sputtered by a 30 keV Ga ion beam under an incident angle of: (a) $\varphi = -26°/\phi = 0.75°$, (b) $\varphi = 11°/\phi = 0.8°$, (c) $\varphi = -18°/\phi = 1.3°$, (d) $\varphi = 8°/\phi = 1.3°$. The circles symbolize directions of the incident ion beam with rotation φ, while the radii indicate the tilt angles ϕ of the incident ion beam with respect to the sample surface.
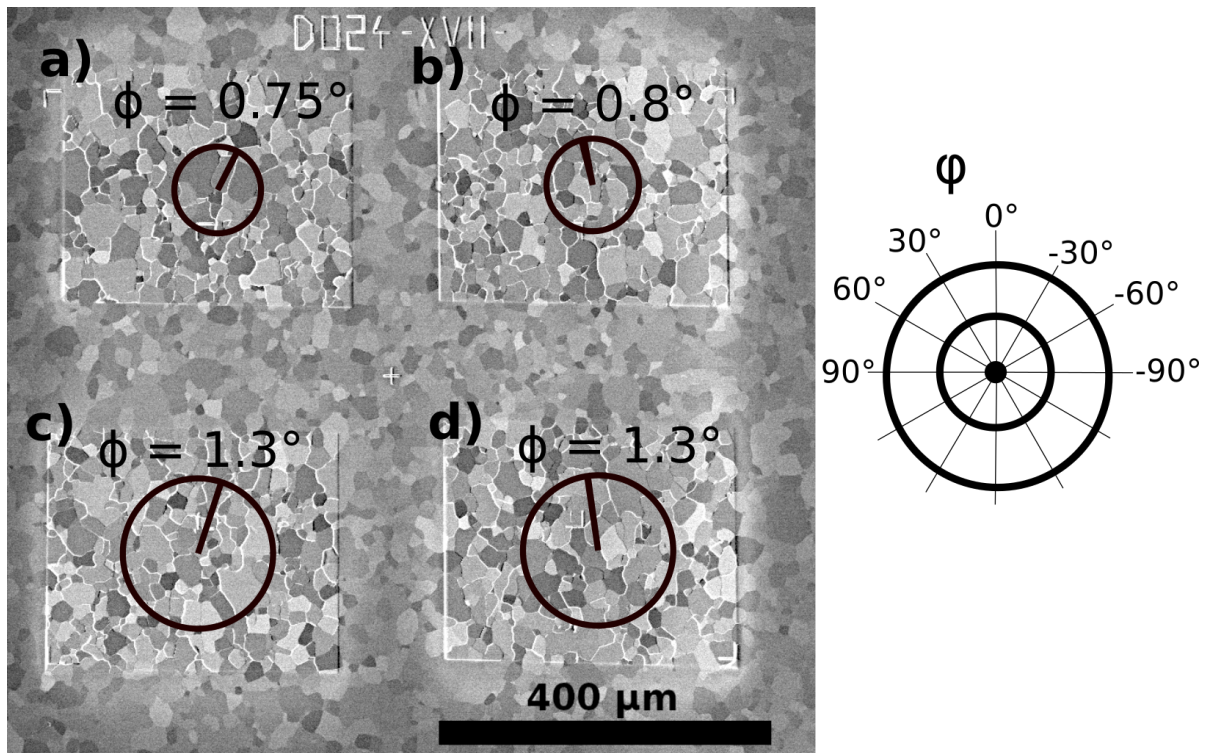
6.5 Correlated properties of sputtering with Ga ions

Two additional properties, secondary electron emission and gallium implantation, were investigated in this section for the main sputter experiment, namely sputtering with a 30 keV Ga ion beam. It is expected and known that these properties correlate with the sputter yield[49,112,113].

The secondary electron emission is a surface process. If the deposited ion energy at the surface was higher, more secondary electrons would be emitted. Therefore, the secondary electron emission was investigated.

Beside sputtering, the ions could be reflected or implanted. Reflection of ions is typical for light ions, e.g. hydrogen (H) and D, and implanted ions penetrate the crystal lattice and come to rest. Therefore, the gallium implantation was investigated with EDX and evaluated to the crystal orientation. In addition, FIB prepared cross-sections were performed to deduce the implantation depth.

Both properties were correlated with the sputter yields. First the tungsten sample was sputtered with a 30 keV Ga ion beam. This cleans the surface from potential impurities. Afterwards the investigations were performed on the sputtered area.

6.5.1 Secondary electron emission

A SEM has several electron detectors to generate different gray scale images for pronouncing material properties or to evaluate the structure of the material. One detector is called Everhart-Thornley detector, which is a SE detector[114]. Normally, a SEM scans with an electron beam, but a FIB-SEM can also scan with an ion beam over the selected sample area and detect the SE[115]. The image of the emitted SE induced by the Ga ion beam is shown in figure 6.34(a) with an overlay image of the crystal orientations. The contrast data was evaluated and visualized as an IPF, which is shown in figure 6.34(b). The Everhart-Thornley-detector was not calibrated to the absolute amount of SE. Therefore, only the differences in the SE emission yield between many crystal orientations can be evaluated.
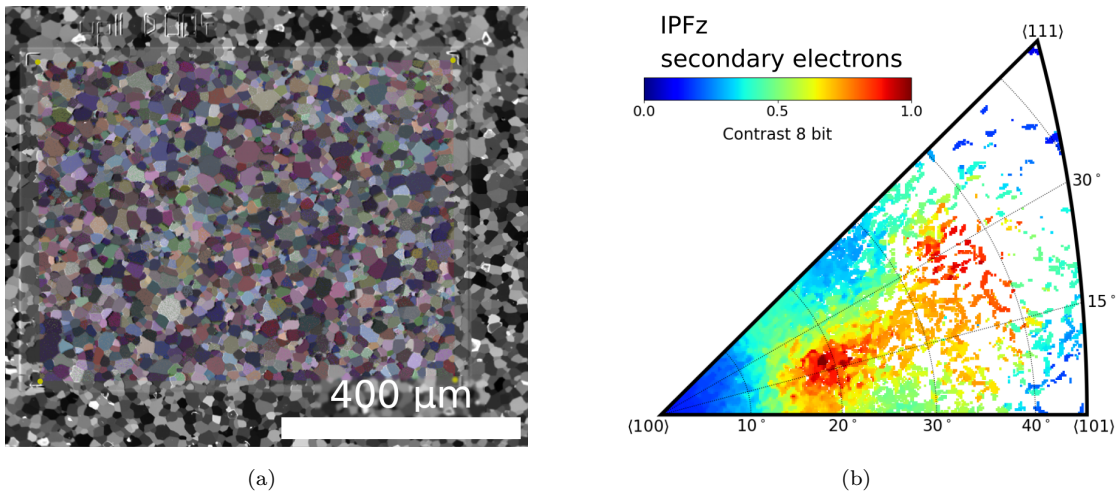
Figure 6.34: (a) An overlay of SE image induced by a 30 keV Ga ion beam and EBSD image of a polycrystalline tungsten surface. (b) SE emission versus crystal orientations. The amount of secondary electrons was deduced from the gray scale of a SE image.

There are several different processes to generate secondary electrons like thermal, potential, or kinetic electron emission. Also, by sputtering tungsten atoms, SEs are emitted. From literature it is known, "when ions are aligned obliquely to a low index crystallographic plane, the ions are stopped closer to the surface, resulting in a larger sputter yield and higher secondary electron yield. Thus, ion channeling directly influences the imaging signal and relative contrast between different grain orientations"[115]. In other words, a FIB ion beam can be used to detect the channeling in the grains of a sample.

The distribution of the SE emission versus the crystal orientation were in agreement with the distribution of the sputter yields. To illustrate this agreement the SE emissions and the sputter yields of figure 6.30 were correlated for each crystal orientation. Each evaluated crystal orientation with less than 50 data points was excluded to get reliable values (see section A.1 or 4.2). The result is shown in figure 6.35.

In principle the Everhart-Thornley detector signal should be proportional to the amount of SEs, because it is based on a scintillation counter. Therefore, the data in figure 6.35 shows that the sputter yield is linear to the SE emission. This plot includes 2654 evaluated data points and has a few outliers. The spread of the data points is probably due to the misalignment angle. By using the not-optimized sputter yields of figure 6.12(a) the spread of the data in figure 6.35 was much larger.
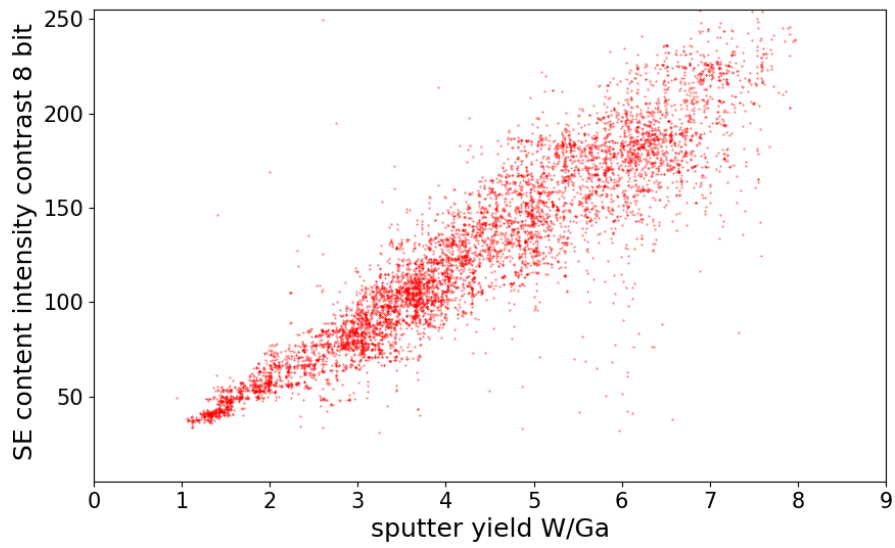
Figure 6.35: Correlations between secondary electron emission intensity and sputter yields.

The linear dependency is also found by others[112,113]. The improvement here is the strongly increased amount of data points.

6.5.2 Gallium implantation

Sputtering and the SE emission depend on the channeling condition of the crystal lattice. If an ion channels into a crystal lattice, it will remain inside the lattice. Therefore, EDX measurements were performed on the sputtered areas.

The focus was to detect the implanted Ga near the surface. In a first trial, EDX measurements were tested with a 20 keV and 5 keV electron beam. The 5 keV electron beam showed better results, which actually means that the differences are bigger between maximum and minimum of the amount of Ga of various grains. This is reasonable, because a 20 keV electron beam has an excitation depth in tungsten of around 200 nm and the implanted Ga atoms were closer to the tungsten surface. With a 5 keV electron beam, an intensity image of the EDX analysis is shown in figure 6.36 (a), which is used to correlate the intensity of the Ga amount to the crystal orientation.

The Ga distribution into the depth was different for each crystal orientation, also the penetration depth of the electron beam was different for various tungsten grains. A quantification of the EDX spectra would give the approximate Ga content. Therefore, only the intensity map was evaluated with a 5 keV electron beam for 'all' crystal orientations. In addition, two grains were selected to estimate the order of the Ga content. The highest amount of Ga is around 20 at% and the lowest amount of Ga is below 2 at%, as shown in figure 6.36. The crystal-dependent Ga EDX intensity distribution is shown in figure 6.36 (b) as an IPF.
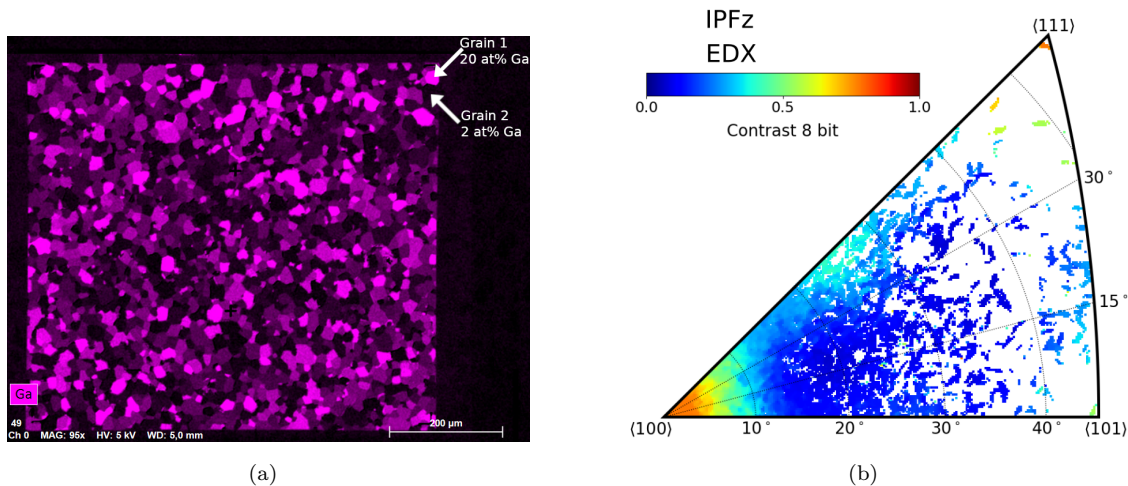
Figure 6.36: (a) EDX intensity map showing the concentration of Ga atoms implanted during sputtering of a polycrystalline tungsten with a 30 keV Ga ion beam. Tungsten grains with strong EDX intensities appear to be bright, indicating a high concentration of implanted Ga atoms. The white arrows indicate two grains where the Ga content was evaluated. (b) Intensities of EDX signal versus crystal orientations.

The distribution of the Ga anti-correlates with the evaluated sputter yields of figure 6.30. The grains with a low sputter yield have a high amount of Ga. The relation between the EDX intensity of Ga and the sputter yield is exponential, which is shown in figure 6.37.
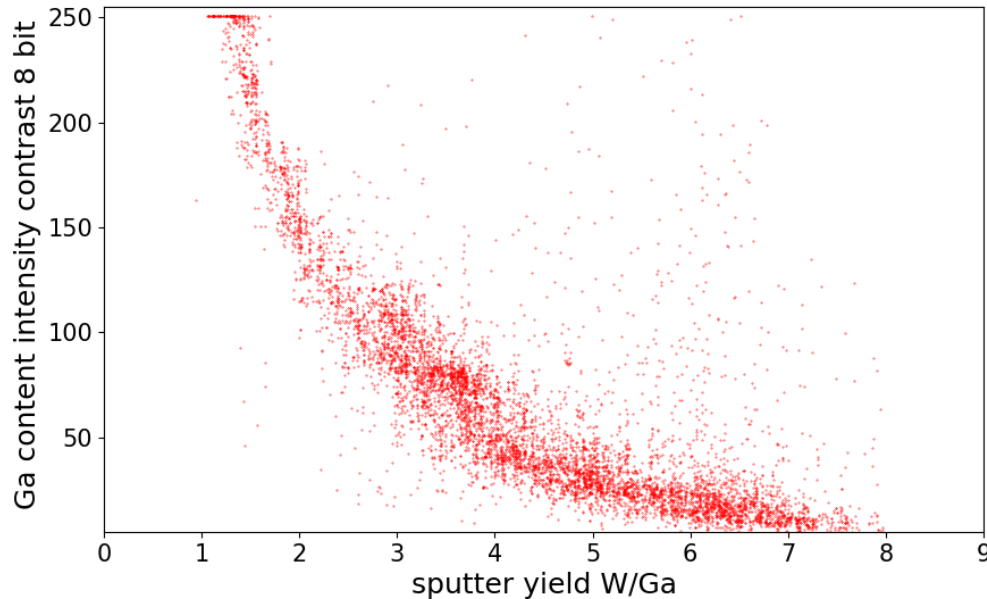
Figure 6.37: Implanted Ga intensities versus sputter yields for tungsten grains. Note that implanted Ga content intensities were evaluated from a 8-bit image (figure 6.36).

To verify the Ga content in the surface, two grains were selected with a high amount of Ga and a low amount of Ga, which are marked in figure 6.36 (a) with grain 1 and grain 2. The surface EDX quantification shows that grain 1 has around $20\,\mathrm{at\%}$ and grain 2 has around $2\,\mathrm{at\%}$ Ga.

For a cross-section, two grains are necessary, because the influence of the Ga ion beam, which was used for the cross-section, must be excluded. First, a Pt-C coating was deposited with an electron beam to protect the surfaces of the grains. Thereafter, a cross-section was produced with a $30\,\mathrm{keV}$ Ga ion beam. The cross-section is shown in figure 6.38 (a). The grain 1 and 2 are marked inside the image. On top, the Pt-C cover is visible. In figure 6.38 (b) the EDX map is shown. Grain 2 has a low amount of Ga at the tungsten surface, which means that the Ga ion beam does not have a significant effect on the cross-section preparation. Therefore, the Ga amount of grain 1 stressing from the FIB cutting was negligible. Grain 1 had around $20\,\mathrm{at\%}$ Ga in the first $50\,\mathrm{nm}$ of the tungsten surface as can be deduced from the green area in the EDX map and the line scan (6.38(c)).

(a)

(b)

(c)
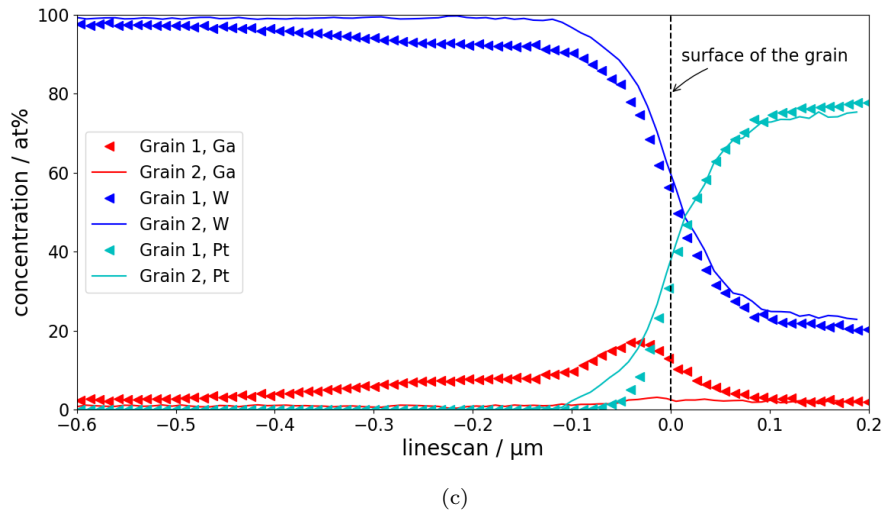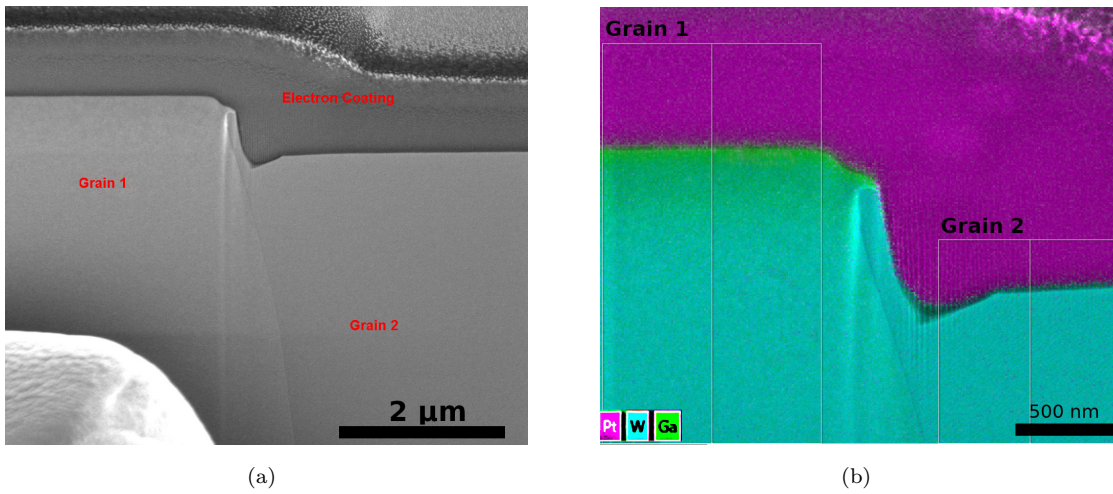
Figure 6.38: EDX analysis with a 5 keV electron beam of a cross-section comprised of two adjacent tungsten grains sputtered by a 30 keV Ga ion beam: (a) SE image of the cross-section. Surface view of the two adjacent tungsten grains can be seen in figure 6.36, as indicated by the white arrows. A Pt-C layer was deposited onto the surface using electron beam prior to cross-section preparation by FIB; (b) elemental mapping of the cross-section; (c) elemental line scanning of the two tungsten grains. The two areas of the scanned lines are marked by white lines in (b). Surfaces of the two tungsten grains are normalized to x=0, as indicated by the dashed perpendicular line. Note that the cross-section and EDX analysis were made 1.5 years after the sputter experiment. Grains 1 and 2 have $\langle 100 \rangle$ and $\langle 216 \rangle$ orientations, respectively.

To visualize the Ga content in grain 1 and 2, two line scans were evaluated. A line scan is a selected area and plotted in one dimension, which is the implantation depth. The selected areas for the line scans are marked with white lines in figure 6.38 (b). The line scan is shown in figure 6.38 (c). The length scale of the x axis was adjusted to 0 at the tungsten surface. Grain 1 has a crystal orientation of $\langle 100 \rangle$,

92

which is a channeling direction. Therefore, Ga channels around $400\,\text{nm}$ into the crystal lattice. The investigation of the cross-section was performed 1.5 years after the sputter experiment. Therefore, the question came up if the Ga could diffuse out or into the crystal lattice at room temperature during the 1.5 years.

(a)   (b)
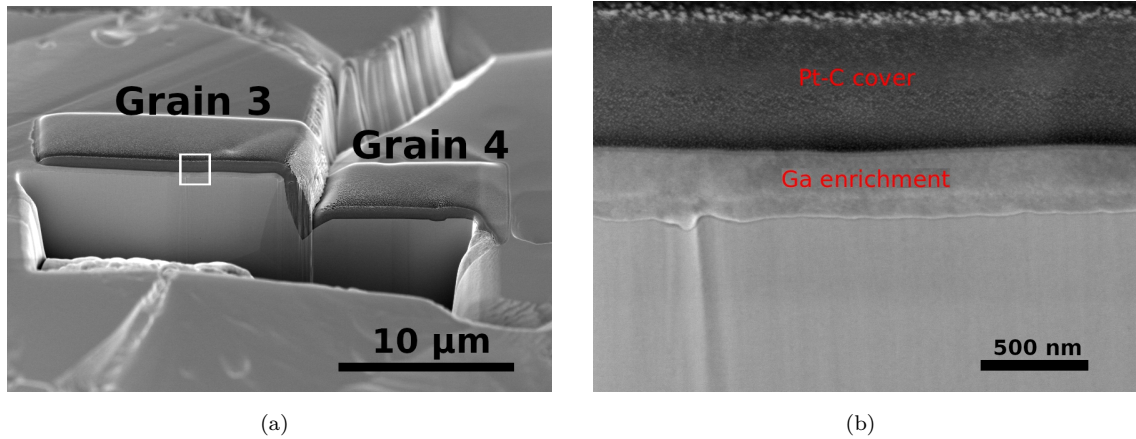
Figure 6.39: SEM images showing the enrichment of implanted Ga atoms at the tungsten grain surface: (a) a low magnification SEM image showing an overview of the cross-section comprising two adjacent tungsten grains, (b) a high magnification SEM image showing the microstructure details of the cross-section of tungsten grain 3. EDS analysis shown in figure A.10 in the appendix indicates that the layer between Pt-C coating and tungsten grain 3 contains a high concentration of implanted Ga atoms. Note that tungsten grain 3 has a $\langle 111 \rangle$ crystal orientation.

To exclude diffusion, a second experiment was performed. This time, the sputter experiment and the EDX analysis were performed on the same day. A polycrystalline tungsten sample was sputtered with a $30\,\text{keV}$ Ga ion beam and afterwards a surface EDX was performed for two selected grains with a high and low amount of Ga. The two selected grains are shown in figure 6.39 (a). The EDX line scans for grain 3 and 4 are shown in the appendix in figure A.10. The EDX line scans of the two analysis are similar. It is interesting that the Ga enrichment zone in grain 3 is visible with an unexpected sharp edge in the SE contrast, which is shown in figure 6.39 (b).

A comparison of the Ga enrichment zone of grain 1 and grain 3 is presented in figure 6.40. Both grains fulfill the channeling condition. But the grain 3 has a $\langle 111 \rangle$ crystal orientation and grain 1 has a $\langle 100 \rangle$ crystal orientation. This makes a direct comparison in figure 6.40 questionable.

At least, a strong diffusion of Ga can be excluded. Also for the $\langle 111 \rangle$ crystal orientation, a $30\,\text{keV}$ Ga ion beam can channel around $350\,\text{nm}$ into the tungsten grain. Interestingly, the plateau of the Ga content in grain 3 is around $150\,\text{nm}$ below the surface. This plateau is not so strongly pronounced in grain 1 which could be due to the diffusion.

Overall, the cross-section EDX analyses confirmed the surface EDX analyses in figure 6.36 and the maximum concentration of Ga is around $20\,at\%$ whereas the lowest amount of Ga is below $1\,at\%$.
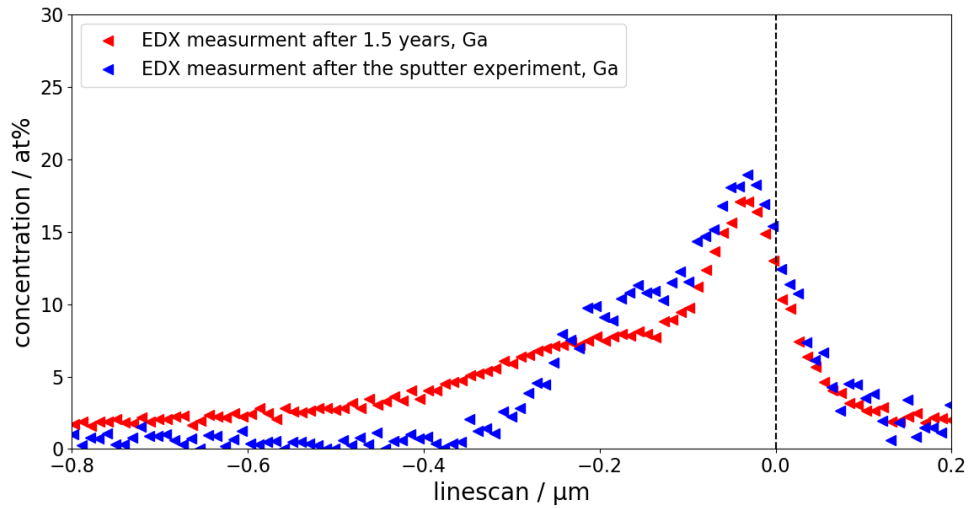
Figure 6.40: Elemental line scanning analysis of the cross-section of tungsten grains with $\langle 100 \rangle$ and $\langle 111 \rangle$ crystal orientations: a comparison of implanted Ga atom concentrations. The EDX surface analysis was the criterion for the selection of the grains. Note, the EDX analysis of tungsten grain with $\langle 100 \rangle$ orientation was made 1.5 years after the sputter experiment, while for tungsten grain with $\langle 111 \rangle$ orientation, the Ga concentration was analyzed directly after the sputter experiment. Tungsten surface is located at x=0 for both cases.

6.6 Deuterium Sputtering

Deuterium sputtering was performed with two different materials. One material was the standard polycrystalline bulk tungsten material, the second one was the W-heavy alloy HPM1850[116,117,118].

HPM1850 is a tungsten base material with $1\,w\%$ Fe and $2\,w\%$ Ni. Both materials were sputtered with the linear plasma device SIESTA[104] at IPP. Afterwards EBSD measurements were performed and the samples were analyzed with CLSM.

6.6.1 Tungsten

The polycrystalline tungsten sample was sputtered with $2\,keV$ D ions over 3 working days to reach a mean erosion depth around $500\,nm$. This resulted in a fluence of $6.44 \times 10^{24}\,at/m^2$.

For getting the absolute erosion depth, markers were deposited to cover several tungsten grains and to protect them against erosion. Unfortunately as shown in figure 6.41, all markers disappeared. But the grain dependent sputtering is well visible.
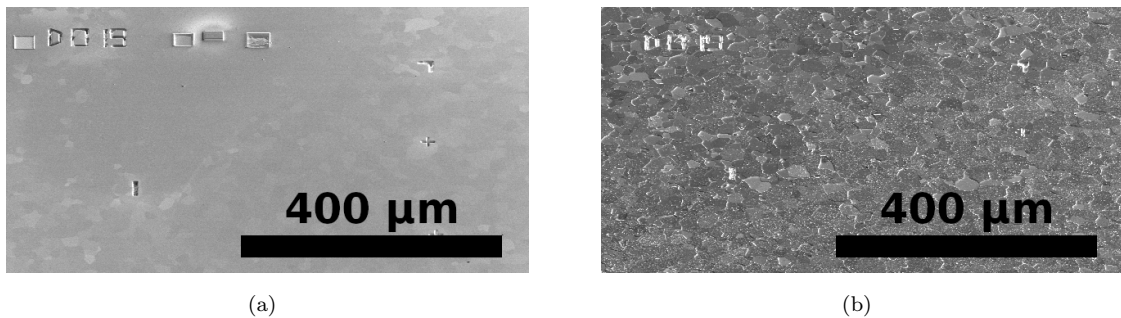
Figure 6.41: SEM images of tungsten showing the surface microstructure before (a) and after (b) the sputter experiment. Note that the deposited Pt-C layers next to the FIB labeled specimen name disappeared in (b).

Therefore, the leveling of the height data was based on SIESTA experiments, in which the sputter yield of such samples was measured due to mass loss. In addition a second check was performed. The second sputter yield investigation with HPM1850 as target had an advanced marker preparation, which persisted under D ion bombardment. The FIB prepared cross-section on the HPM sample (see figure 6.44) confirms the absolute tungsten erosion of around $100\,nm$ at the $\langle 100 \rangle$ crystal orientation. With these information the erosion depth versus the crystal orientation was evaluated, which is shown in figure 6.42(a). The corresponding sputter yields are shown in the appendix in figure A.11.
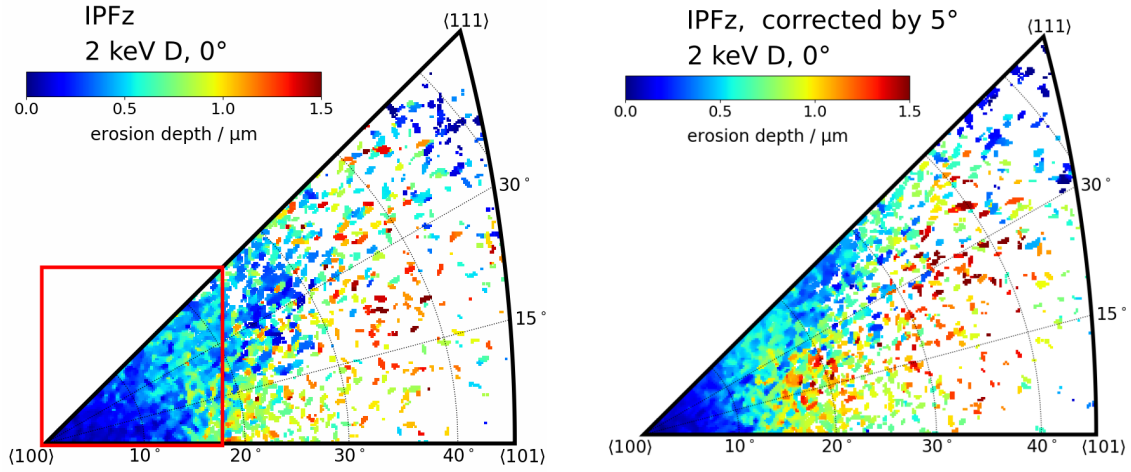
(a) IPFz with erosion depths of tungsten after 2 keV D irradiation. The distribution is blurry due to a misalignment.

(b) IPFz with erosion depths of tungsten after 2 keV D irradiation. The crystal orientations were evaluated to the direction of the ion beam. The direction of the ion beam was evaluated with PCA (see (d)). The sputter yields and the number of measurements are shown in the appendix in figure A.11.
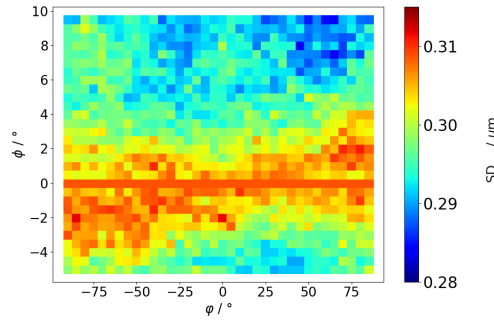
(c) Optimization of all data values with PCA. The SD_{PCA}s of the measurements of the IPF are shown for different misalignment angles ($\phi = 0$ and $\varphi = 0$ was the SD_{PCA} of the values in (a)). The crystals were twisted in ϕ and φ, which results in a different SD_{PCA} for the IPF. No impact angle could be identified, because of the white areas in (a) (to less detected crystal orientations).
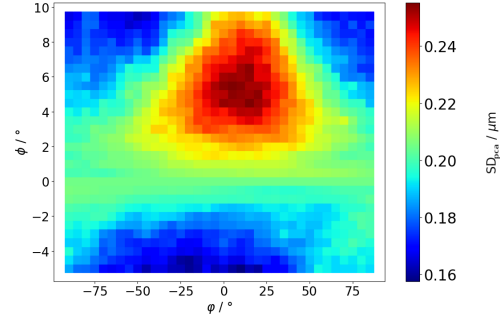
(d) Optimization of selected data points with PCA. The SD_{PCA}s are shown of the measurements inside the red rectangle in (a). The crystals were twisted in ϕ and φ, which results in a different SD_{PCA}. The coordinate $\varphi_{max} = 12°$ and $\phi_{max} = 5°$ shows the highest SD_{PCA}, which actually shows the direction of the ion beam to the surface normal.

Figure 6.42: Crystal orientation dependent erosion behavior of a polycrystalline tungsten after sputtering with a 2 keV D ion beam: (a) erosion depths versus crystal orientations, the crystal orientations were evaluated with respect to the surface normal; (b) erosion depths versus crystal orientations, the crystal orientations were evaluated with respect to the direction of incident ion beam; (c) and (d) standard deviations of the optimization of two Euler angles.

First, the erosion data in figure 6.42(a) was not well understood, because high sputter yields were visible at the boundaries of the triangle and the distribution seemed to be different compared to the Ga sputter experiments (see figure 6.12). After angle-dependent sputter experiments with Ga, the reason became clear, because as shown in section 6.4.3 the developed method is strongly sensitive to the impact angle of the ions. The device SIESTA had a misalignment due to the sample mounting and ion optics, which is around 5°.

After the impact angle detection method was developed, it was used to optimize the data. As realized in section 6.4.2, the PCA was performed with the data of the whole IPF in figure 6.42(a) and the PCA failed as shown in figure 6.42(c), because many crystal orientations were not found on the sample, as can be identified by the white areas in the IPF.

Therefore, the PCA was applied on a smaller region of the IPF marked with a red rectangle in figure 6.42(a). The result of the SD_{PCA} from the PCA evaluation is shown in figure 6.42(d), which shows the impact angle of the ion, ion optics or the misalignment error due to sample mounting.

After correcting this error, strongly eroded grains were not anymore at the boundaries of the IPF, which is shown in figure 6.42(b). The higher erosion appears closer to the center of the IPF, where the high index surfaces are located. This is in agreement with the experiments of a 30 keV Ga ion beam. Therefore, the distribution of the erosion looks similar to that of Ga which means the low index surfaces have low sputter yields and the high index surfaces have high sputter yields. This was expected for 2 keV D from Ga sputter experiments and simulations[109].

6.6.2 HPM1850

HPM1850 is a W-heavy alloy produced by the company H.C.Starck[116]. It is a sintered material and is composed of tungsten with $1\,w\%$ Fe and $2\,w\%$ Ni and has a density of $18.5\,mg/mL$. Therefore, it has a homogeneous texture as demonstrated in the appendix in figure A.13. This means that the crystal orientation of the tungsten grains is randomly distributed and the sample does not contain a preferred crystal orientation as the tungsten samples used for the investigation in the previous sections.

The Fe and Ni act as a sintering add-on as a kind of glue between the tungsten grains, which is visible in figure 6.44 (a) (the black area surrounding the tungsten grains). The Fe/Ni phase between the grains required a changed polishing procedure and the surface was in general rougher than for tungsten. Electropolishing was not anymore possible, therefore the sample was only mechanically polished. After polishing, height differences of around $500\,nm$ between the grains were detected. Therefore, the same areas were analyzed before and after the sputter experiment with CLSM to allow difference microscopy.

As a side topic, heights of the polished surface were correlated to the crystal orientation to study crystal-dependent polishing. The evaluation after polishing is shown in figure 6.43. The crystal orientation $\langle 111 \rangle$ and $\langle 110 \rangle$ show a higher erosion rate compared to the $\langle 100 \rangle$ crystal surface orientation.
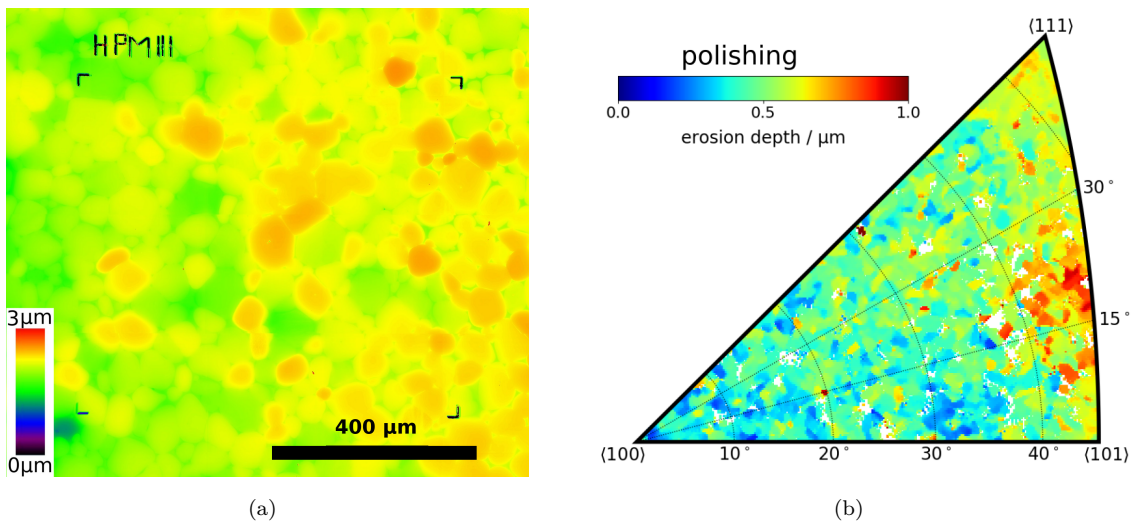
Figure 6.43: Influence of crystal orientations on the mechanically polishing of HPM1850: (a) height profile map derived by CLSM, (b) height profile map visualized in an IPF.

This study was not performed systematically. In order to draw conclusions for crystal

dependent polishing, the experiment needs to be repeated. However, it is clear from this single observation that crystal orientation dependent polishing would influence the evaluation of the sputter experiments. Therefore, difference microscopy was implemented into the Python tool and used during the evaluation of the sputter experiment. This means that the heights measured before and after the sputter experiments were subtracted eliminating the influence of the polishing.

Due to the experience of D sputtering on tungsten, shown in figure 6.41, a Pt-C cover was deposited with an advanced preparation. First 5 holes were prepared with the Ga ion gun (figure 6.41(a)) and afterwards a Pt-C cover was deposited over these holes (figure 6.41(b)). The holes should provide a stronger adhesion of the deposit layer.

(a)   (b)   (c)
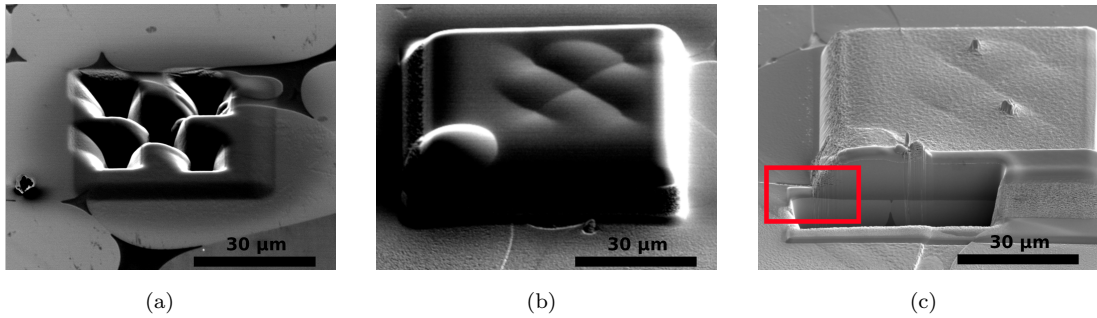
Figure 6.44: SEM images showing an advanced technique to evaluate the absolute depths of erosion induced by sputtering: (a) holes preparation by Ga ion gun. The bright and dark contrasts of the substrate are W and Fe/Ni phases, respectively; (b) deposition of a Pt-C layer over the prepared holes; (c) redeposition of a thin Pt-C layer and cross-section prepared after sputtering the sample surface with 2 keV D ions.

After the Pt-C cover was deposited, the sample was sputtered with 2 keV D ions in SIESTA. The fluence was a little bit lower as for the tungsten sample with $3.7 \times 10^{24} \, \text{at/m}^2$. As already mentioned, during the evaluation the polishing roughness was taken into account by difference microscopy. The erosion depth versus crystal orientation is shown in figure 6.45(a).

Since HPM1850 has a homogeneous texture, the IPF is evenly populated and the PCA was performed over the whole date set. The misalignment through sample mounting was around 6°, which is comparable with the evaluation of tungsten. The result of the PCA analysis is shown in figure 6.45(c). The corrected IPF is shown in figure 6.45(b). The result is similar as for tungsten. All highly eroded grains at the boundaries of the IPF moved to the center of the IPF as it was expected. The channeling crystal orientations had a low sputter yield and the high index surfaces had a high sputter yield, which is similar to a 30 keV Ga ion beam (see figure 6.30).
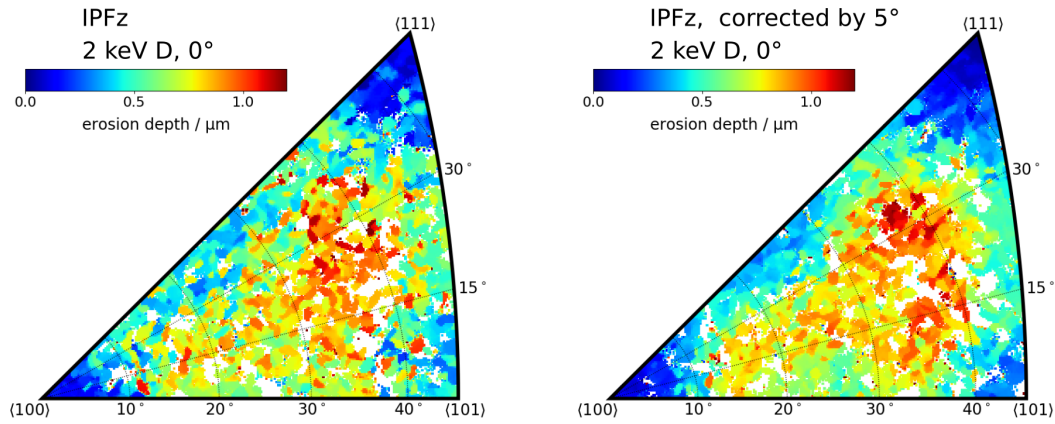
(a) IPFz with erosion depths of HPM1850 after 2 keV D irradiation. The crystal orientations were evaluated to the surface normal.

(b) IPFz with erosion depths of HPM1850 after 2 keV D irradiation. The crystal orientations were evaluated to the direction of the ion beam. The direction of the ion beam was evaluated with PCA (see (c)). The values of the erosion as well as the SD_{PCA} and the number of measurements are shown in the appendix in figure A.12.
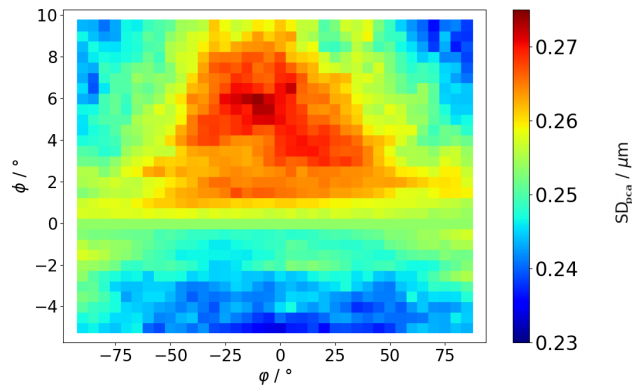
(c) Optimization of the measurements with PCA. The SD_{PCA}s of the erosion values in the IPF are shown for different misalignment angles ($\phi = 0$ and $\varphi = 0$ was the SD_{PCA} of the values in (a)). The crystals were twisted in ϕ and φ, which results in a different SD_{PCA} for the IPF. The coordinate $\varphi_{max} = -10°$ and $\phi_{max} = 5°$ shows the highest SD_{PCA}, which actually shows the direction of the ion beam to the surface normal.

Figure 6.45: Crystal orientation dependent erosion behavior of HPM1850 after sputtering with a 2 keV D ion beam: (a) and (b) erosion depths versus crystal orientations in an IPF. The crystal orientations in (a) and (b) were evaluated with respect to the surface normal and the direction of the ion beam, respectively; (c) the change of standard deviations with the two impact angles. The standard deviation at $\phi = 0$ and $\varphi = 0$ corresponds to the case shown in (a). The standard deviation peak appears at $\varphi = -10°$ and $\phi = 6°$, which actually indicates the direction of the ion beam with respect to the surface normal.

The results show that the method to evaluate thousands of different sputter yields in various crystal orientations works for different sputtering particles and particle sources. The evaluation process and the experimental set up is more complicated than making the crystal orientation measurements and the sputter experiment in one device (focused ion beam scanning electron microscope (FIB-SEM)). The amount of data by sputtering with the device SIESTA could be increased easily in future experiments, because the sputtered area is not limited to around $1\,\mathrm{mm}^2$ as it was by the FIB.

6.7 Summary and discussion for sputtering results

Crystal-dependent sputter yields were evaluated for different flux densities, different fluences (Ga: $0.5 \times 10^{22} - 4.3 \times 10^{22}$ atoms/m^2, D: $3 \times 10^{24} - 6.5 \times 10^{24}$ atoms/m^2), different energies (2 keV, 8 keV and 30 keV) and different impact angles (0°, 5°, 20° and 60°) and compared with simulations. In general, the experimental data are in very good agreement with molecular dynamic simulations and SDTrimSP simulations for the average sputter yield. The molecular dynamic simulations were based on the energy impact in the first two nm of the surface, which confirms the common sputter theories[36,39,46].

For a 2 keV Ga ion the differences of the crystal-dependent sputter yields were a factor of two, whereas for 30 keV Ga ion beam the sputter yields were a factor of eight different. In general, for higher energies of Ga ions the crystal-dependency of the sputter yields is stronger. In addition for low energies around 2 keV, the used FIB-SEM showed an influence of the flux density. A possible explanation is the influence of the residual gas in the vacuum chamber. As figure 6.18 shows, the sputter yields increase for higher energies at the high index surfaces whereas the lowest evaluated sputter yields, which were measured at the low index surfaces, remain nearly the same for different energies ($2 - 30$ keV Ga ions). Specially for a 30 keV Ga ion beam, the sputter yield on tungsten changed continuously with the crystal orientation, and there is no region of crystal directions that would behave like amorphous material. This could be due to linear collision sequences, which can only occur in a crystalline material[49].

Due to the huge amount of experimental data, filter techniques and new analysis methods could be applied on crystal-dependent sputter data. This included the optimization of the data due to the impact angle of the ions, as shown in figure 6.29. This newly developed technique was also used to detect the impact angle of the ions. The accuracy of this impact angle detection is far better than 1° as shown in figure 6.33. It is shown that this impact angle detection and the following correction of the data are necessary for the plasma device SIESTA, because the sample mounting on different devices was hardly better than 1° and the evaluation was sensitive to the impact angle. Sputtering with D ions showed a misalignment of 5°. This was measured for 2 keV D ions. Experiments showed that for lower energies, e.g. 200 eV[105], the ions had an impact angle of around 20°, which is not anymore negligible. This knowledge was not available in[105]. Therefore, figure 12 in[105] was reevaluated and presented in the appendix in figure A.14, which yields in a significant change of the interpretation of the sputter yield data.

The angle-dependent sputter experiments showed that the impact angle can be evaluated by PCA or by minimizing the error between the measurements. The accuracy of both methods was better than 1°. The preferred detection method depends on the data set and on the experiment. With rotation matrix multiplications, the crystal-

dependent sputter yields were evaluated as an IPF in direction to the ion beam. The angle-dependent sputter experiment showed that the sputter yield increased at the low and high index surfaces (see figure 6.18), whereas for energy dependency, the sputter yields increased mainly at the low index surfaces (see figure 6.23). In addition, the sputter yield distribution in the IPF changes with the crystal orientation for different impact angles, as shown in figure 6.24. For a 30 keV Ga ion beam, specially at the high index surfaces, more crystal orientations had the highest sputter yield for sputtering under 60° compared to sputtering under 0°. The total sputter yield was influenced by the change of the sputter yield distribution and it showed that angle-dependent sputter yield could not simply be described by a $\cos(\phi)$ function, which is often done[28]. Probably for angle dependent sputtering, the change of the sputter yield distribution in the IPF is due to linear collision sequences, and in some crystal orientations, the probability is maybe higher so that a linear collision sequence occurs under a higher impact angle.

In addition to the sputter yield, the secondary electron emission, caused by the 30 keV Ga FIB, was measured with the secondary electron detector of the microscope. The distribution of the secondary electron yield versus the crystal orientation matches the experimental sputter yields very well. It was demonstrated that secondary electron emission has a linear dependency on the sputter yield (see figure 6.35).

Also, the Ga implantation due to the crystal orientation was investigated for a sputtered surface by the 30 keV Ga FIB. The resulting IPF showed high Ga contents around low-index crystallographic directions where the projected range is large[49] and the sputter yield small. This was expected, since both features make it more difficult to remove the implanted ions from the target. For a detailed investigation of the depth distribution of the channeled Ga ions, FIB prepared cross-sections were made on low and high index surfaces for comparing them and verifying the Ga content with EDX. At the low index surfaces ($\langle 100 \rangle$ and $\langle 111 \rangle$), the Ga content was around 20 at% at the surface. In contrast, at the high index surfaces, the Ga content was below the detection limit of the EDX. Also, Ga was found down to about 350 nm below the surface in the $\langle 100 \rangle$ and $\langle 111 \rangle$ crystal orientation, whereas SDTrimSP simulation showed a maximum penetration depth of 25 nm and a Ga content of 20 at% for an amorphous W.

7 Crystal-dependent etching of tungsten

Etching is a topic for many applications in industry and science[61,119,120,121]. Specially for silicon, which has a diamond crystal structure, a lot of investigations were performed. The etching rate along different crystal directions varies, e.g for silicon over a factor of 100. This makes it possible to generate the structure in a single crystal with the help of masks on top of the surface[119,122]. Often, these investigations were performed on single crystals. Sometimes the geometry of a sphere was used to etch a single crystal[121,123]. A single crystal sphere provides every crystal orientation on the surface. The developed method in this work is appropriate to investigate crystal-dependent etching on a polycrystalline sample. In the previous sections, oxidation rates, sputter yields, secondary electrons and the implantation of Ga were investigated. To demonstrate the broadness of the developed method, one etching experiment was performed with Murakami solution, which is a mixture of sodium hydroxide and potassium ferricyanide[124].

7.1 Experiment
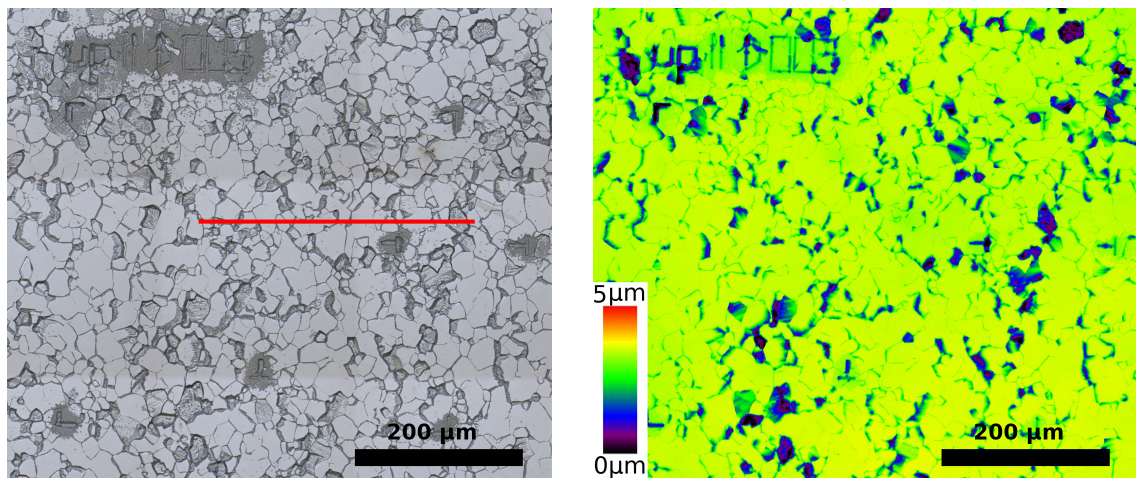
(a) CLSM image is shown after the etching experiment. The red line marks the area of the line scan in figure 7.2

(b) Height profile map with the CLSM after the etching experiment.

Figure 7.1: Crystal orientation dependent etching behavior of tungsten: (a) CLSM image showing the surface microstructure after etching. (b) Height profile map derived by CLSM.

The sample preparation was similar as for sputtering and the oxidation experiment. For the etching experiment, a recrystallized polished polycrystalline tungsten sample was used. The Murakami solution was produced shortly before the tungsten sample was etched. First, a 15 % sodium hydroxide solution and a 15 % potassium

ferricyanide solution were produced. Second, the two solutions were mixed together to get the Murakami solution[124]. The tungsten sample was hold with tweezers into the liquid for 2 min. Afterwards, the sample was cleaned directly with distilled water.
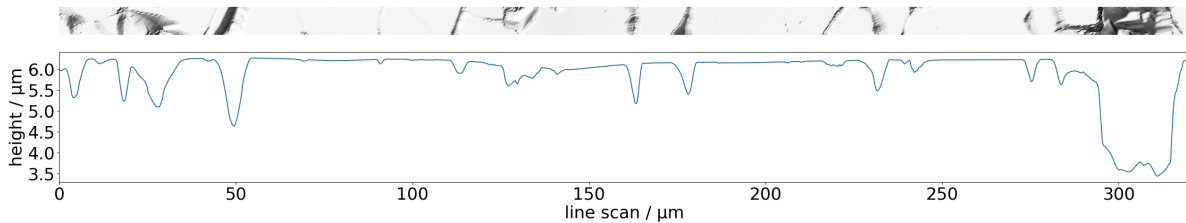
Figure 7.2: Height profile along the red line marked in figure 7.1. The selected area is visualized as an image above the height diagram.

Figure 7.2 shows the height differences and an image of the selected area which is marked as a red line in figure 7.1. The height differences were up to $4\,\mu m$. The reference level, which is the height where no etching appears, is around $6.3\,\mu m$. This is visible because most grains do not show any etching. The heights and the crystal orientation were merged with the python tool described in section 4.2. To get the total etching depth, the reference level was subtracted from the data set.

7.2 Results and discussion

The deduced etching depth versus the crystal orientation is shown in figure 7.3. The $\langle 111 \rangle$ crystal orientation to the surface normal has the strongest erosion. The etching of one single grain was not homogeneous. A line scan in figure 7.2 shows often peaks which increase the SD. Therefore, the SD, which is shown in figure 7.3 (b), is larger compared to oxidation experiments or sputter experiments. In the line scan, only one grain eroded over the full area of the grain at the line scan position $300\,\mu m$. Often, only the grain boundaries show an eroded area. Nevertheless, figure 7.3 shows the distribution of the erosion versus the crystal orientation and it demonstrates that the method is feasible also for etching investigations. The $\langle 110 \rangle$ crystal orientation in a bcc lattice has the closest packed surface of atoms, but does not have the lowest etching rate (see figure 5.11). Since most grains do not show any erosion, the differences in the etching rate due to the crystal orientation is huge and different by several orders of magnitudes.

106
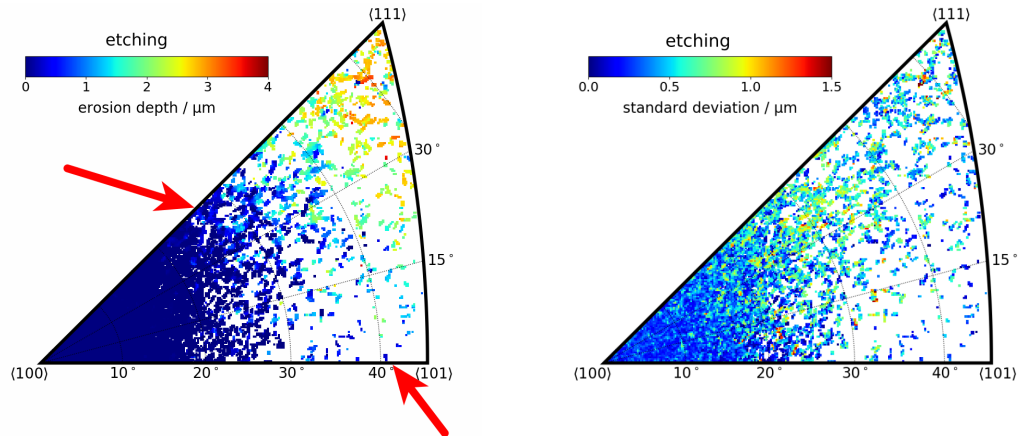
(a) Erosion versus the crystal orientation is shown. The red arrows point to the positions where the tensile Schmid factors are equal to the compressive Schmid factors (see figure 7.4).

(b) Standard deviation is shown of the measurement in (a). The SD is larger than for sputter or oxidation experiments.

Figure 7.3: Evaluation of crystal orientation dependent etching behavior of a recrystallized tungsten sample: (a) erosion depth versus crystal orientation in an IPF. (b) standard deviation for the evaluation of erosion depth. The sample was etched in the Murakami solution for 2 min.

An explanation to the etching depths distribution in the IPF could be the relationship between the compressive and tensile stress in a bcc lattice. Gall and Sehitoglu[125] compared the compressive and tensile stress for TiNi, which has a bcc lattice. Mao et. al.[126] extended the studies and calculated the Schmid-factors for an IPF with the experimentally observed shearing systems in[127]. The tensile (S_{max}^T) and compressive Schmid factors (S_{max}^C) of their studies are presented in figure 7.4. If the S_{max}^T is bigger than S_{max}^C of the bcc lattice, the tungsten surface will be etched, which is marked with red arrows in figure 7.3 (a). The correlation between etching rate and Schmid factor should be tested with other materials or etching solutions to generate a reliable data set to develop perhaps a theory or an approximation of the underlying process.

In figure 7.3, there are a lot of crystal orientations, where the etching rate is not determined. Therefore, additional experiments are required with tungsten and the Murakami solution to evaluate the etching rate in "every" crystal orientation. Already a higher data amount, specially at the ⟨110⟩ orientation, could show a better correlation between the Schmid factors (S_{max}^T vs. S_{max}^C) and the etching behavior.

Another correlation of the etching rate was found due to the recrystallization process. Recrystallization is a process which reduces the internal energy of the system. Energetically unfavourable structure, like crystal defects and probably special crystal surface orientations will be reduced during the process. As shown in figure 3.1, the ⟨111⟩ orientation amount decreases during the recrystallization process. This is the same orientation which has the strongest etching rate and is an interesting correlation.
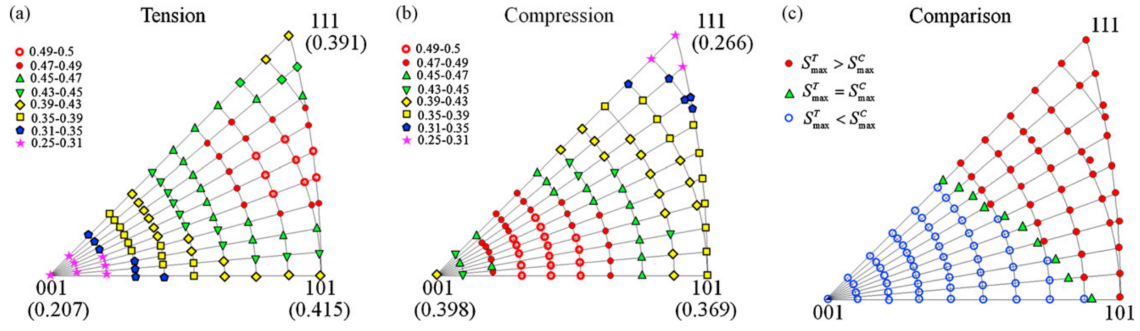
Figure 7.4: The caculated Schmid factor IPF from [126]: (a) for tensile Schmid factor and (b) for compressive Schmid factor. Different symbols represent different values of the Schmid factor. (c) The comparison results of the tensile Schmid factors ($S_{m}ax^{T}$) and compressive Schmid factors (S_{max}^{C}) and a $S_{max}^{T} = S_{max}^{C}$ line is defined in the figure as shown by the green triangles [126].

8 Summary and Outlook

The main goal of this work was to characterize tungsten surface properties with regard to its crystal orientation. The samples were recrystallized to avoid surface defects which could influence the investigations. Also, grain growth was desired to achieve larger single crystal grains for different kinds of experiments. The crystal orientation was measured using EBSD. After performing sputter, oxidation or etching experiments, the CLSM provided height information of thousands of single crystal grains. These data described the investigated properties in 'every' crystal orientation. These huge data sets contain millions of measurements so that a manual merging was not possible anymore.

Therefore, a python tool was developed to correlate the data of different measuring systems using different physical principles. The data provided by these measuring systems had different kinds of forms and also the space coordinate system was different. It turned out that a simple perspective correction of two optical devices was not sufficient for merging the data sets. Ultimately, an affine transformation was used to merge the different space coordinate systems, and therefore the data. Millions of data points were combined with this technique, which makes it reasonable to apply filters to enhance the quality of the final results, even if many high quality data points were lost together with the lower number of unreliable ones.

The python tool was continuously developed during the whole work. This means that the evaluation was extended to different kinds of data sets and that features were implemented, as for example difference microscopy or an impact angle detection algorithm. Finally, the python tool combined and evaluated data which includes crystal orientation data, height data, secondary electron emission data and energy dispersive X-ray spectroscopy data. The investigated properties, such as oxidation, sputtering, and etching, were discussed in detail in section 5.5, 6.7, 7.2, respectively.

As expected, the crystal-dependent surface properties showed significant differences. The oxidation rate of tungsten surfaces differs by a factor of 2 between crystal orientations in a temperature range from 450 °C to 600 °C. The sputter experiments showed higher differences between different crystal orientations. For a 30 keV Ga ion beam as well as for a 2 keV D ion beam, the sputter yields of tungsten differ of around one order of magnitude for different crystal orientations. The strongest dependency on the crystal orientation was found for chemical etching. By etching tungsten with the Murakami solution, the differences of the etching rate due to the crystal orientation were several orders of magnitudes.

The oxidation process is complex and can be subdivided into several steps. For future investigations, the sub-processes such as diffusion of oxygen could be investigated as a function of the crystal orientation. Also, future studies could focus more on tungsten oxide crystals rather than on pure tungsten. This could elucidate the

process in far more detail.

Compared to oxidation, the sputter process is far more understood and therefore, simulations are available. The MD and BCA simulations are in very good agreement with the experiments and allow to study details like the correlation between projected range of ions and the sputter yields[49]. In addition, new techniques could be developed to investigate, e.g. the impact angle detection of high energetic ions. The angle-dependent sputter experiments showed that the impact angle could be evaluated with PCA or with minimization of the error between the measurements. The accuracy of both methods was better than 1°. The appropriate detection method depends on the data set and on the experiment. In addition, even with the accuracy better than 1°, there is still room for improvement. For a known ion target combination, the distribution of the sputter yields could be pre-characterized and the impact detection algorithm could be applied to the known solution. This would extend the impact angle detection method to poor data sets. Such an algorithm would be interesting for sputtering of materials in a plasma device like ASDEX Upgrade, where the impinging plasma will have a distinct angle distribution depending on the ambient magnetic and electrical fields and where different kinds of ions may exist in the plasma.

With a detailed knowledge of crystal-dependent sputtering, also the ion energy, the fluence and probably the ion species could be distinguished for unknown plasma composition if sufficient pre-knowledge of the system is available.

The last investigated property in this work was crystal-dependent etching. The differences in the etching rate are several orders of magnitudes. This huge factor is very interesting and could be used to optimize the life time of components.

In addition, it was observed that the etching data has a strong correlation with the Schmid factor (see figure 7.3 and 7.4). This is an interesting correlation and should be studied in more detail, because it may allow to predict crystal orientation dependent etching rates, respectively the erosion resistance of materials. This would be important for, e.g. battery research, where the degradation of the anode should be avoided[128] or for other chemical applications, where strong chemical surface reactions are desired[129].

In general, the strategy and tools developed in this thesis are suitable to investigate different kinds of properties depending on the crystal orientation, which allow in case of the sputter experiments an unprecedented comparison to mesoscopic theories.

References

[1] G E Fussell. Ploughs and ploughing before 1800. *Agricultural History*, 40(3): 177–186, 1966.

[2] M A White. *Physical properties of materials.* CRC press, 2018.

[3] B Alemour, O Badran, and M R Hassan. A review of using conductive composite materials in solving lightening strike and ice accumulation problems in aviation. *Journal of Aerospace Technology and Management*, 11, 2019.

[4] S Mazumdar. *Composites manufacturing: materials, product, and process engineering.* CRC press, 2001.

[5] S Naik. Basic aspects of gas turbine heat transfer. *Heat Exchangers–Design, Experiment and Simulation*, pages 111–142, 2017.

[6] H Gietl, J Riesch, J W Coenen, T Höschen, Ch Linsmeier, and R Neu. Tensile deformation behavior of tungsten fibre-reinforced tungsten composite specimens in as-fabricated state. *Fusion Engineering and Design*, 124:396–400, 2017.

[7] M Zhao, K Schlueter, M Wurmshuber, M Reitgruber, and D Kiener. Open-cell tungsten nanofoams: Scaling behavior and structural disorder dependence of young's modulus and flow strength. *Materials & Design*, 197:109187, 2020.

[8] R L Davidchack and B B Laird. Crystal structure and interaction dependence of the crystal-melt interfacial free energy. *Physical Review Letters*, 94(8): 086102, 2005.

[9] A L Southern, W R Willis, and M T Robinson. Sputtering experiments with 1-to 5-keV Ar^+ ions. *Journal of Applied Physics*, 34(1):153–163, 1963.

[10] H E Roosendaal. Sputtering yields of single crystalline targets. In *Sputtering by particle bombardment I*, pages 219–256. Springer, 1981.

[11] D E Harrison Jr, P W Kelly, Barbara J Garrison, and N Winograd. Low energy ion impact phenomena on single crystal surfaces. *Surface Science*, 76 (2):311–322, 1978.

[12] G K Wehner. Sputtering of metal single crystals by ion bombardment. *Journal of Applied Physics*, 26(8):1056–1057, 1955.

[13] A Litnovsky, Yu Krasikov, M Rasinski, A Kreter, Ch Linsmeier, Ph Mertens, B Unterberg, U Breuer, and T Wegener. First direct comparative test of single crystal rhodium and molybdenum mirrors for ITER diagnostics. *Fusion Engineering and Design*, 123:674–677, 2017.

[14] M Rusanovsky, R Harel, L Alon, I Mosseri, H Levin, and G Oren. Backus: comprehensive high-performance research software engineering approach for simulations in supercomputing systems. 2019. URL https://arxiv.org/abs/1910.06415.

[15] G E Moore et al. Cramming more components onto integrated circuits, 1965.

[16] J Goulden, P Trimby, and A Bewick. *Microscopy and Microanalysis*, 24(S1): 1128–1129, 2018.

[17] E Lassner and W-D Schubert. The element tungsten. In *Tungsten*, pages 1–59. Springer, 1999.

[18] W Borchardt-Ott. *Kristallographie Eine Einführung für Naturwissenschaftler*. Springer-Verlag Berlin-Heidelberg-New York-London-Paris-Tokyo-Hong Kong, 5 edition, 1997. ISBN 3-540-63044-9.

[19] H J Bunge. The general description on texture. *Z. Metallkunde*, 56:872–874, 1965.

[20] V Randle. *Microtexture determination and its applications.* 2003.

[21] V Randle and O Engler. *Introduction to texture analysis: macrotexture, microtexture and orientation mapping.* CRC press, 2014.

[22] 04.04.2020. URL https://en.wikipedia.org/wiki/Crystal.

[23] E J W Whittaker and C A Taylor. *The stereographic projection.* University College Cardiff Press, 1984.

[24] C Fong et al. An indoor alternative to stereographic spherical panoramas. *Proceedings of Bridges 2014: Mathematics, Music, Art, Architecture, Culture*, pages 103–110, 2014.

[25] W R Grove. XXXIII. On some anomalous cases of electrical decomposition. *The London, Edinburgh, and Dublin Philosophical Magazine and Journal of Science*, 5(31):203–209, 1853.

[26] W R Grove. VII. On the electro-chemical polarity of gases. *Philosophical Transactions of the Royal Society of London*, (142):87–101, 1852.

[27] M Plücker. XLVI. Observations on the electrical discharge through rarefied gases. *The London, Edinburgh, and Dublin Philosophical Magazine and Journal of Science*, 16(109):408–418, 1858.

[28] R Behrisch and W Eckstein. *Sputtering by particle bombardment: experiments and computer calculations from threshold to MeV energies*, volume 110. Springer Science & Business Media, 2007.

[29] G Dearnaley and N E W Hartley. Ion implantation into metals and carbides. *Thin Solid Films*, 54(2):215–232, 1978.

[30] H D Hagstrum. Auger ejection of electrons from tungsten by noble gas ions. *Physical Review*, 104(2):317, 1956.

[31] M L E Oliphant and P B Moon. The liberation of electrons from metal surfaces by positive ions. Part II.—Theoretical. *Proceedings of the Royal Society of London. Series A, Containing Papers of a Mathematical and Physical Character*, 127(805):388–406, 1930.

[32] L A Giannuzzi et al. *Introduction to focused ion beams: instrumentation, theory, techniques and practice.* Springer Science & Business Media, 2004.

[33] A A Correa. Calculating electronic stopping power in materials from first principles. *Computational Materials Science*, 150:291–303, 2018.

[34] J Orloff, M Utlaut, L Swanson, and A Wagner. High resolution focused ion beams: FIB and its applications. *Physics Today*, 57(1):54–55, 2004.

[35] W Möller. Fundamentals of ion-solid interaction. 2013. URL `https://hzdr.qucosa.de/api/qucosa%3A22328/attachment/ATT-0/`.

[36] J Lindhard. *Influence of crystal lattice on motion of energetic charged particles*, volume 34. Munksgaard, 1965.

[37] H Ryssel and H Glawischnig, editors. *Ion Implantation Techniques.* Springer, New York, 1982. ISBN 978-3-642-68779-2.

[38] A Brodyanski, S Blomeier, H Gnaser, W Bock, B Hillebrands, M Kopnarski, and B Reuscher. Interplay of energy dissipation, ion-induced mixing, and crystal structure recovery, and surface effects in ion-irradiated magnetic Fe/Cr/Fe trilayers. *Physical Review B*, 84(21):214106, 2011.

[39] P Sigmund. Theory of sputtering. I. Sputtering yield of amorphous and polycrystalline targets. *Physical Review*, 184(2):383, 1969.

[40] G R Piercy, F Brown, J A Davies, and M McCargo. Experimental evidence for the increase of heavy ion ranges by channeling in crystalline structure. *Physical Review Letters*, 10(9):399, 1963.

[41] H Lutz and R Sizmann. Super ranges of fast ions in copper single crystals. *Phys. Letters*, 5, 1963.

[42] Y Kagan and Y V Kononets. Theory of channeling effect. *Soviet Physics JETP*, 31(1), 1970.

[43] J Bak, G Melchart, E Uggeroj, J S Forster, P R Jensen, H Madsboll, S P Moller, Henry Nielsen, G Petersen, and H Schiott. Bending of high energy beams using axial and planar channeling. *Physics Letters B*, 93(4):505–508, 1980.

[44] W J MoberlyChan, D P Adams, M J Aziz, G Hobler, and T Schenkel. Fundamentals of focused ion beam nanostructural processing: Below, at, and above the surface. *MRS bulletin*, 32(5):424–432, 2007.

[45] 03.04.2020. URL https://de.wikipedia.org/wiki/Gitterführungseffekt.

[46] D Onderdelinden. The influence of channeling on Cu single-crystal sputtering. *Applied Physics Letters*, 8(8):189–190, 1966.

[47] T Nagasaki, H Hirai, M Yoshino, and T Yamada. Crystallographic orientation dependence of the sputtering yields of nickel and copper for 4-keV argon ions determined using polycrystalline targets. *Nuclear Instruments and Methods in Physics Research Section B: Beam Interactions with Materials and Atoms*, 418:34–40, 2018.

[48] B W Kempshall, S M Schwarz, B I Prenitzer, L A Giannuzzi, R B Irwin, and F A Stevie. Ion channeling effects on the focused ion beam milling of Cu. *Journal of Vacuum Science & Technology B: Microelectronics and Nanometer Structures Processing, Measurement, and Phenomena*, 19(3):749–754, 2001.

[49] K Schlueter, K Nordlund, G Hobler, M Balden, F Granberg, O Flinck, T F da Silva, and R Neu. Absence of a crystal direction regime in which sputtering corresponds to amorphous material. *Physical Review Letter*, 125:225502, Nov 2020. doi: 10.1103/PhysRevLett.125.225502. URL https://link.aps.org/doi/10.1103/PhysRevLett.125.225502.

[50] M T Robinson. Basic physics of radiation damage production. *Journal of Nuclear Materials*, 216:1–28, 1994.

[51] P Sigmund. Fundamental processes in sputtering of atoms and molecules. 1993.

[52] P Sigmund. Six decades of atomic collisions in solids. *Nuclear Instruments and Methods in Physics Research Section B: Beam Interactions with Materials and Atoms*, 406:391–412, 2017.

[53] M T Robinson. Theoretical aspects of monocrystal sputtering. In *Sputtering by particle bombardment I*, pages 73–144. Springer, 1981.

[54] M A Kirk, T H Blewitt, and T L Scott. Irradiation disordering of $Ni_3 Mn$ by replacement collision sequences. *Physical Review B*, 15(6):2914, 1977.

[55] D N Seidman, N L Peterson, and S D Harkness. Radiation damage in metals. *American Society for Metals*, page 28, 1976.

[56] K H Ecker. Transmission sputtering of gold by heavy ions in the lower keV energy region. *Radiation Effects*, 23(3):171–180, 1974.

[57] G Ayrault, R S Averback, and D N Seidman. New approach for the study of transmission sputtering. *Scr. Metall.;(United States)*, 12(2), 1978.

[58] W Weil and W Schubert. 03.12.2015. URL `http://www.itia.info/assets/files/newsletters/Newsletter_2013_06.pdf`.

[59] K Schlueter. Dependence of oxidation on the grain orientation of tungsten. 2017. URL `http://hdl.handle.net/11858/00-001M-0000-002C-94A5-8`.

[60] O Lange. Metalloberflächenbehandlung. In *Metalle und Minerale*, pages 25–128. Springer, 1923.

[61] Kenneth E Bean. Anisotropic etching of silicon. *IEEE Transactions on electron devices*, 25(10):1185–1193, 1978.

[62] A Manhard, M Balden, and S Elgeti. Quantitative microstructure and defect density analysis of polycrystalline tungsten reference samples after different heat treatments. *Practical Metallography*, 52(8):437–466, 2015.

[63] R Reichelt. *Scanning Electron Microscopy*, pages 133–272. Springer New York, New York, NY, 2007. ISBN 978-0-387-49762-4. doi: 10.1007/978-0-387-49762-4_3. URL `https://doi.org/10.1007/978-0-387-49762-4_3`.

[64] J I Goldstein, D E Newbury, J R Michael, N W M Ritchie, J H J Scott, and D C Joy. *Scanning electron microscopy and X-ray microanalysis*. Springer, 2008.

[65] S L Flegler, J W Heckman, and K L Klomparens. *Elektronenmikroskopie: Grundlagen, Methoden, Anwendungen*. Spektrum, Akad. Verlag, 1995.

[66] K Schlueter, M Balden, and T da Silva. Evaluating crystal-orientation-dependent properties on polycrystalline tungsten: Example oxidation. *International Journal of Refractory Metals and Hard Materials*, page 105189, 2020.

[67] K Schlueter and M Balden. Dependence of oxidation on the surface orientation of tungsten grains. *International Journal of Refractory Metals and Hard Materials*, 79:102–107, 2019.

[68] S van der Walt, J L Schönberger, J Nunez-Iglesias, F Boulogne, J D Warner, N Yager, E Gouillart, T Yu, and the scikit-image contributors. Scikit-image: image processing in Python. *PeerJ*, 2:e453, 6 2014. doi: 10.7717/peerj.453. URL `https://doi.org/10.7717/peerj.453`.

[69] C C Mardare and A W Hassel. Review on the versatility of tungsten oxide coatings. *Physica Status Solidi (a)*, page 1900047, 2019.

[70] A Kobayashi, S Sharafat, and N M Ghoniem. Formation of tungsten coatings by gas tunnel type plasma spraying. *Surface and Coatings Technology*, 200 (14-15):4630–4635, 2006.

[71] G R Smolik, S J Piet, and R M Neilson Jr. Predictions of radioactive tungsten release for hypothetical ITER accidents. *Fusion Technology*, 19(3P2B):1398–1402, 1991.

[72] O K Varghese, M Paulose, and C A Grimes. Long vertically aligned titania nanotubes on transparent conducting oxide for highly efficient solar cells. *Nature Nanotechnology*, 4(9):592, 2009.

[73] K Hara, Z-G Zhao, Y Cui, M Miyauchi, M Miyashita, and S Mori. Nanocrystalline electrodes based on nanoporous-walled WO_3 nanotubes for organic-dye-sensitized solar cells. *Langmuir*, 27(20):12730–12736, 2011.

[74] J Yu and L Qi. Template-free fabrication of hierarchically flower-like tungsten trioxide assemblies with enhanced visible-light-driven photocatalytic activity. *Journal of Hazardous Materials*, 169(1-3):221–227, 2009.

[75] C W Lai and S Sreekantan. Incorporation of WO_3 species into TiO_2 nanotubes via wet impregnation and their water-splitting performance. *Electrochimica Acta*, 87:294–302, 2013.

[76] X Wang, N Miura, and N Yamazoe. Study of WO_3-based sensing materials for NH_3 and NO detection. *Sensors and Actuators B: Chemical*, 66(1-3):74–76, 2000.

[77] S Berger, H Tsuchiya, A Ghicov, and P Schmuki. High photocurrent conversion efficiency in self-organized porous WO_3. *Applied Physics Letters*, 88(20): 203119, 2006.

[78] D Maisonnier, I Cook, S Pierre, B Lorenzo, B Edgar, B Karin, F Robin, G Luciano, H Stephan, N Claudio, et al. The European power plant conceptual study. *Fusion Engineering and Design*, 75:1173–1179, 2005.

[79] F Koch and H Bolt. Self passivating W-based alloys as plasma facing material for nuclear fusion. *Physica Scripta*, 2007(T128):100, 2007.

[80] A Calvo, C García-Rosales, N Ordás, I Iturriza, K Schlueter, F Koch, G Pintsuk, E Tejado, and J Y Pastor. Self-passivating W-Cr-Y alloys: characterization and testing. *Fusion Engineering and Design*, 124:1118–1121, 2017.

[81] A Calvo, K Schlueter, E Tejado, G Pintsuk, N Ordás, I Iturriza, R Neu, J Y Pastor, and C García-Rosales. Self-passivating tungsten alloys of the system W-Cr-Y for high temperature applications. *International Journal of Refractory Metals and Hard Materials*, 73:29–37, 2018.

[82] E Sal, C García-Rosales, K Schlueter, K Hunger, M Gago, M Wirtz, A Calvo, I Andueza, R Neu, and G Pintsuk. Microstructure, oxidation behaviour and thermal shock resistance of self-passivating W-Cr-Y-Zr alloys. *Nuclear Materials and Energy*, 24:100770, 2020.

[83] W E Boggs, R H Kachik, and G E Pellissier. The effects of crystallographic orientation and oxygen pressure on the oxidation of iron. *Journal of The Electrochemical Society*, 114(1):32–39, 1967.

[84] J Gao, A Hu, M Li, and D Mao. Influence of crystal orientation on copper oxidation failure. *Applied Surface Science*, 255(11):5943–5947, 2009.

[85] J R Ligenza. Effect of crystal orientation on oxidation rates of silicon in high pressure steam. *The Journal of Physical Chemistry*, 65(11):2011–2014, 1961.

[86] A Manhard, G Matern, and M Balden. A step-by-step analysis of the polishing process for tungsten specimens. *Practical Metallography*, 50(1):5–16, 2013.

[87] M Will. Korrelation der Wolframoxidation mit der Kristallorientierung. 2019. URL http://hdl.handle.net/21.11116/0000-0005-6D6F-6.

[88] F Koch, J Brinkmann, S Lindig, T P Mishra, and Ch Linsmeier. Oxidation behaviour of silicon-free tungsten alloys for use as the first wall material. *Physica Scripta*, 2011(T145):014019, 2011.

[89] F Klein, T Wegener, A Litnovsky, M Rasinski, X Tan, J Schmitz, Ch Linsmeier, J Coenen, H Du, J Mayer, et al. On oxidation resistance mechanisms at 1273 K of tungsten-based alloys containing chromium and yttria. *Metals*, 8(7):488, 2018.

[90] C Xu and W Gao. Pilling-bedworth ratio for oxidation of alloys. *Material Research Innovations*, 3(4):231–235, 2000.

[91] Specifications of atomic force microscopy (Bruker). 12.12.2019. URL https://www.bruker.com/fileadmin/user_upload/8-PDF-Docs/SurfaceAnalysis/AFM/Brochures/Dimension_FastScan_Atomic_Force_Microscope_brochure.pdf.

[92] Specifications of atomic force microscopy (Park Systems), 12.12.2019. URL https://www.parksystems.com/products/large-sample-afm/park-xe15/specifications.

[93] Y Yamada-Takamura, F Koch, H Maier, and H Bolt. Hydrogen permeation barrier performance characterization of vapor deposited amorphous aluminum oxide films using coloration of tungsten oxide. *Surface and Coatings Technology*, 153(2-3):114–118, 2002.

[94] E Hasselbrink and S Tauchmann. Crystal lattice figures. 11.12.2019. URL http://www.phchem.uni-duisburg-essen.de/photochem/Crystal%20faces.pdf.

[95] G Fulton and A Lunev. Probing the correlation between phase evolution and growth kinetics in the oxide layers of tungsten using Raman spectroscopy and EBSD. *Corrosion Science*, 162:108221, 2020.

[96] F Klein, T Wegener, A Litnovsky, M Rasinski, X Y Tan, J Gonzalez-Julian, J Schmitz, M Bram, J W Coenen, and Ch Linsmeier. Oxidation resistance of bulk plasma-facing tungsten alloys. *Nuclear Materials and Energy*, 15:226–231, 2018.

[97] C Lehmann and P Sigmund. On the mechanism of sputtering. *Physica Status Solidi (b)*, 16(2):507–511, 1966.

[98] M Hölscher, D Raabe, and K Lücke. Rolling and recrystallization textures of bcc steels. *Steel Research*, 62(12):567–575, 1991.

[99] R Arredondo, M Oberkofler, T Schwarz-Selinger, U von Toussaint, VV Burwitz, A Mutzke, E Vassallo, and M Pedroni. Angle-dependent sputter yield measurements of keV D ions on W and Fe and comparison with SDTrimSP and SDTrimSP-3D. *Nuclear Materials and Energy*, 18:72–76, 2019.

[100] A Mutzke, R Schneider, W Eckstein, and R Dohmen. SDTrimSP: Version 5.00. IPP, Report,(12/8). *Max Planck-Institut für Plasmaphysik*, 2011.

[101] R Arredondo Parra. SIESTA: A new ion source setup and its application to erosion studies on first-wall materials for fusion reactors. 2019. URL http://hdl.handle.net/21.11116/0000-0003-8BDC-9.

[102] P Blank and K J Wittmaack. Energy and fluence dependence of the sputtering yield of silicon bombarded with argon and xenon. *Journal of Applied Physics*, 50(3):1519–1528, 1979.

[103] A A Haasz and J W Davis. Flux and energy dependence of radiation-enhanced sublimation of graphite. *Journal of Nuclear Materials*, 151(1):77–80, 1987.

[104] R Arredondo, M Oberkofler, K Schmid, T Schwarz-Selinger, W Jacob, and R Neu. SIESTA: A high current ion source for erosion and retention studies. *Review of Scientific Instruments*, 89(10):103501, 2018.

[105] R Arredondo, M Balden, A Mutzke, U von Toussaint, S Elgeti, T Höschen, K Schlueter, M Mayer, M Oberkofler, and W Jacob. Impact of surface enrichment and morphology on sputtering of EUROFER by deuterium. *Nuclear Materials and Energy*, 23:100749, 2020.

[106] G Hobler. Monte Carlo simulation of two-dimensional implanted dopant distributions at mask edges. *Nuclear Instruments and Methods in Physics Research Section B: Beam Interactions with Materials and Atoms*, 96(1-2):155–162, 1995.

[107] C Ebm and G Hobler. *Nuclear Instruments Methods*, B 267:2987–2990, 2009. doi: 10.1016/j.nimb.2009.06.014.

[108] Gerhard Hobler, Dawid Maciążek, and Zbigniew Postawa. *Physical Review B*, 97(15):155307, April 2018. doi: 10.1103/PhysRevB.97.155307.

[109] K Nordlund, F Djurabekova, and G Hobler. Large fraction of crystal directions leads to ion channeling. *Physical Review B*, 94(21):214109, 2016.

[110] K Nordlund. Molecular dynamics simulation of ion ranges in the 1–100 keV energy range. *Computational Materials Science*, 3(4):448–456, 1995.

[111] T A Runkler. Data analytics. *Wiesbaden: Springer*, 10:978–3, 2012.

[112] Y Stark, R Frömter, D l Stickler, and H P Oepen. Sputter yields of single-and polycrystalline metals for application in focused ion beam technology. *Journal of Applied Physics*, 105(1):013542, 2009.

[113] R E Franklin, E C G Kirk, J R A Cleaver, and H Ahmed. Channelling ion image contrast and sputtering in gold specimens observed in a high-resolution scanning ion microscope. *Journal of Materials Science Letters*, 7(1):39–41, 1988.

[114] T E Everhart and R F M Thornley. Wide-band detector for micro-microampere low-energy electron currents. *Journal of Scientific Instruments*, 37(7):246–248, jul 1960. doi: 10.1088/0950-7671/37/7/307. URL `https://doi.org/10.1088%2F0950-7671%2F37%2F7%2F307`.

[115] L A Giannuzzi and J R Michael. Comparison of channeling contrast between ion and electron images. *Microscopy and Microanalysis*, 19(2):344–349, 2013.

[116] 2020. URL `https://www.hcstarck.com/en/home.html`.

[117] R Neu, H Maier, M Balden, S Elgeti, H Gietl, H Greuner, A Herrmann, A Houben, V Rohde, B Sieglin, et al. Investigations on tungsten heavy alloys for use as plasma facing material. *Fusion Engineering and Design*, 124:450–454, 2017.

[118] R Neu, H Maier, M Balden, R Dux, S Elgeti, H Gietl, H Greuner, A Herrmann, T Höschen, M Li, et al. Results on the use of tungsten heavy alloys in the divertor of ASDEX Upgrade. *Journal of Nuclear Materials*, 511:567–573, 2018.

[119] T J Hubbard and Erik K Antonsson. Emergent faces in crystal etching. *Journal of Microelectromechanical Systems*, 3(1):19–28, 1994.

[120] J S Danel and G Delapierre. Anisotropic crystal etching: A simulation program. *Sensors and Actuators A: Physical*, 31(1-3):267–274, 1992.

[121] K Sato, M Shikida, Y Matsushima, T Yamashiro, K Asaumi, Y Iriye, and M Yamamoto. Characterization of orientation-dependent etching properties of single-crystal silicon: effects of KOH concentration. *Sensors and Actuators A: Physical*, 64(1):87–93, 1998.

[122] Y L Kanamori, K Hane, H Sai, and H Yugami. 100 nm period silicon antireflection structures fabricated using a porous alumina membrane mask. *Applied Physics Letters*, 78(2):142–143, 2001.

[123] H Tanaka, D Cheng, M Shikida, and K Sato. Characterization of anisotropic wet etching properties of single crystal silicon: Effects of ppb-level of Cu and Pb in KOH solution. *Sensors and Actuators A: Physical*, 128(1):125–131, 2006.

[124] G Petzow. *Metallographisches, keramographisches und plastographisches Ätzen*. Schweizerbart Science Publishers, Stuttgart, Germany, 08 2006. ISBN 9783443230166. URL http://www.schweizerbart.de//publications/detail/isbn/9783443230166/Petzow_Metall_Keram_u_Plastogr_Atz.

[125] K Gall and H Sehitoglu. The role of texture in tension–compression asymmetry in polycrystalline NiTi. *International Journal of Plasticity*, 15(1):69–92, 1999.

[126] S C Mao, X D Han, Y B Tian, J F Luo, Z Zhang, Y Ji, and M H Wu. In situ EBSD investigations of the asymmetric stress-induced martensitic transformation in TiNi shape memory alloys under bending. *Materials Science and Engineering: A*, 498(1-2):278–282, 2008.

[127] O Matsumoto, S Miyazaki, K Otsuka, and H Tamura. Crystallography of martensitic transformation in TiNi single crystals. *Acta Metallurgica*, 35(8):2137–2144, 1987.

[128] X Fan, G Hu, B Zhang, X Ou, J Zhang, W Zhao, H Jia, L Zou, P Li, and Y Yang. Crack-free single-crystalline Ni-rich layered NCM cathode enable superior cycling performance of lithium-ion batteries. *Nano Energy*, 70:104450, 2020.

[129] C H Christensen, K Johannsen, E Toernqvist, I Schmidt, H Topsøe, and C H Christensen. Mesoporous zeolite single crystal catalysts: Diffusion and catalysis in hierarchical zeolites. *Catalysis Today*, 128(3-4):117–122, 2007.

[130] J D Hunter. Matplotlib: A 2D graphics environment. *Computing in Science & Engineering*, 9(3):90–95, 2007.

[131] 06.04.2020. URL `https://www.gimp.org/`.

[132] 06.04.2020. URL `https://gdal.org/`.

[133] T E Oliphant. *A guide to NumPy*, volume 1. Trelgol Publishing USA, 2006.

A Appendices

A.1 Python tool: Function descriptions

As shown in figure 4.1, the Python tool contains two different parts: functions for data merging and data evaluation. At the moment merging and evaluation functions are called "merge_data_1_28.py" and "evaluation_Data1_23.py", respectively.

Six main functions are necessary for the merging procedure. These functions from the file "merge_data_1_18.py" are listed below:

- load_EBSD_data('path/name.ctf', phase='XY', step_size='XY')

- load_confocal_data('path/name.ctf', rot='XY', flip=0) **or**
  load_tiff_data('path/name.xyz')

- calibrate_confocal_data() **or** calibrate_tiff_data()

- calibrate_EBSD_data()

- calculate_superposition()

- save_confocal_data('path/name') **or** save_tiff_data('path/name')

The function load_EBSD_data() loads the EBSD data. At first the path and file name must be filled in. The format of the EBSD file is CTF (channel text file). It is an export file format from Oxford Instruments. Figure A.1 gives an example for the information provided in the header of this file.


```
1  Channel Text File
2  Prj Y:\HELIOS-2017\2017_12_Dez\2017-12-14-h_schluetk_D008_Sputtering\EBSD\D008_Sputter1_006.cpr
3  Author  [Unknown]
4  JobMode Grid
5  XCells   800
6  YCells   710
7  XStep    0.85
8  YStep    0.85
9  AcqE1    0
10 AcqE2    0
11 AcqE3    0
12 Euler angles refer to Sample Coordinate system (CS0)!   Mag 150 Coverage    100 Device  0   KV  20  TiltAngle   57  TiltAxis    0
13 Phases  3
14 3.1648;3.1648;3.1648    90;90;90     W    11  229 1079592441 5.0.6.2  -1317562963 Curr. Sci. [CUSCAM], (1962), vol. 31, pages 497-499
15 5.431;5.431;5.431   90;90;90    Silicon 11  227 3803863129 5.0.6.3  -1022683988 J. Appl. Phys. [JAPIAU], vol. 56, pages 314-320
16 5.2773;5.1575;7.6673   90;91.73;90 W O3    2   7   1079592441 5.0.6.2  970719984    J. Phys.: Condens. Matter [JCOMEL], (1997), vol. 9, pages 6563-6577
17 Phase  X   Y   Bands    Error  Euler1 Euler2  Euler3  MAD BC  BS
18 0   0.0000  0.0000  0    3   0.0000  0.0000  0.0000  0.0000  27  123
19 0   0.8500  0.0000  0    3   0.0000  0.0000  0.0000  0.0000  29  130
20 0   1.7000  0.0000  0    3   0.0000  0.0000  0.0000  0.0000  34  118
21 0   2.5500  0.0000  0    3   0.0000  0.0000  0.0000  0.0000  32  109
22 1   3.4000  0.0000  5    0   148.57  3.7416  67.251  0.8020  15  127
23 0   4.2500  0.0000  0    3   0.0000  0.0000  0.0000  0.0000  24  128
24 0   5.1000  0.0000  0    3   0.0000  0.0000  0.0000  0.0000  21  126
25 0   5.9500  0.0000  0    3   0.0000  0.0000  0.0000  0.0000  22  117
```

Figure A.1: CTF-file export file of the EBSD system. Two things are important for the load_EBSD_data() function. The "XStep or "YStep" (line 7 or 8) which is called step_size and the 'Phases'. This export file has three phases (line 13) and tungsten (line 14), which is the phase of interest and has the number 1. In this example the function was used as "load_EBSD_data('EBSD/D008_Sputter1_006.ctf', phase='1', step_size='0.85')".

This file combines different phases (e.g. Si or W) and the phases are labeled in numbers. The number zero corresponds to no solution of the crystal orientation. The Python tool will merge only the data points of one phase, e.g. W.

> **Attention**: The merging of a two phase material should work, e.g. first merge phase 1 and then phase 2. This merging procedure has not been tested yet for two phases.

In the function "load_EBSD_data()", the option 'step_size' is important to build up a matrix of data. In the first approach of the python tool, the X,Y coordinates were plotted with "matplotlib.pyplot.plot()"[130], but this was impractical for a large data set. It is better to build up a matrix and visualize the EBSD data with "matplotlib.pyplot.imshow()". The 'step_size' is essential for calculating the matrix dimension. If the 'step_size' is wrong, the loading process will produce a dimensional error "ValueError: cannot reshape array of size 2326010 into shape (4754,5431)".

The function load_confocal_data() loads the CLSM data. At first the path and file name must be filled in. The format of the CLSM file is CSV (comma-separated values). It is an export file format from CLSM (Olympus, LEXT OSL4000). The option 'rot' rotates the data. For example, the rotation is 90° for 'rot='1' and 0° for 'rot=0'. The maximum value is 'rot=3'. For the option 'flip=1', the data is mirrored on the vertical axis. These two options are necessary, because the data could have been exported to CSV with different options.

An alternative function to "load_confocal_data()" is the "function load_tiff_data()". In general, this function loads contrast data of an image and combines them with crystal orientations. For this purpose the image should be pre-processed with a raster graphic editor such as gimp[131] to check, e.g. the histogram of black/white levels. At the moment, there is no perfect work flow and the users should have a few experiences in the topic image processing. (The contrast data in the image should not touch the values 255 or 0, except there are letters or other markers inside, which are not the target data).

The second stage of image data processing (tiff or jpeg) is the use of "GDAL", (Geospatial Data Abstraction Library)[132]. This program converts raster data among different formats. It has the advantage of transferring different data sets into a general data format. At the moment tiff and jpeg format images are converted under linux system. The command line for linux is "gdal_translate -of XYZ 'input_data' 'output_data.xyz'". After generating the data file "output_data.xyz", the path and file name must be filled in the function "load_tiff_data('output-_data.xyz')".

The function "calibrate_confocal_data()" **or** "calibrate_tiff_data()" opens a window for visualizing the data points and allows the user to select distinct structures

with the mouse. The left click of the mouse adds a point, the right click removes the previously added point. If enough points are added, the enter button on the keyboard will end the selection.

The function "calibrate_EBSD_data()" opens a window for visualizing the data points. It works as previously described. With the function "calibrate_tiff_data()" the same distinctive structures should be selected in the image. The function "calculate_superposition()" starts the calculation of EBSD data to a new coordinate system. The function "save_confocal_data()" **or** "save_tiff_data()" saves the merged data to a given directory.

The evaluation process is the second part of the python tool. The main functions of data processing are in the file called "evaluation_Data1_23.py". During the evaluation process, the user can relate the evaluation to a specific research question, e.g. transfer the height data to sputter yields. The main functions in "evaluation_Data1_22.py" are listed below with all possible parameters for the evaluation process:

- data1 = grainBounderies(data1)

- data1 = rotationEBSD(data1,XX,XX,0) –> **optional** (necessary for angle-dependent sputtering)

- data1 = relativeHeighttoAbsHeight(data1, erosion_height) **or**
  data1 = relativeHeighttoAbsOxidTungstenHeight(data1, ABSHeightSEM)

- X, Y, Z, Zstd, Zcounts, h, k1, l = medianDataXYZ(data1, resolution=2, neighbors=1, DataLess=5)

- plot_IPFz(X,Y,Z, resolution=2, [0,1.5], Amount_of_digits=4, 'Title', 'Color_scale_lable')

During the merging process, the merged data are loaded with numpy (data1 = numpy.loadtxt('path/name.dat')) [133]. "data1" is a variable which can be randomly named. As described in section 4.3, the function grainBounderies() is actually a noise filter, which helps to reduce the data set. By performing the function grainBounderies() at first, the other functions run much faster afterwards. The function rotationEBSD(data1,0,XX,0) rotates the EBSD data with equation 2.5. This function is implemented for angle-dependent sputtering. With this function, it is possible to rotate crystal lattices to the ion beam during the evaluation.

The function relativeHeighttoAbsHeight(data1, erosion_height) is a leveling function. This leveling function selects data from the $\langle 100 \rangle$ corner in an IPF (e.g. figure 5.5), and adjusts the height to a given value (e.g. erosion_height = -0.3). Thus, the height of $\langle 100 \rangle$ corner must be known.

> **Attention**: If the ⟨100⟩corner does not have data, the leveling function will run into an error. An option to change the leveling area has not yet been implemented until now.

For a FIB sputter experiment, the erosion height of ⟨100⟩ orientation can be determined by following the procedures given below:

- Obtain a flat surface before the sputter experiment.

- Sputter a rectangle area using FIB, and set the heights outside of the sputtered area as the reference level.

- Run the function "relativeHeighttoAbsHeight(data1,1)" for the first time, which gives the relative height of ⟨100⟩ orientation.

- Set the difference between the reference level and the relative height of ⟨100⟩ orientation as the erosion depth (the value should be negative).

- Run the function "relativeHeighttoAbsHeight(data1, -0.3)" again with the calculated erosion depth. In this example the value is $-0.3\,\mu m$.

> **Attention**: The expression 'data2 = data1' does not copy the data set in python. It creates a pointer to the data set of the type 'list'. As an example, if 'data2' is multiplied with 2, 'data1' is also multiplied with 2. To copy the 'data1' uses 'data2 = data1.copy()'. Therefore, it makes no sense to change the left side of function 'data1 = relativeHeighttoAbsHeight(data1, -0.3)', e.g. to "data2 = relativeHeighttoAbsHeight(data1, -0.3)'.

An extra leveling function was written for oxidation experiments, as the oxidation process erodes tungsten (please see figure 5.2 in section 5.1). The depth growth into the tungsten sample is corrected in the function. For oxidation experiments, the thickness of oxide layers must be known, e.g. through FIB-cuts. Since the ⟨100⟩ corner in an IPFz is leveled, it makes sense to cut cross-sections at these orientations.

After leveling the data, the median of heights and the corresponding positions were taken from the inverse pole figure with the function "medianDataXYZ()". The following three parameters in this Python function need to be set: (i) the data, e.g "data1"; (ii) the resolution, which corresponds to the amount of pixel in the IPF. For a resolution of 1 and 2 the IPF has up to 7200 and 28600 plotted points, respectively; (iii) the 'cut-off' filter. The meaning of 'DataLess=5' is data with less than 5 values for each pixel should be excluded in the IPF. For more details, please see section 4.3.

The last function is the "plot_IPFz()", which requires the XYZ coordinates calculated by using the function "medianDataXYZ()". The Z coordinate can be replaced by Zstd (i.e. the standard deviation), or by Z counts (the amount of measurements for each pixel). Besides, Z can be recalculated to values like sputter yields. The parameter 'resolution' in the "medianDataXYZ() function should be the same. The next parameter in the function sets the title of the IPF figure and the last parameter labels the color of the scale bar, e.g. 'Heights / µm'.

A.2 Sputtering

A.2.1 Setting of SDTrimSP

Below is the input file for the SDTrimSP simulations, which is called 'tri.inp' The parameter 'e0= XXX', is changed for energy dependent sputtering and the parameter 'alpha= XXX', is changed for angle dependent sputtering.

```
Some  title
          &TRI_INP
          text='−−−elemements−−−'
                  ncp=2
                  symbol="Ga",  "W"

          text='−−−beam−−−'
                  case_e0=0
                  e0=30000, 0
                  case_alpha=0
                  alpha0= 0, 0
                  qubeam=1, 0

          text='−−−control−−−'
                  flc=100
                  nh =100000
                  nr_pproj=2
                  idout=−1
                  idrel=0
                  iintegral=1
                  ipivot=8

          text='−−−target−−−'
                  tableinp = "../SDTrimSP6/tables"
                  ttarget=50000
                  nqx=500
                  qu=0, 1
                  iq0=0
                  e_cutoff=2, 2
!         dns0    =−1,−1
!         e_surfb=−1,−1
                  inel0=3, 3
                  qumax=1, 1
                  ipot=1
```

```
                isbv=1

        text='−−−output  parameter '
                lmatrices=.false.
                lparticle_p=.false.
                lparticle_r=.false.
                ltraj_p=.false.
                ltraj_r=.false.
/
```

A.2.2 Fluence
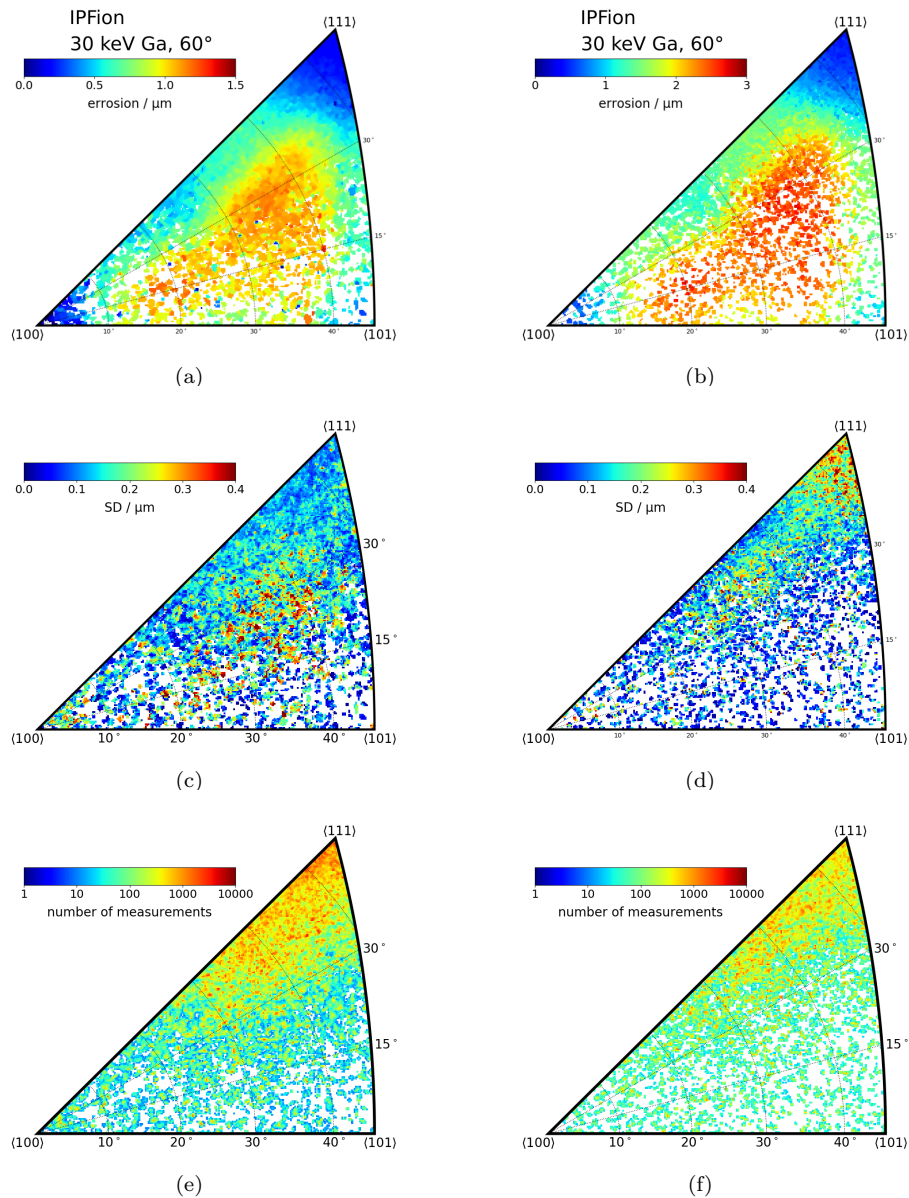
Figure A.2: Influence of ion fluences on the sputter yields of tungsten grains with various crystal orientations. Sputtering of the polycrystalline tungsten sample was conducted with a 30 keV Ga ion beam under an incident angle of 60° with respect to the surface normal: (a) sputter yields versus crystal orientations at a fluence of 5.3×10^{21} at/m^2 and (b) at a fluence of 1.1×10^{22} at/m^2, (c) and (d) show the standard deviations, (e) and (f) the amount of measurments for the sputter yield evaluations in (a) and (b), respectively. The crystal orientations were evaluated to the direction of the ion beam.
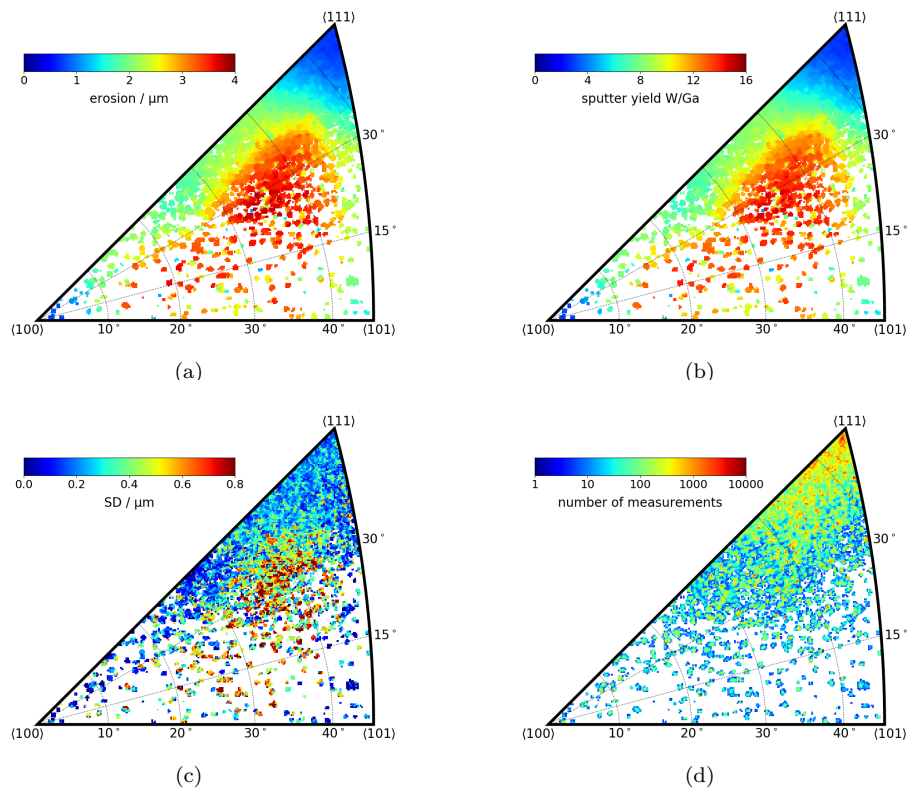
Figure A.3: Influence of ion fluences on the sputter yields of tungsten grains with various crystal orientations. Sputtering of the polycrystalline tungsten sample was conducted with a 30 keV Ga ion beam under an incident angle of 60° with respect to the surface normal: (a) erosion versus crystal orientations at a fluence of $1.62 \times 10^{22} \, \mathrm{at/m^2}$, (b) sputter yields (c) the standard deviations and (d) the amount of measurments. The crystal orientations were evaluated to the direction of the ion beam. Note that the SD is very high which is an indication that the maximum erosion depth of 4 μm was to high.

A.2.3 Tungsten sputtering by 30 keV Ga ions
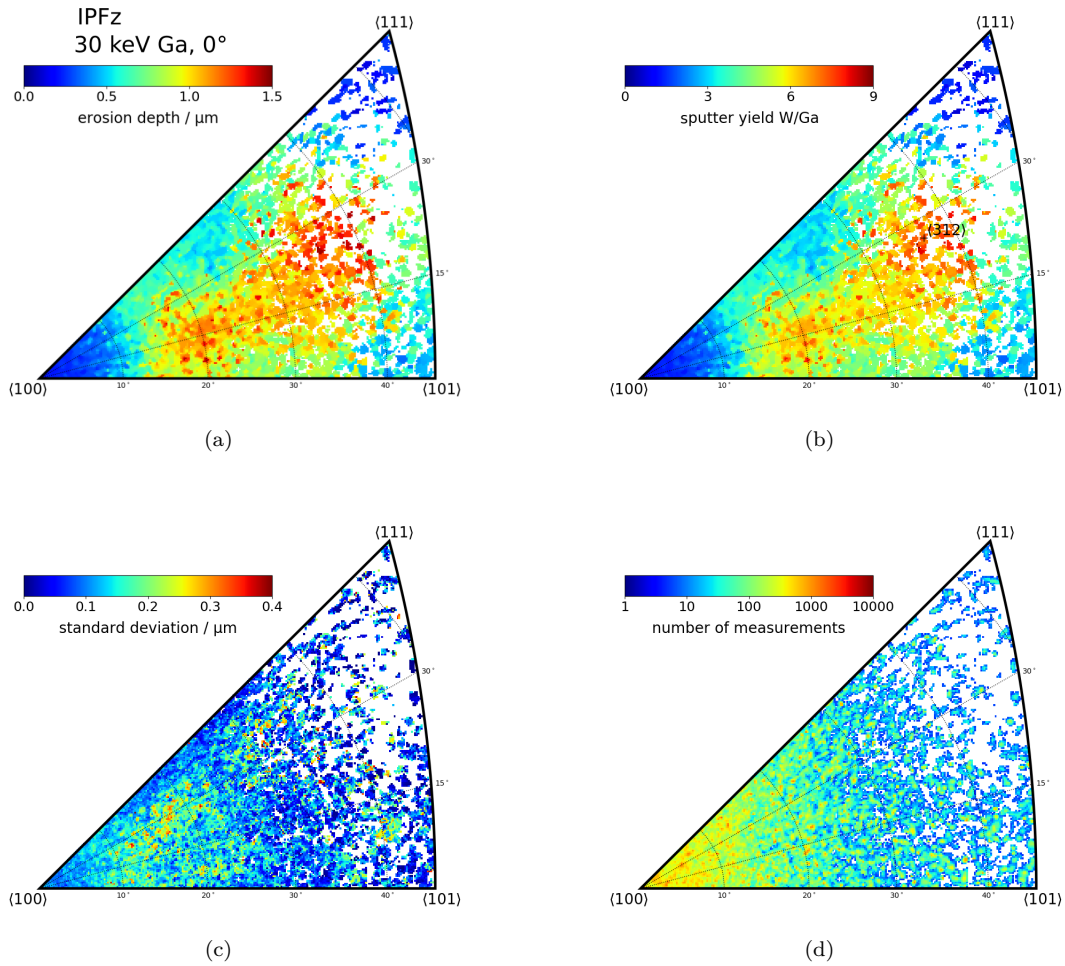
Figure A.4: Statistics for the crystal orientation dependent erosion behavior of tungsten sputtered with a 30 keV Ga ion beam: (a) erosion depths, (b) sputter yields, (c) standard deviations and (d) amount of measurements for the evaluated erosion depths of various crystal orientations shown in 6.3. There were in total 1.8 million measurements in the erosion depth evaluations.

Correction of the impact angle
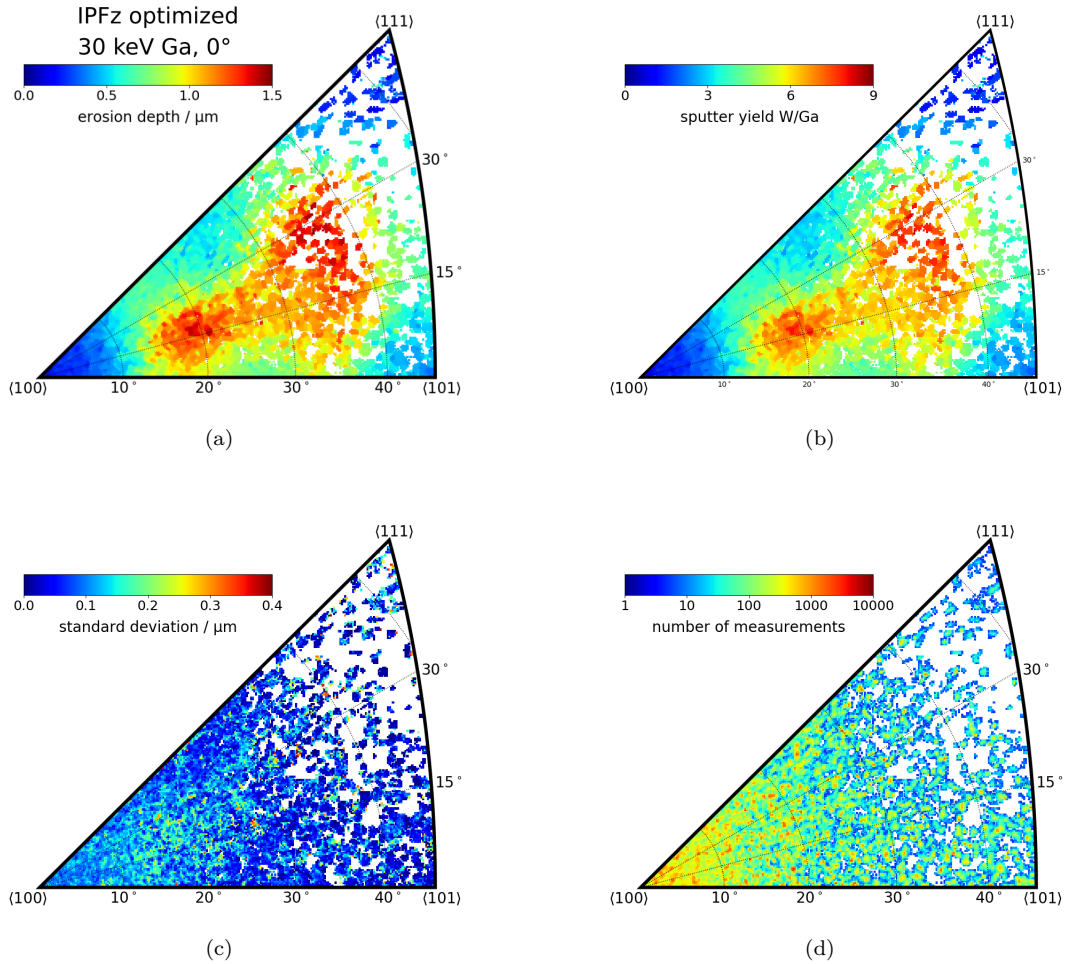
Figure A.5: Statistics for the crystal orientation dependent erosion behavior of tungsten sputtered with a 30 keV Ga ion beam: (a) erosion depths, (b) sputter yields, (c) standard deviations and (d) amount of measurements for the evaluated sputter yields of various crystal orientations shown in 6.30(b). There were in total 1.8 million measurements in the erosion depth evaluations.

A.2.4 Tungsten sputtering by 8 keV Ga ions

(a)

(b)

(c)

(d)
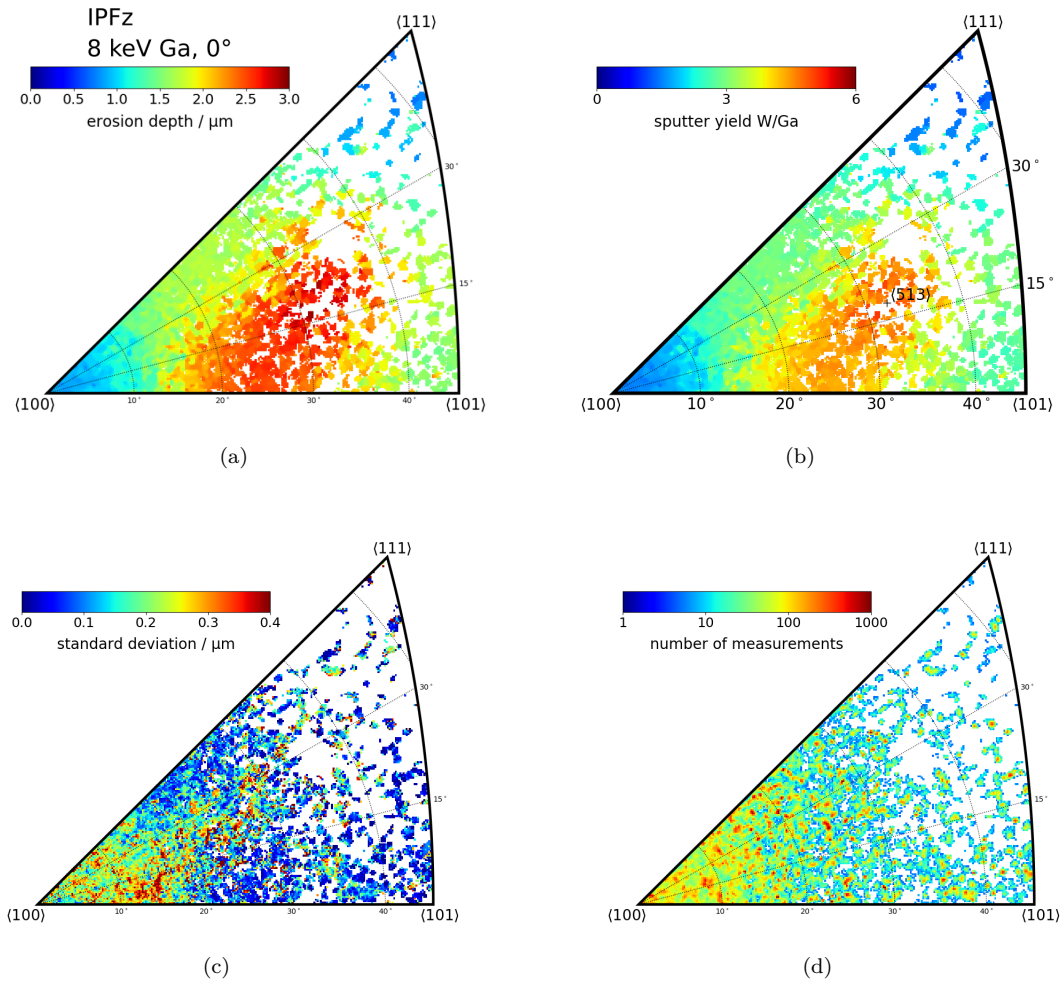
Figure A.6: Statistics for crystal orientation dependent erosion behavior of tungsten sputtered with a 8 keV Ga ion beam: (a) erosion depths, (b) sputter yields, (c) standard deviations and (d) amount of measurements for the evaluated sputter yields of various crystal orientations shown in figure 6.16. There were in total 0.5 million measurements included in the evaluation.

A.2.5 Tungsten sputtering by 5 keV Ga ions
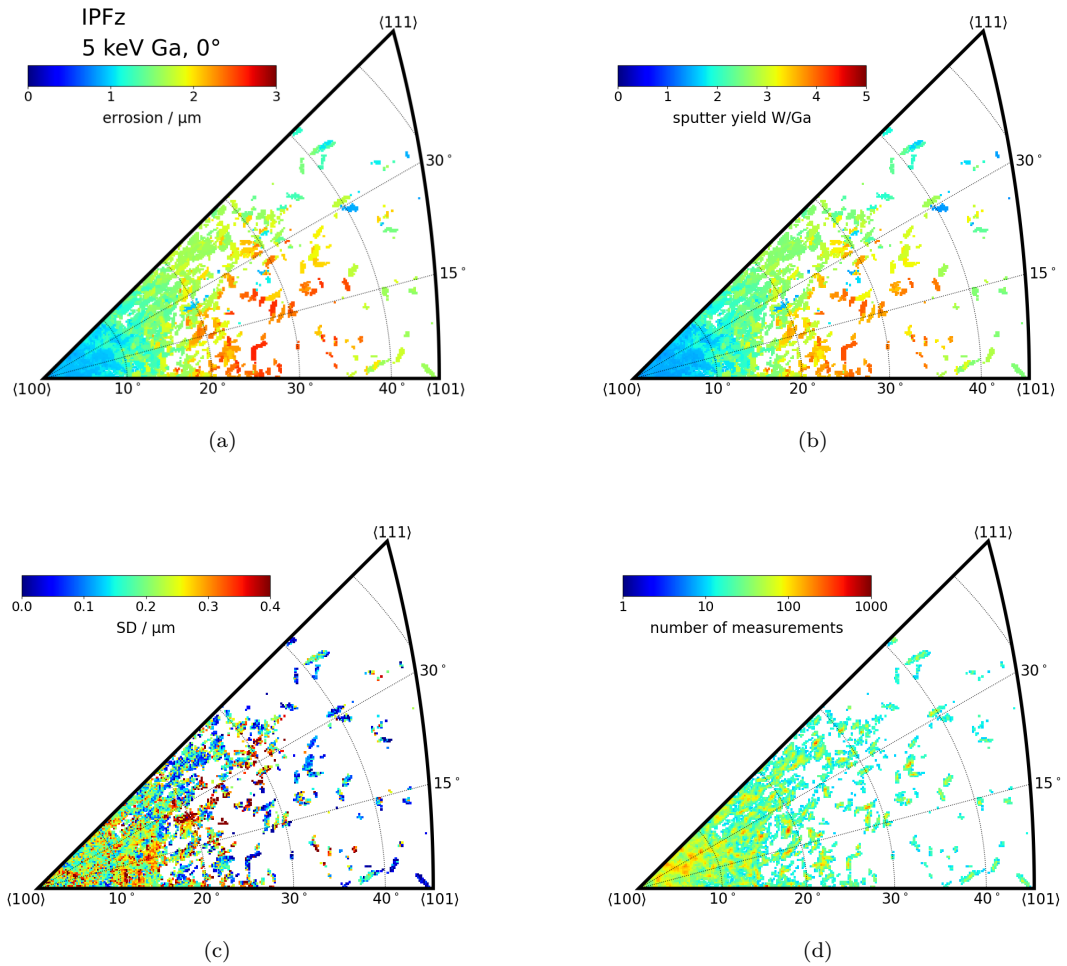
Figure A.7: Statistics for crystal orientation dependent erosion behavior of tungsten sputtered with a 5 keV Ga ion beam: (a) erosion depths, (b) sputter yields, (c) standard deviations and (d) amount of measurements. There were in total 0.2 million measurements included in the evaluation.

A.2.6 Tungsten sputtering by 2 keV Ga ions
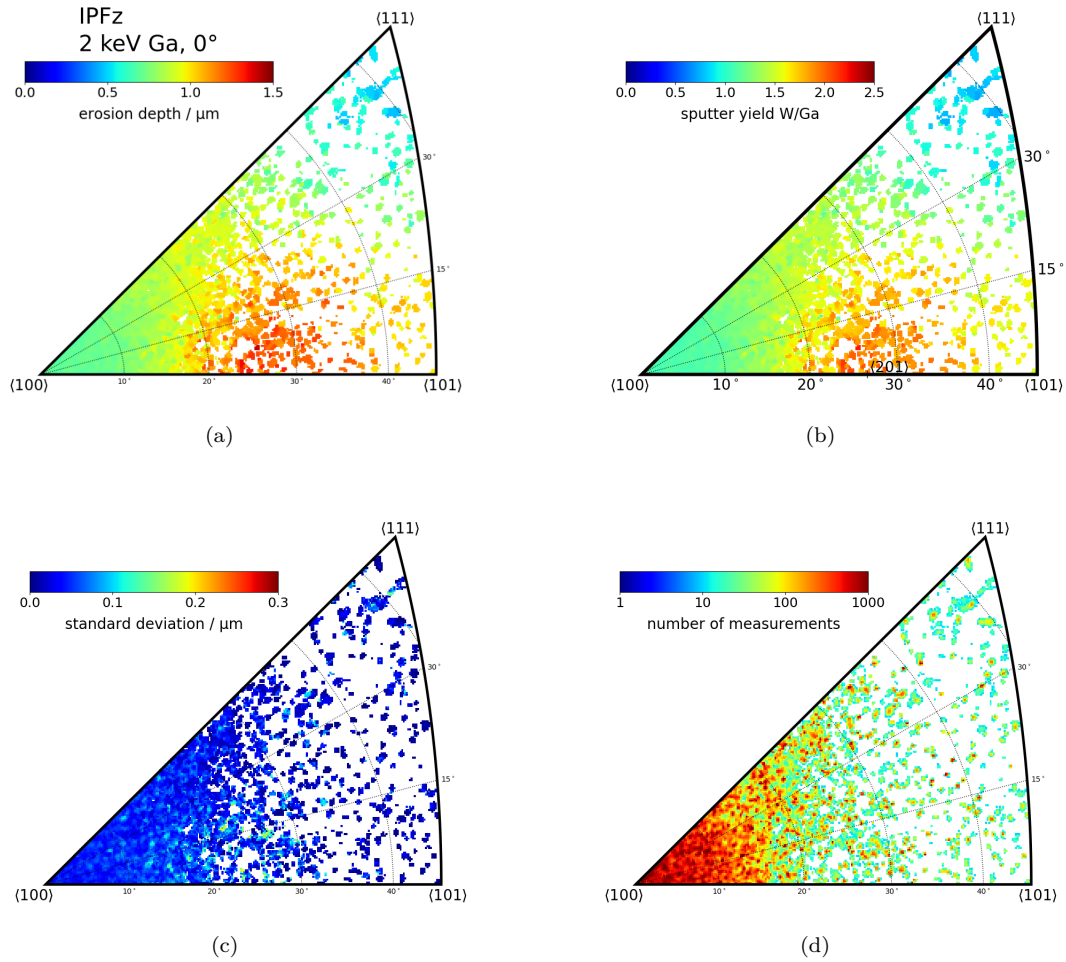
Figure A.8: Statistics for crystal orientation dependent erosion behavior of tungsten sputtered with a 2 keV Ga ion beam: (a) erosion depths, (b) sputter yields, (c) standard deviations and (d) amount of measurements for the evaluated erosion depths of various crystal orientations shown in 6.17. There were in total 1.9 million measurements included in the evaluations.

A.2.7 Optimization of 30 keV sputter data

Remark: A negative ϕ (see figure 2.3 and 6.29) corresponds to a 180° roation in φ for polar coordinates.
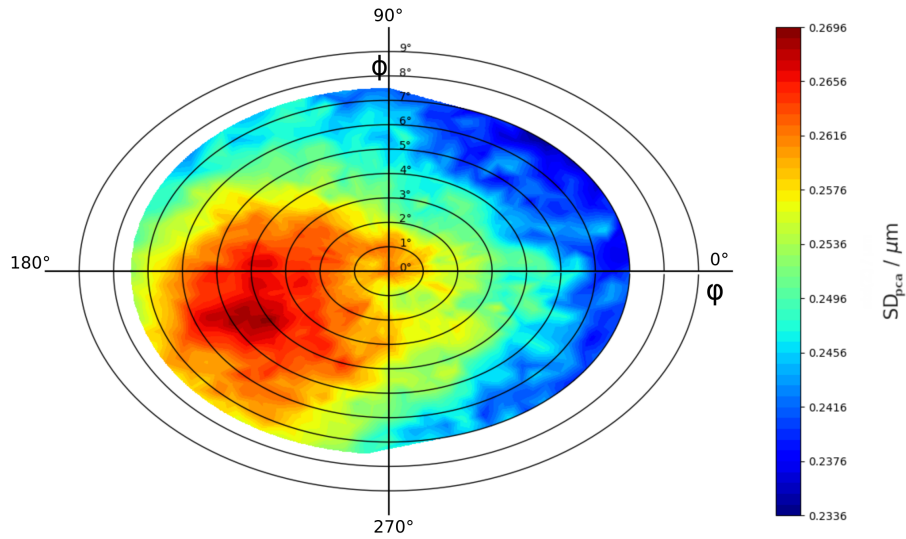
(a) The sample misalignment is in $\varphi_{max} = 30°$ and in $\phi_{max} = -4°$ or in $\varphi_{max} = 210°$ and in $\phi_{max} = 4°$.
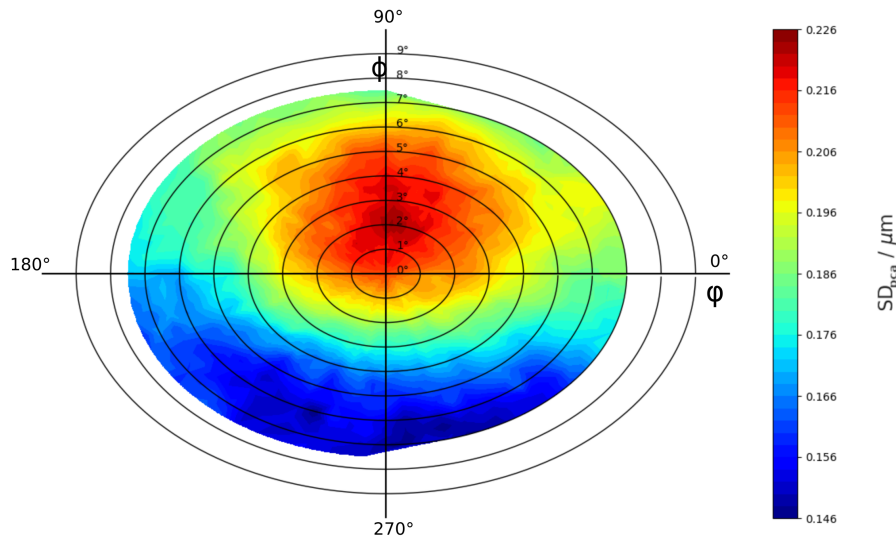
(b) The sample misalignment is in $\varphi_{max} = 80°$ and in $\phi_{max} = 2°$.
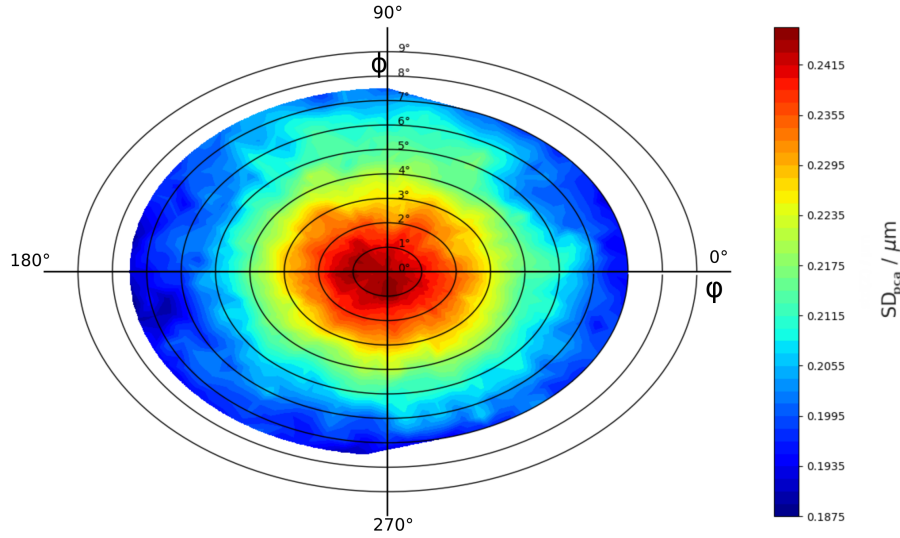
(c) The sample misalignment is in $\varphi_{max} = -90°$ and in $\phi_{max} = 0.5°$ or in $\varphi_{max} = 270°$ and in $\phi_{max} = 0.5°$.
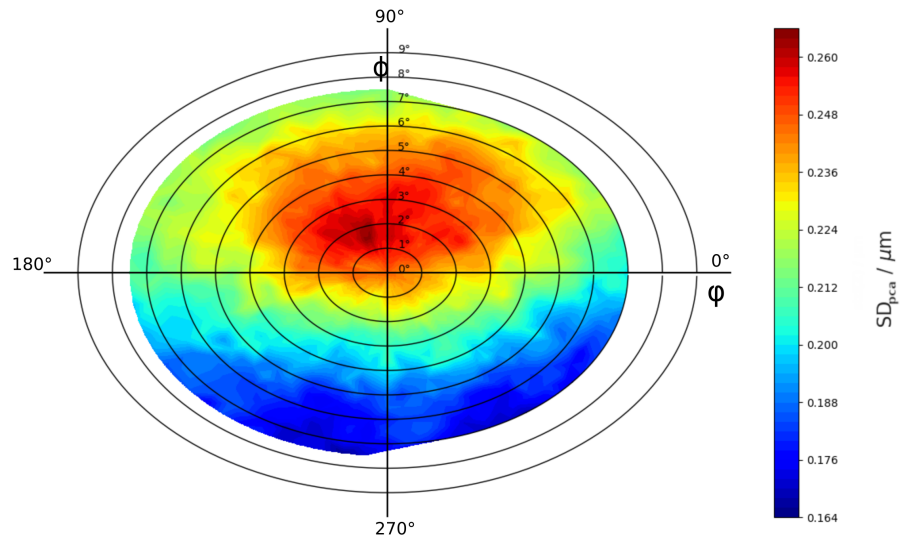
(d) The sample misalignment is in $\varphi_{max} = -70°$ and in $\phi_{max} = -1.5°$ or in $\varphi_{max} = 110°$ and in $\phi_{max} = 1.5°$.

Figure A.9: PCA evaluation showing the misalignment error of the the sample mounting. $\mathrm{SDs_{pca}}$ are shown in regard of two Euler angles in polar coordinates. The crystals were twisted in ϕ, which is the rotation angle in the pole figure, and φ, which is the radius in the pole figure. The maxima of the $\mathrm{SD_{pca}}$ are used to find the angles to rotate the crystal orientation with equation 2.5 for optimizing the sputter yield data (see figure 6.30).

A.2.8 Gallium implantation
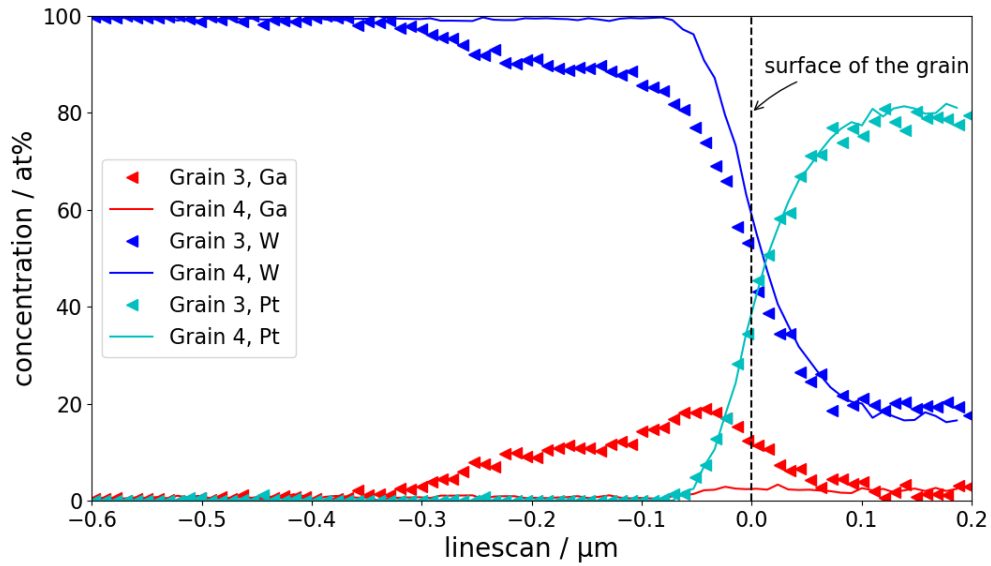
Figure A.10: EDX elemental line scanning of the cross-sections of two tungsten grains with different crystal orientations. The detected Ga atoms were introduced by implantation during sputtering of the polycrystalline tungsten sample with a 30 keV Ga ion beam. The EDX analysis was made directly after the sputter experiment. The surface of both tungsten grains are normalized to x=0, as indicated by the dashed perpendicular line. For SEM images of the cross-sections, please refer to figure 6.39.

A.2.9 Sputtering by 2 keV D ions

Tungsten
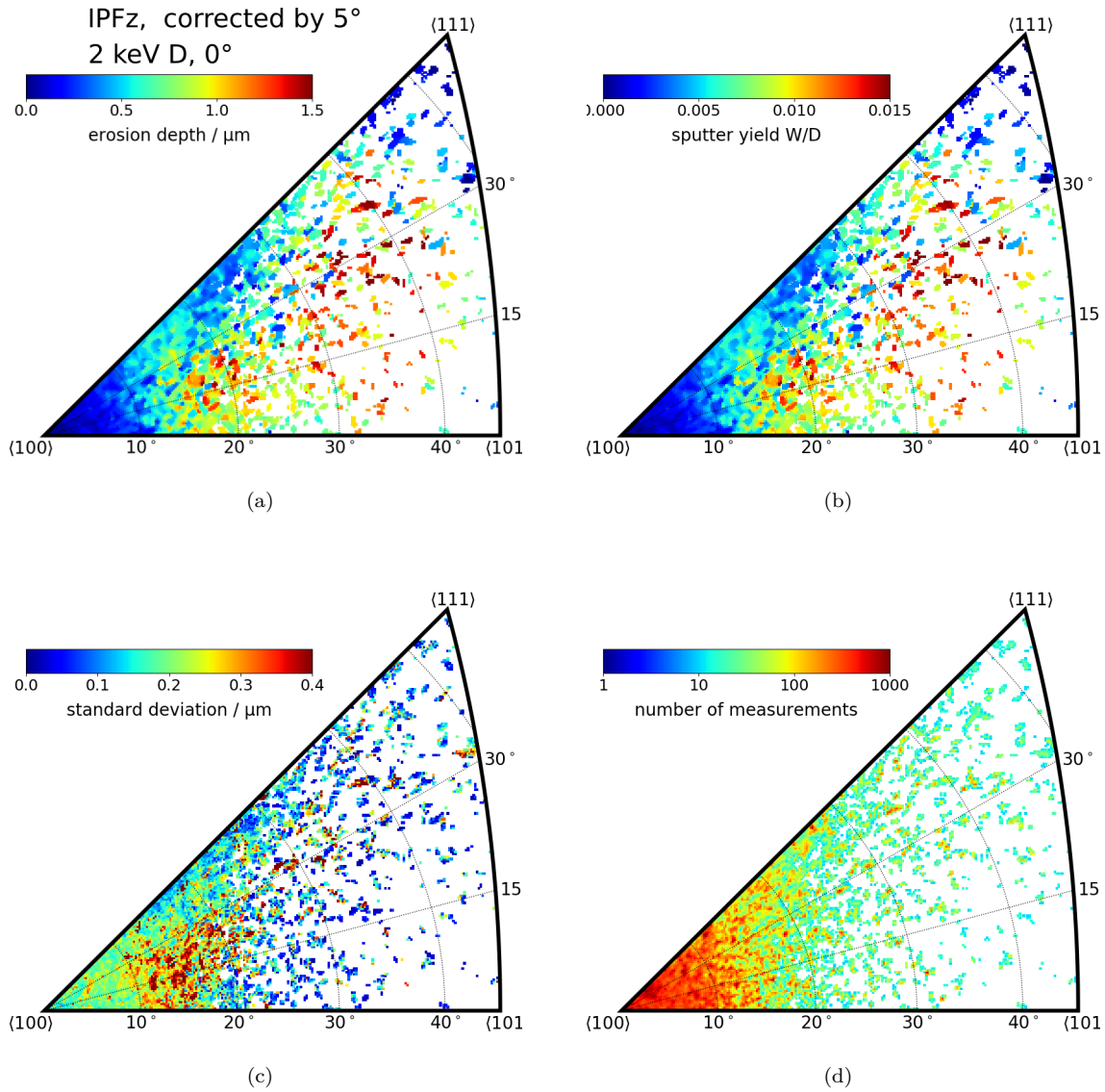
Figure A.11: Statistics for crystal orientation dependent erosion behavior of tungsten sputtered with 2 keV D ion beam: (a) erosion depths, (b) sputter yields, (c) standard deviations and (d) amount of measurements for the evaluated erosion depths of various crystal orientations shown in 6.42. There were in total 1.0 million measurements in the evaluations.
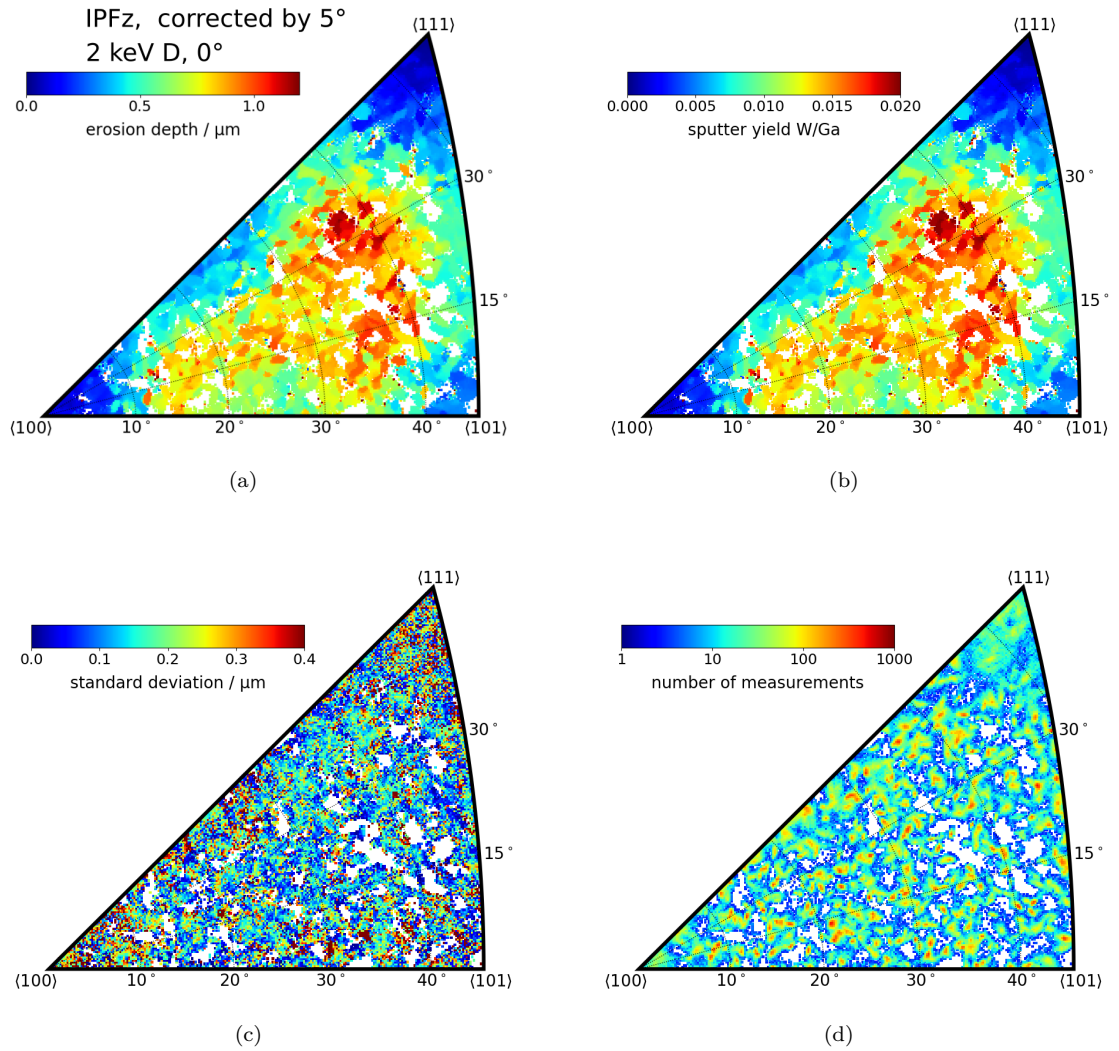
Figure A.12: Statistics for crystal orientation dependent erosion behavior of tungsten sputtered with 2 keV D ion beam: (a) erosion depths, (b) sputter yields, (c) standard deviations and (d) amount of measurements for the evaluated erosion depths of various crystal orientations shown in 6.45.

HPM1850
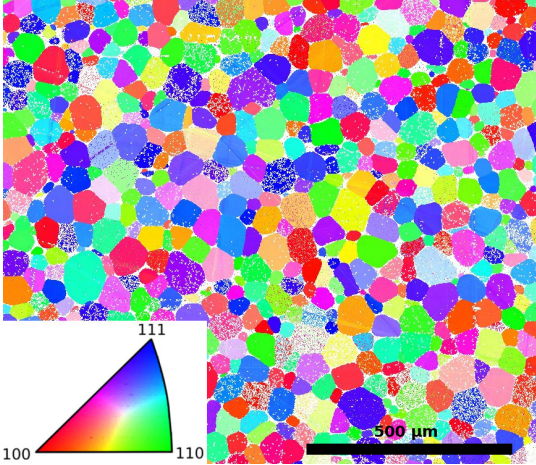
Figure A.13: EBSD map showing crystal orientation distributions on the surface of HPM1850.

EUROFER

The results are described in[105]
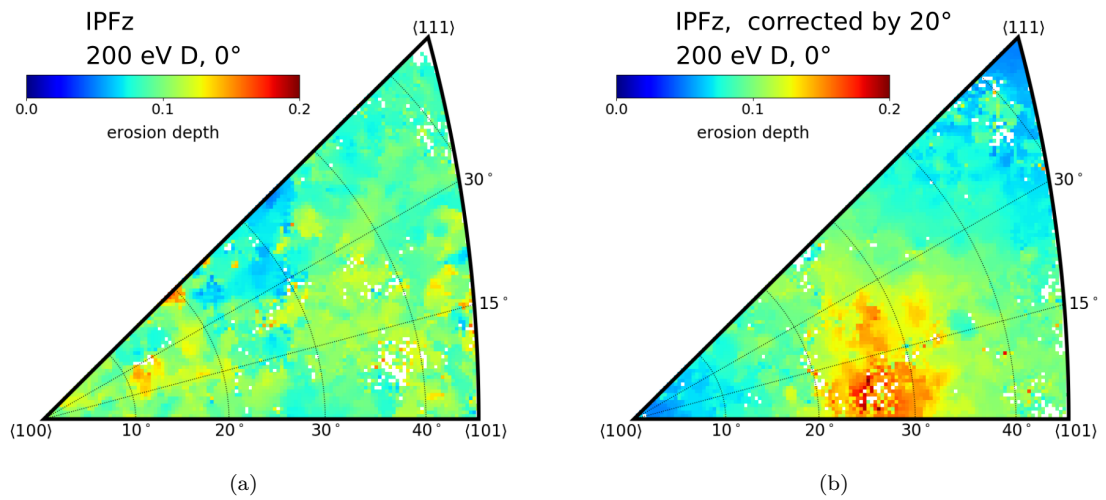
Figure A.14: Eorsion depth of EUROFER bombarded at 300 K by 200 eV D ions (600 eV/D_3^+) to a fluence of 1.4×10^{24} D/m^2. (a) "approximate eroded depth as a function of grain orientation in the direction normal to the sample surface"[105]; (b) reevaluate data due to impact angle detection, which was 20°.

List of Abbreviations

atm	standard atmosphere
AFM	atomic force microscopy
BCA	binary collision approximation
bcc	body-centered cubic
BKD	backscatter Kikuchi diffraction
Cu	copper
FEPA	Federation of European Producers of Abrasives
CEIT	Ceit-IK4 Technology Center
CLSM	confocal laser scanning microscope
CMOS	complementary metal oxide semiconductor
Cr	chromium
D	deuterium
DC	direct current
D-T	deuterium tritium
EBSD	electron backscatter diffraction
EDX	energy dispersive X-ray spectroscopy
Fe	iron
FEI	Field Electron and Ion Co.
FIB	focused ion beam
FIB-SEM	focused ion beam scanning electron microscope
ϵ_{Flade}	flade-potential
Ga	gallium
GIS	gas injection system
H	hydrogen

He	helium
HPM1850	High Performance Materials 1850
HIP	hot isostatic pressing
IPP	Max Planck Institut for Plasma Physics
IPF	inverse pole figure
ISO	International Organization for Standardization
ITER	International Thermonuclear Experimental Reactor
lbs	pound-force
LSM	laser scanning microscope
NaOH	sodium hydroxide
$\mathbf{NaNO_3}$	sodium nitrate
m	mass
MD	molecular dynamic
MV	mean value
min	minutes
O	oxygen
P	partial pressure
Pt	platinum
Pt-C	platinum carbon
PCA	principal component analysis
PPCS	European Power Plant Conceptual Study
PBR	Pilling-Bedworth ratio
PFC	plasma-facing components
RBS	Rutherford Backscattering Spectrometry
RPM	revolutions per minute
s	second

SD	standard deviation
SE	secondary electron
SDTrimSP	static/dynamic transport of ions in matter with the calculation mode serial or parallel
SEM	scanning electron microscope
SIESTA	second ion experiment for sputtering and TDS analysis
STA	simultaneous thermal analysis
t	time
W	tungsten
TEM	transmission electron microscopy
TGA	thermogravimetric analysis
$\mathbf{T}_R$	recrystallization temperature
TT	temperatur treatment
W	tungsten
WD	working distance
$\mathbf{WO}_3$	tungsten(VI)-oxide
Y	yttrium

List of Figures

151

154

155

158

159

162

List of Tables

Acknowledgments

I would like to thank the following people, without whom I would not have been able to complete this research:

Prof. Dr. Rudolf Neu acting as academic supervisor and providing excellent support during the whole thesis. Specifically I would like to thank him for the valuable scientific discussions.

Dr. Martin Balden for the introduction into the analytical systems, the constant support throughout the preparation of the thesis including many intense and fruitful scientific discussions.

Dr. Ulrich Stroth for the possibility to work in E2M division and providing a superior research environment.

I am especially thankful to Stefan Elgeti, Katja Hunger and Gabriele Matern for their support in the sample preparation as well as the support and advice for the SEM and FIB. I am grateful to them for their scientific discussions.

I would additionally like to express my gratitude to Prof. Kai Nordlund from the University of Helsinki and Prof. Gerhard Hobler from TU Wien. They performed crystal orientation dependent simulations and helped to publish these data together with the data of this work.

Furthermore, many thanks to all my other colleagues at the IPP, especially Dr. Hans Maier, Dr. Udo von Toussaint, Dr. Wolfgang Jacob, Dr. Rodrigo Arredondo Parra, Dr. Georg Holzner, Dr. Liang Gao, Dr. Johannes Bauer as well as the other participants of the scientific round table and of the PWI meeting. In addition, I would like to thank Prof. Tiago da Silva to his great support with Python and contributions for the publications.

I am grateful to Prof. Peter Manz. He supported, discussed and organized the International Helmholtz Graduate School for Plasma Physics (HEPP).

Finally, I would like to thank my family, especially my wife Mingyue for her steady support and her patience over the past years.